On the Distribution of Dark Matter in Clusters of Galaxies

Thesis by
David J. Sand

In Partial Fulfillment of the Requirements
for the Degree of
Doctor of Philosophy

California Institute of Technology
Pasadena, California

2005

(Defended September 6, 2005)

Acknowledgements

There are many, many people to thank for this thesis and without them it would not have been possible.

I have been lucky to have a great advisor in Richard Ellis. During my first year when I was looking for a research group, he was the only one eager to talk with me and to offer me a position. Richard was always there to give praise and sage advice at the right times. He always has the big picture in mind, something that is easy to miss when you're buried in data. And he is always out advertising your work to others. He would also light a fire under my ass when necessary.

One of my greatest mentors here at Caltech has been Tommaso Treu. His importance can not be overstated. From my first moments joining Richard Ellis' group until the day before my thesis defense, Tommaso has been there to hear my concerns, to focus my thoughts, and to calm me down. He has taught me nearly everything I know about doing science and astronomy. More than that, he has been a great friend. He and his wife, Stefania Tutino, have always provided wonderful food and conversation. Thank you so much Tommaso and Stefania. I hope we stay close.

A separate mention is due to my office mates Kevin Bundy and Stanimir Metchev, along with my pseudo-office mate Josh Eisner. Thank you for the good times and the friendship these last several years. I am confident that I have made life-long friends. I would like to deeply and dearly thank Vivian Castro for her love during my first year of graduate school and her support ever since. I wish great things for her. Russel White always gave me the call, with an occasional chili burger and many, many drinks behind us. I wish to thank Alice Shapley for always being available to talk, gossip and give advice, even many years after she left Caltech. I would like to thank Mike Santos and Alison Farmer for many nights of hours-long conversation. Farmer John, you weren't a bad roomate either. It was excellent grabbing coffee and having scientific discussions with Graham Smith. Thanks to Jean-Paul Kneib for his hospitality in Marseilles so that Chapter 5 of this thesis could happen. Little Dan and Brian are always up for a chat or some lunch or even a 40 oz. Good luck, don't work too hard. Melissa Enoch has always been a good friend to me, despite the hard time that I give her. Pizza and a movie was always so great or even a quick run to In n' Out. We have had our ups and downs, but hopefully we will continue to be friends.

Thanks go to my thesis committee: Andrew Blain, John Mulchaey and Marc Kamionkowski. John was always supportive and allowed me to come up to Carnegie whenever for a quick chat. Marc was the one who encouraged me to switch to an observational cosmology group and to work with Richard Ellis in particular. Thanks Marc, I owe you one. Keep listening to hip-hop.

This acknowledgement section would not be complete if I did not thank Ernie and Ernesto's lunch truck, who kept my belly happy with good food and were always friendly. The lunch trucks in Tucson will pale in comparison.

My family deserves particular thanks. My parents have been incredibly supportive all these years. Even though I don't call enough or let them visit enough, my love is strong. The free meals were always appreciated as well as the advice you gave on life in general. Thank you for encouraging me to go to grad school, for whatever reasons I had.

Finally, I am deeply grateful to my sunshine, Eva Rose Murdock. Thank you so much for popping into my life out of no where. You have supported and loved me beyond all expectations and I will never forget it. Bring on the adventures.

On the Distribution of Dark Matter in Clusters of Galaxies

by

David J. Sand

In Partial Fulfillment of the
Requirements for the Degree of
Doctor of Philosophy

Abstract

The goal of this thesis is to provide constraints on the dark matter density profile in galaxy clusters by developing and combining different techniques. The work is motivated by the fact that a precise measurement of the logarithmic slope of the dark matter on small scales provides a powerful test of the Cold Dark Matter paradigm for structure formation, where numerical simulations suggest a density profile $\rho_{DM} \propto r^{-1}$ or steeper in the innermost regions.

We have obtained deep spectroscopy of gravitational arcs and the dominant brightest cluster galaxy in six carefully chosen galaxy clusters. Three of the clusters have both radial and tangential gravitational arcs while the other three display only tangential arcs. We analyze the stellar velocity dispersion for the brightest cluster galaxies in conjunction with axially symmetric lens models to jointly constrain the dark and baryonic mass profiles jointly. For the radial arc systems we find the inner dark matter density profile is consistent with $\rho_{DM} \propto r^{-\beta}$, with $\langle\beta\rangle = 0.52^{+0.05}_{-0.05}$ (68% CL). Likewise, an upper limit on β for the tangential arc sample is found to be $\beta < 0.57$ (99% CL). We study a variety of possible systematic uncertainties, including the consequences of our one-dimensional mass model, fixed dark matter scale radius, and simple velocity dispersion analysis, and conclude that at most these systematics each contribute a $\Delta\beta \sim 0.2$ systematic into our final conclusions. These results suggest the relationship between dark and baryonic matter in cluster cores is more complex than anticipated from dark matter only simulations.

Recognizing the power of our technique, we have performed a systematic search of the Hubble Space Telescope Wide Field and Planetary Camera 2 data archive for further examples of systems containing tangential and radial gravitational arcs. We carefully examined 128 galaxy cluster cores and found 104 tangential arcs and 12 candidate radial arcs, each of whose length to width ratio exceeds 7. Twenty-four additional radial arc candidates were identified with smaller length to width ratios. In order to confirm the nature of these radial arc candidates, we obtained Keck spectroscopy of 17 candidate radial arcs, suggesting that the contamination rate from non-lensed objects is ~30-50%. With this catalog of gravitational arcs, we use the number ratio of radial to tangential arcs as a statistical measure of the inner logarithmic dark matter slope, β, in galaxy cluster cores. This abundance ratio is fairly constant across various cluster subsamples partitioned according to X-ray luminosity and optical survey depth. Using two-component mass models for cluster cores, we show that the arc statistics in our survey are consistent with $\beta \lesssim 1.6$, depending on various assumptions, the most important of which is the stellar mass associated with the brightest cluster galaxy.

Finally, in order to refine and confirm the analysis technique presented for the six galaxy clusters with gravitational arcs and brightest cluster galaxy dynamics, and to address several comments on our earlier work, we present a more elaborate two dimensional lens model of the cluster MS2137 using a newly upgraded gravitational lensing code. We combine these two-dimensional lens model constraints with the velocity dispersion data of the brightest cluster galaxy to constrain the dark and baryonic mass profiles jointly. We find the inner dark matter density profile to be consistent with a distribution with logarithmic inner slope $\langle\beta\rangle = 0.25^{+0.35}_{-0.12}$ (68% CL) in agreement with the axially symmetric model presented earlier for MS2137 ($\langle\beta\rangle = 0.57^{+0.11}_{-0.08}$) with simpler assumptions. However, we do find a significant degeneracy remains between the scale radius, r_{sc}, and inner logarithmic slope, β, which might be resolved with further lensing data at larger radii. Notwithstanding this limitation, we conclude that our technique of combining gravitational lensing with stellar dynamics offers a reliable probe of the dark matter distribution in clus-

ters and that, most likely, a discrepancy remains between numerical predictions in the CDM paradigm and our observations.

Contents

3 The Dark Matter Distribution in the Central Regions of Galaxy Clusters: Implications for CDM 43

List of Figures

List of Tables

Chapter 1

Introduction

One of the great challenges of astrophysics is to understand how galaxies and galaxy clusters formed and evolved. It is clear that dark matter plays a dominant role in cosmology and the galaxy formation process (Davis et al., 1985; Percival et al., 2001; Spergel et al., 2003; Croft et al., 2002; Bahcall et al., 2003), making the nature of dark matter and its relationship to baryons key to our understanding of structure formation. The goal of this thesis is to provide new constraints on the dark matter (DM) density profile in galaxy clusters by developing and combining different techniques. Why is it important to measure the DM density profile of galaxy clusters? It is the goal of this introduction to address this question.

This chapter is intended to give a brief overview of the current observational and theoretical status of DM from the astronomical perspective. Readers interested in the unknown identity of the dark matter particle and the intensive efforts underway to uncover it are directed to the recent review by Gaitskell (2004). In § 1.1 I will discuss the basic observations and analyses which led to the current view that some form of dark matter is required to make sense of observational results. Dark matter plays a central role in our understanding of how structure formed in the universe and the latest dark matter simulations make specific predictions about the DM density profile and the amount of substructure in halos ranging in size from dwarf galaxies all the way up to galaxy clusters. It is these simulations which motivated this thesis and they will be discussed in § 1.2. To put these simulations in context, I briefly discuss the latest results on the DM halos of dwarf and normal galaxies in § 1.3. Most observational work on dark matter halos has been done at the dwarf galaxy scale and has already presented challenges to the currently favored Cold Dark Matter (CDM) paradigm. Finally, we will discuss the current observational methods for measuring the dark matter density profile in galaxy clusters and the latest observational results (§ 1.4) which will inform the discussion presented in the following chapters of this thesis. This chapter will conclude with a paragraph discussing the structure of this thesis.

1.1 Observational Evidence for Dark Matter

The probable necessity for dark matter dates to the mid-1930's following observations of the kinematics of galaxies in the Coma Cluster (Zwicky, 1937). The results of Zwicky's observations were verified in other local galaxy clusters, such as Virgo (e.g. Smith 1936). Equally important, observations of the rotation curves of disk galaxies also called for some other form of matter besides the luminous matter (e.g. Rubin et al. 1980). In this section I will briefly present these two historical observations and the arguments traditionally used that have pointed to the necessity for dark matter.

It is thought that massive objects such as galaxies and clusters of galaxies are gravitationally bound systems in equilibrium. There are two lines of evidence that suggest this. First, the distribution of galaxies in clusters is often characterized by an increase in the space density of galaxies towards the cluster center with the density decreasing steadily outwards to that of the background, approximating the profile of an isothermal gas sphere, which is expected for a system in hydrostatic equilibrium. Another argument suggesting that clusters are in a gravitationally bound equilibrium follows by comparing the crossing time of a typical cluster galaxy with the age of the universe. The crossing time is

$$t_{cr} \sim R/\langle v \rangle \tag{1.1}$$

where R is the size scale of the cluster and $\langle v \rangle$ is the velocity dispersion of the consituent galaxies in the cluster. For example, a galaxy cluster with radius ∼1 Mpc and velocity dispersion $10^3 km/s$ has a crossing time of ∼1 Gigayear. Since the age of the universe is greater than ∼10 Gigayears, it is safe to assume that typical galaxy clusters are gravitationally bound objects, because if they were not, the system would have flown apart by now. If the cluster is in gravitationally bound equilibrium then it must obey the virial theorem, which simply states

$$T = 1/2|U| \tag{1.2}$$

where T is the total kinetic energy and $|U|$ is the total potential energy. Translating this into more usable terms for an observational astrophysicist (including the need to take into account the fact that normally velocities can be measured only along the line of sight), we get the following relation for the mass of an object that is in virial equilibrium:

$$M = 5\langle v_{||}^2 \rangle R/G \tag{1.3}$$

where $\langle v_{||}^2 \rangle$ is the line of sight velocity dispersion. Therefore, by measuring the velocity dispersion of galaxies within a cluster out to high radii, one can accurately estimate the mass of the galaxy cluster. As was mentioned previously, this was first done by Zwicky (1937) for the Coma cluster and Smith (1936) for the Virgo cluster. Both Zwicky and Smith's results were quite surprising. For example, if we assume some plausible values for the Coma cluster, that it has a radius of 3 Mpc and velocity dispersion of 1000 km/s, along with the fact that the cluster has an optical luminosity of $5 \times 10^{12} L_\odot$ then we would conclude that it has an optical mass-to-light ratio of over 600! Typical M/L for elliptical and S0 galaxies in the local universe are ∼10-15, leading to the direct conclusion that there is much more matter present in clusters than is visible in optical light. Even after taking into account other forms of baryonic matter (e.g. the hot intracluster medium) and the shortcomings of this order of magnitude calculation, the discrepancy between the observed, luminous mass in clusters and that inferred through gravitational interactions is great.

A further observation that leads to the conclusion that some form of dark matter is necessary comes from the rotation curves of disk galaxies. By measuring the rotational velocity of stars (or, if one wants to go even further out, of gas) about the galaxy's center as a function of radius, an estimate of the mass distribution can be made. Up until the 1950's and 1960's, the rotation curves of galaxies did not extend out to radii well beyond those of the stars, and had characteristics that were roughly compatible with a constant M/L, indicating that no dark matter was necessary. It was pointed out by Roberts (1975) that these early rotation curves were inadequate to probe the outer mass distribution of spiral galaxies. However, hints began to appear that suggested there was more mass in spirals than met the eye. In an extended optical rotation curve of M31 out to 24 kpc, Rubin & Ford (1970) noted that the total mass continued to quickly increase despite the steep falloff in stellar brightness at high radii. As observations improved, it became apparent that nearly all rotation curves increase at low radii, reach a peak, and then flatten out to the limits of the observations (Figure 1.1), which when using the 21cm line as a kinematic tracer, can extend far beyond the edge of the visible stellar disk (for an early realization of this, see Rogstad & Shostak 1972). Excellent quality rotation curves of hundreds of spiral galaxies all indicate (unless the galaxy is significantly disturbed) that they are flat out to the limits of the observations (e.g. Bosma 1978; Rubin et al. 1980, 1985).

Fairly simply, one can see what the physical implications of flat rotation curves are on the distribution of mass in galaxies. Using Gauss' theorem and Newton's law of gravity, along with making the assumption that the galaxy we are dealing with is spherically symmetric (unrealistic, but fine for this illustration), we find

$$M(\leq r) = v_{rot}^2 r/G \tag{1.4}$$

where $M(\leq r)$ is the mass enclosed within a given radius, r, and v_{rot}^2 is the rotation speed of the galaxy at a given radius. If the rotation curve is flat as a function of

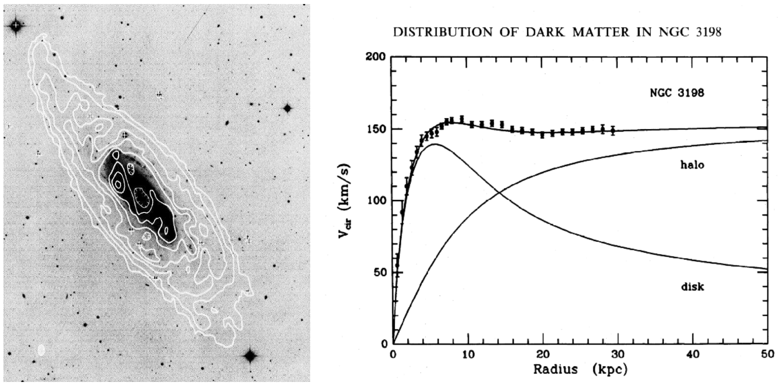

Figure 1.1: **Left:** Neutral hydrogen contours overplotted on an optical image of the spiral galaxy NGC 3198. **Right:** The measured rotation curve of NGC 3198 from neutral hydrogen. Note the rapid rise followed by a peak which flattens out to the limits of the observations. The shape of this rotation curve is typical for spiral galaxies. This figure is from van Albada et al. (1985).

radius, then $M(\leq r) \propto r$ and the mass increases linearly with radius, unlike the light distribution of disk galaxies, which fall off exponentially (Freeman, 1970). This implies that the M/L ratio of disk galaxies must increase with increasing radius, a finding that cannot be reconciled with the data unless some form of dark matter is invoked.

The high velocity dispersion in galaxy clusters and the flat rotation curves of spiral galaxies are just two of the many observational facts which lead to the conclusion that dark matter is necessary. By the late 1970's, it was quite clear that there were significant quantities of dark matter in spiral galaxies and clusters of galaxies, with some hints that dark matter was also present in elliptical galaxies (for a review at the time, see Faber & Gallagher 1979). Dark matter is now completely incorporated into modern thought on how galaxies and clusters form and evolve (e.g. Blumenthal et al. 1984). One of the best tools for studying this in more detail is through numerical simulations, which will be discussed in the following section.

1.2 Predictions from Simulations of Structure Formation

The current standard picture for how structures such as galaxies and clusters of galaxies formed combines an inflationary Universe with the hierarchical growth of small fluctuations in the initial cosmic mass distribution. This picture includes not only baryonic matter but also some kind of non-baryonic dark matter (in addition to some dark energy). Focusing on the topic of this thesis, dark matter, it should be noted that this dominant mass component in the universe remains unkown. Throughout the years, numerous properties of the dark matter particle and its consquences for structure formation have been explored, including warm dark matter (e.g. Hogan & Dalcanton 2000), scalar field dark matter (e.g. Peebles 2000), and self-interacting dark matter (e.g. Spergel & Steinhardt 2000). However, both because it accurately reproduces the large scale structure of the universe and because it is the dark matter candidate most in line with expectations from particle physics theory, the Cold Dark Matter (CDM) model (first coined by Peebles 1982) dominates current astrophysical theories.

Cold Dark Matter is collisionless, both with itself and with normal baryons, and nonrelativistic (hence 'cold'). Cold dark matter generally forms halos which are triaxial, have dense cores and have significant amounts of gravitationally bound substructure. The Cold Dark Matter paradigm is extremely successful at explaining the universe on large scales (> a few Mpc; Spergel et al. 2003; Croft et al. 2002; Bahcall et al. 2003). This is not to say that the Cold Dark Matter paradigm does not have its weaknesses, but it is the current dark matter candidate with the fewest by far. Alternatives to the standard CDM paradigm are possible that agree with large scale structure observations but have different properties on scales less than a megaparsec or so and are occasionally invoked when a set of observations appears to disagree with CDM. For example, the so-called self-interacting dark matter candidate (Spergel & Steinhardt, 2000) has a non-negligible cross section with itself and so on small scales would tend to produce halos which are rounder and have less dense cores. However, the self-interacting dark matter scenario may be ruled out by the ellipticity of dark matter halos inferred through strong lensing (Miralda-Escudé, 2002) and estimates of the self-interaction cross section obtained through cluster-cluster mergers (Markevitch et al., 2004). We will focus in the rest of this section on Cold Dark Matter (CDM) and the findings of numerical simulations given a CDM dominated universe on relatively small scales, such as that of galaxies and galaxy clusters (less than a few Mpc). It is on these scales that the dark matter is strongly nonlinear and slight differences in inherent properties can have large consequences for the central regions of halos.

The standard tool for predicting the properties of a universe dominated by CDM is the numerical simulation. These simulations are traditionally straightforward since gravity is the only physics involved for dark matter. The limitation is always CPU power in order to get the force resolution necessary to study the very inner regions of dark matter halos. Early high-resolution simulations of cold dark matter halos were performed by Frenk et al. (1988); Dubinski & Carlberg (1991); Warren et al. (1992) whose work studied the structural properties of the halos, including their core radii, density profiles, and distribution of shapes. However, these studies were limited by the number of particles and their dynamic range, due mostly to the limits of computation power at the time.

The series of papers that has given rise to the current era of detailed study and comparison of CDM halos in simulations with observations were performed by Navarro et al. (1996, 1997). In this work, Navarro et al. studied many DM halos with varying mass at relatively low resolution, suggesting that dark matter halos ranging in size from dwarf galaxies all the way up to galaxy clusters have a universal density profile, which looks like

$$\rho_d(r) = \frac{\rho_c \delta_c}{(r/r_{sc})(1+(r/r_{sc}))^3} \tag{1.5}$$

where ρ_c is the critical density of the universe, δ_c is the scale of the dark matter halo, and r_{sc} is some scale radius. Within the scale radius, the DM density

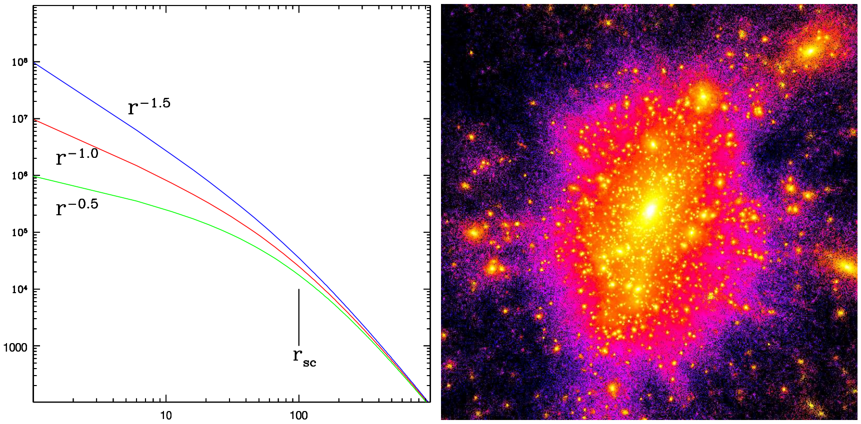

Figure 1.2: Left Panel– An illustration of the form of the generalized-NFW density profile with different inner slopes. An observationally derived value of β somewhere in between 1.0 and 1.5 would indicate agreement between numerical simulations and observations, while any other value would indicate a need to revise the current form of the Cold Dark Matter paradigm. Right Panel–A dark matter only, high resolution simulation of a galaxy cluster with approximately the mass of the Coma cluster, obtained from the web site of the University of Washington numerical computing web site.

asymptotes to $\rho \propto r^{-1}$, while external to r_{sc}, $\rho \propto r^{-3}$. The Navarro-Frenk-White (NFW) dark matter density form has become one of the basic predictions of the CDM paradigm, despite the fact that more recent work has slightly amended their results. This landmark work has led to an avalanche of theoretical, numerical, and observational papers which seek to refine, understand, and test this basic result.

As CPU power and numerical methods have progressed, larger and larger numbers of particles have been used to simulate dark matter halos. The convergence of the simulations has been tested and better understood. Soon after the NFW results, Moore et al. (1998) used higher resolution simulations and suggested that the inner DM slope asymptoted to $\rho \propto r^{-1.5}$, slightly steeper than the original NFW. Moore's work was followed by many others, all with improved resolution, but with relatively few overall halos. The consensus appeared to be that the DM density profile asymptoted somewhere between $\rho \propto r^{-1.0}$ and $\rho \propto r^{-1.5}$ (Fukushige & Makino, 1997; Ghigna et al., 2000; Jing & Suto, 2000; Moore et al., 1999b). This variation in inner slope has led to the use of a more generalized form of the NFW profile

$$\rho_d(r) = \frac{\rho_c \delta_c}{(r/r_{sc})^{\beta}(1 + (r/r_{sc}))^{3-\beta}} \tag{1.6}$$

This density profile asymptotes to $\rho \propto r^{-\beta}$ well within r_{sc} and $\rho \propto r^{-3}$ well outside of it. The generalized NFW DM density profile parameterization is used throughout this thesis to compare the inner slope seen in simulations with that observed in galaxy clusters (see Figure 1.2). An observationally derived value of β somewhere between 1.0 and 1.5 would indicate agreement between numerical simulations and observations, while any other value would indicate a need to revise the current form of the Cold Dark Matter paradigm.

The very latest generation of CDM-only simulations have over one million particles per DM halo in order to resolve the density profile to within 1% of the virial radius. These simulations seem to indicate that the inner slope does not asymptote to a particular value but becomes progressively shallower at smaller radii, with the logarithmic derivative being between -1 and -1.5, as seen in lower resolution simulations. In addition, enough of these high-resolution halos are being simulated that the scatter in density profiles can be determined across mass scales (Fukushige et al., 2004; Navarro et al., 2004; Reed et al., 2003; Tasitsiomi et al., 2004). This may be the ultimate limit of DM only simulations. Even given that a suite of these simulations takes several months of dedicated supercomputer time, to probe the DM halo further requires an equally good knowledge of the baryonic matter and its effect on the overall density profile. The future of CDM simulations must include an accurate representation of the baryonic matter as well. Without it and the physics that baryons contribute, it will be impossible to accurately compare the very inner density profiles of observed and simulated halos.

Along these lines, hydrodynamic simulations of galaxy clusters that include baryonic physics in conjunction with dark matter are rapidly advancing, taking into account radiative cooling, star formation, and supernova feedback processes (Borgani et al., 2004; Nagai & Kravtsov, 2005; Kravtsov et al., 2005), although problems still remain in producing the basic properties of galaxy clusters (e.g. Borgani et al. 2004). More current simulations try to gauge the effect baryons have on dark matter profiles. Since baryons tend to cool and collapse, their very presence in the center of dark matter halos should serve to steepen the density profile and possibly even make the generalized NFW form invalid (Gnedin et al., 2004). The effects that cooled baryons have on the ultimate distribution of the central portions of dark matter halos are one of the most exciting avenues of current numerical simulation work.

It should be noted that there are other predictions for dark matter halos which arise from CDM numerical simulations besides the universal density profile. For instance, there are specific predictions on the number of satellite dark halos surrounding and interacting with a parent halo. Known as the substructure problem, it has been noted that the number of dwarf galaxies surrounding normal galaxies such as our own are far too few in number to be compatible with the number seen in numerical simulations (Moore et al., 1999a). However, due to the difficulty of forming stars in low mass dark matter halos, this is still a subject of vigorous debate both observationally and theoretically.

1.3 The Dark Matter Density Profile on the Dwarf and Normal Galaxy Scale

The mass regime in which the dark matter density profile has been studied most extensively is at the dwarf galaxy scale. Dwarf galaxy mass distributions can be inferred by measuring the rotation of either the gas with HI or using the stellar $H\alpha$ emission line. The reason that dwarf galaxies are considered promising candidates for testing the dark matter density profile predictions from simulations is that they are thought to be dark matter dominated into the very central regions of the galaxy, with the baryonic mass seen in stars being a minority component. This leads to two advantageous consequences: 1) The mass of stars and gas contribute little to the actual observed rotation curve and are instead a direct manifestation of the inner dark matter halo and 2) the cooling and collapse of baryons during disk formation will not alter the underlying dark matter structure significantly since the total mass in baryons is small.

Initial HI observations of dwarf galaxies yielded rotation curves which were well described by dark matter halos with a core rather than a cusp (e.g. de Blok & McGaugh 1997 and references within), leading to an apparent crisis for the CDM model (e.g. Flores & Primack 1994; Moore 1994). However, the flat-cored DM results utilizing HI synthesis observations have been called into question due to the effect of beam smearing. Both due to intrinsically mediocre angular resolution and the need to bin the data to get higher signal to noise, the typical effective beam size used for HI observations is tens of arcseconds across, which is too large to accurately probe the very inner regions of these dark matter halos. Indeed, this limited spatial resolution in the inner regions of the halo seems to systematically bias results towards flatter inner DM slopes (van den Bosch & Swaters, 2001).

More recent work has focused on long-slit $H\alpha$ emission line observations. These observations can be of relatively high resolution depending on the ground-based site and their effects can be modeled relatively easily in the analysis, making $H\alpha$ rotation curves a superior dark matter density probe. Again, initial results indicated that dwarf galaxies have rotation curves which are consistent with flat-core dark matter halos, although some could be described with a cuspy profile (de Blok et al., 2001; Borriello & Salucci, 2001; de Blok & Bosma, 2002; de Blok et al., 2003). And again, these results have been called into question after additional, more thorough analyses have been performed. For example, Swaters et al. (2003) have taken into account several observational and geometric systematic effects associated with the modeling of observations such as noncircular motions, galaxy inclination, slit width, seeing and slit alignment errors and have concluded that dark matter slopes as steep as that seen by NFW can not be ruled out by the current set of data. Additionally, Rhee et al. (2004) and Hayashi et al. (2004b) have performed simulated observations of simulated dark matter halos and have also concluded that many rotation curves that appear to be caused by flat cored dark matter halos actually originate from cuspy halos which are triaxial or have some other dynamical complication. These issues remain a matter of some debate (de Blok, 2005).

Much work has gone into the dark matter profile at the normal galaxy scale as well. Unlike with dwarf galaxies, however, baryons play an important role in the inner regions of the halos, making it necessary to disentangle luminous and dark matter with multiple mass tracers and possibly to take into account the gravitational effects that the baryonic halo may have on the dark matter halo. Degeneracies inevitably remain.

For elliptical galaxies, one can use gravitational lensing or dynamics (or both) to probe the mass profile. For local galaxies dynamics can be used, and while dark matter often appears to be necessary, it is difficult to ascertain its properties given the influence of baryons and the uncertainties surrounding stellar orbits (e.g. Rix et al. 1997; Gerhard et al. 2001). At higher redshift, it is possible to combine lensing and dynamics. For example, the Lensing and Dynamics Survey has sought to understand the relative properties of dark and luminous matter in ellipticals as a function of redshift using both strong gravitational lensing and the velocity dispersion profile of the central lens galaxy (Treu & Koopmans, 2004; Koopmans & Treu, 2002, 2003; Treu & Koopmans, 2002, 2003). They can place strong constraints on the density profile of the dark matter alone only if the orbits of the stars are understood (γ is between 0.9 and 1.5, in accordance with the CDM paradigm, if the stellar orbits are isotropic, where the inner DM density goes like $\rho \propto r^{-\gamma}$). They have robustly determined the total (as opposed to just dark or luminous) mass density profile in their sample of 5 ellipticals with both lensing and velocity dispersion data to be slightly shallower than isothermal, along with an root mean square scatter of $\gamma \sim 0.3$. A fair comparison with the CDM paradigm must wait until star formation is robustly incorporated into numerical modeling.

The same conclusion can be drawn for normal spiral galaxies, which are also dominated by a baryonic component at small radii. For these systems, the rotation curve evidence is inconclusive about the slope of the dark matter halo, with the major degeneracy being between the stellar disk M/L and the dark halo profile. In two separate studies, Jimenez et al. (2003) and Barnes et al. (2004) could not distinguish between or could not find good fits for different models of the dark matter in their high resolution rotation curves of disk galaxies. Dutton et al. (2005) have presented a thorough discussion of the pitfalls and degeneracies involved in trying to infer the inner dark matter slope from rotation curves of disk galaxies.

The differing and controversial results at the dwarf and normal galaxy scale highlight the fact that the predictions of CDM must be tested at multiple mass scales. It is apparent that the debate on the inner slope of dwarf and normal galaxy halos will be contentious for some time and that it will be fruitful to look at the inner slope question at the galaxy cluster scale as well.

1.4 Measuring the Dark Matter Density Profile in Clusters

As we have seen, the Cold Dark Matter paradigm for structure formation has faced some hurdles on the dwarf to normal galaxy scale. But what about on the scale of galaxy clusters? Numerical simulations predict that the "universal" DM profile applies to clusters as well, meaning that the CDM paradigm will not be fully investigated until the DM density profile in clusters is well characterized. While in systems such as the local group there appear (without taking into account the inefficiency of star formation in such low mass objects) to be far fewer satellite galaxies then are expected from CDM simulations, the same is not true in clusters of galaxies. In clusters, the number of satellite galaxies seems to be in agreement with simulations (Moore et al., 1999a). However, the jury is still out on the slope of the inner dark matter density profile in clusters, which is the focus of this thesis.

One of the great advantages of working at the galaxy cluster scale is that there are several density measurement techniques that can trace the DM distribution from small scales (brightest cluster galaxy dynamics; Kelson et al. (2002)) to intermediate scales (strong gravitational lensing; e.g. Broadhurst et al. (2005a) and out to the virial radius (weak lensing; e.g. Kneib et al. (2003)). It is also possible to use both X-ray analyses of the intracluster medium (ICM; e.g. Arabadjis et al. (2004)) and the velocity dispersion profile of the cluster galaxies themselves (e.g. Łokas & Mamon (2003)). This lends itself to using multiple techniques simultaneously and to direct comparisons between methods so that systematics can be understood and corrected for. I will spend the remainder of the chapter describing the three main mass measurement techniques utilized at the galaxy cluster scale: gravitational lensing, galaxy and stellar dynamics, and X-ray measurements of the intracluster medium (ICM) assuming hydrostatic equilibrium. Each of these techniques has its strengths and weaknesses which I will touch on in these subsections and throughout this thesis.

1.4.1 Gravitational Lensing

The great strength of using gravitational lensing to probe the mass density profile of clusters is that lensing can measure mass without regard to the dynamical state of the cluster. This strength, however, is also its weakness. Since lensing cannot distinguish between light and dark mass components, another mass tracer is needed to disentangle luminous from dark matter.

Here we present some basics of strong gravitational lensing. For a more in depth discussion, the reader is referred to Schneider et al. (1992); Blandford & Narayan (1992); Narayan & Bartelmann (1996), which were also used as sources in what follows. Also, a more detailed account of multiple image modeling and interpretation is presented in Chapter 5.

In a gravitational lensing system, light from a distant object (the “source”) is deflected by the gravitational potential of an intervening object (the “lens”) on its way to the observer. In some situations, the gravitational potential of the lens causes deflections which produce more than one image of the same background source (a multiply imaged system). It is these situations which define the strong lensing regime and what will be dealt with in this thesis. Throughout this discussion, the reader is referred to Figure 1.4.1 for a schematic of a typical strong gravitationally lensed system.

Looking at Figure 1.4.1, and keeping in mind that the angles we are dealing with are small, it is easy to determine the reduced deflection angle

$$D_{ds}\vec{\hat{\alpha}} = D_s\vec{\alpha} \tag{1.7}$$

and from that the "lens equation":

$$\vec{\beta} = \vec{\theta} - \vec{\alpha}(\vec{\theta}) \tag{1.8}$$

It must be kept in mind that the distances D_s, D_{ds}, and D_l are angular diameter distances and that in general D_s does not equal $D_{ds} + D_d$. The distribution of mass in the lens determines the deflection angle $\vec{\hat{\alpha}}$. The simplest mass distribution to consider is that of a point mass, which has a deflection angle (according to general relativity) of

$$\hat{\alpha} = \frac{4GM}{c^2\xi} \tag{1.9}$$

where G is Newton's gravitational constant, c is the speed of light, and M is the mass of the point mass. The real world presents us with more complex mass distributions, however, with different masses and distances to the light ray. In most astrophysical situations (all considered in this thesis) the region over which the light rays are being bent is much smaller than the distances between the observer and lens and between lens and source. Given this, the mass distribution of the lens can be projected along the line of sight and approximated as a single "lens plane." We can then write the surface mass density, $\Sigma(\vec{\xi})$, as

$$\Sigma(\vec{\xi}) = \int \rho(\vec{\xi}, z)dz \tag{1.10}$$

where $\rho(\vec{\xi}, z)$ is the three-dimensional mass density of the lens and the integral is along the line of sight. Therefore to extend the deflection angle for a point mass

(Equation 1.9) to that of a smooth surface mass distribution, we can integrate over the entire lensing plane to get

$$\vec{\hat{\alpha}}(\vec{\xi}) = \int \frac{4G\Sigma(\vec{\xi'})(\vec{\xi} - \vec{\xi'})}{c^2|\vec{\xi} - \vec{\xi'}|^2} d^2\xi' \tag{1.11}$$

which effectively is the sum of the deflections due to many point masses.

A special situation arises when the background source and the lens are collinear, that is, β=0. In this instance, for elliptical or circular lens, the background source is lensed into a ring known as an Einstein Ring. The radius of the Einstein ring, along with the redshift of the source and lens, provides a robust measure of the mass enclosed within the ring. As an example, if we again take the point mass lens (Equation 1.9), and combine with the lens equation (Equation 1.8), with β=0, then we get the following relationship between the mass enclosed and the angle subtended by the ring

$$M_E = \theta_E^2 \frac{c^2}{4G} \frac{D_d D_{ds}}{D_s} \tag{1.12}$$

for circularly symmetric lenses this is a generic result, the Einstein ring always measures the mass enclosed, and this is nearly true for the elliptical case as well. The Einstein radius, θ_E, also provides a good length scale for gravitational lensing. For multiple imaging systems (those that aren't necessarily lensed into Einstein rings) the typical separation between images is $\sim 2\theta_E$. The mean surface mass density within the Einstein ring is called the critical density where

$$\Sigma_{cr} = \frac{c^2}{4\pi G} \frac{D_s}{D_d D_{ds}} \tag{1.13}$$

and is a common scaling factor in lensing analyses.

The modeling of strongly gravitationally lensed systems can provide key information on the potential and mass distribution of the lens. The angular position and radius of background source images is highly dependent on the surface mass distribution of the lens (see Equation 1.11), which is usually represented as a parameterized mass model with ellipticity, position angle, and a radial profile. The

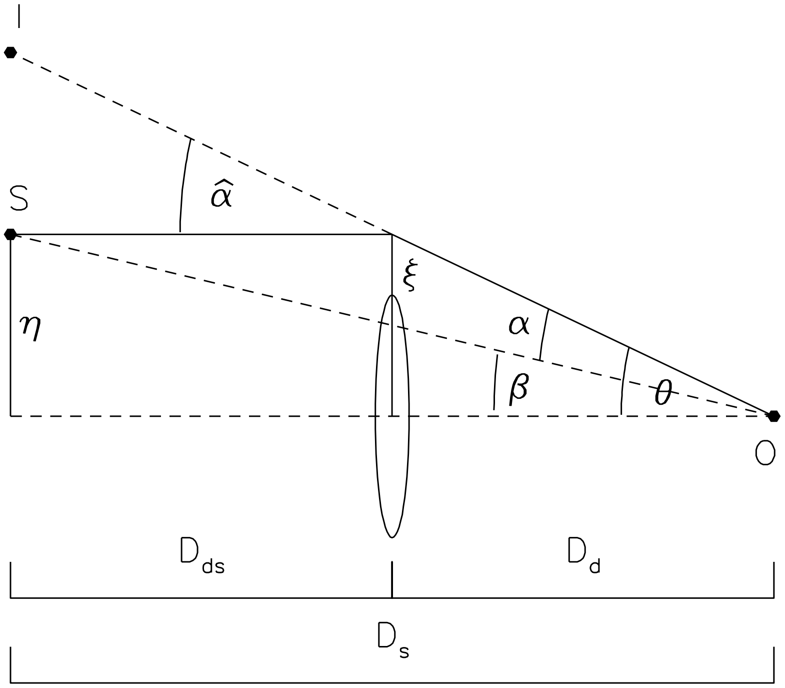

Figure 1.3: A schematic illustrating gravitational lensing. This figure has been reproduced from Narayan & Bartelmann (1996) and is a schematic of a typical strong gravitational lens system. See text for a discussion.

parameters of these lens models can be varied, and the expected image positions can be found by solving the lens equation. By comparing the expected image positions for the model with the observations, constraints on the parameterized lens model can be found. We will discuss the modeling of lenses and the constraints that they can provide in Chapter 5.

Lensing has long been recognized as a tool for probing the mass density profile of clusters. For example, even in the early 1990's, it was recognized that cluster MS2137 (which will be studied in several chapters of this thesis) would place tight constraints on the mass profile (Fort et al., 1992; Mellier et al., 1993). Remarkable lenses such as Abell 2218 also provided constraints on the mass profile due to the sheer number of gravitational arcs seen (Kneib et al., 1996). One of the earliest attempts to compare the NFW dark matter profile with that of actual lensing data in a cluster was performed by Tyson et al. (1998), where they found the slope to be shallower than that predicted, although that result turned out to be controversial (Broadhurst et al., 2000).

New results on the lensing front have been very exciting with quantitatively better data and methods being continuously developed. Perhaps the most exciting recent strong lensing results have come out of the Advanced Camera for Surveys Guaranteed Time Observations team and their deep imaging of the galaxy cluster Abell 1689 where over 100 multiple images have been identified (Broadhurst et al. 2005b; see Figure 1.4.1). No thorough analysis of the inner dark matter slope has been made for this cluster yet, with the existing analysis focusing only on the NFW profile, although such an analysis would be very interesting. A particular area of growth has been combining strong and weak lensing analyses. Three recent studies stand out in particular; that done for the clusters Cl0024 (Kneib et al., 2003), MS2137 (Gavazzi et al., 2003) and Abell 1689 (Broadhurst et al., 2005a). The combination of weak and strong lensing is particularly powerful since it can probe the density profile from ∼10 kpc scales out to ∼1 Mpc, allowing both the inner and outer density profile to be probed and any degeneracy between the two (due to projection effects) to be partially mitigated. Quite interestingly, the Kneib et al. (2003) analysis of Cl0024 attempted to constrain the outer slope of the dark matter density profile, finding that it must fall off more steeply than $\rho \propto r^{-2}$, in accordance with CDM simulations. A further discussion of these techniques and the new ACS data will be presented in Chapter 6.

1.4.2 X-ray measurements of the ICM

The gas clouds from which galaxy clusters formed were heated by the energy of the initial gravitational collapse of the system. For massive systems such as galaxy clusters, these halos of hot gas are visible in the form of diffuse X-ray emission. All massive galaxy clusters are intense X-ray emitters, and this emission is identified as bremsstrahlung of the hot intracluster gas (the temperature of the gas is between approximately 10 and 100 million K). Discovered by the UHURU

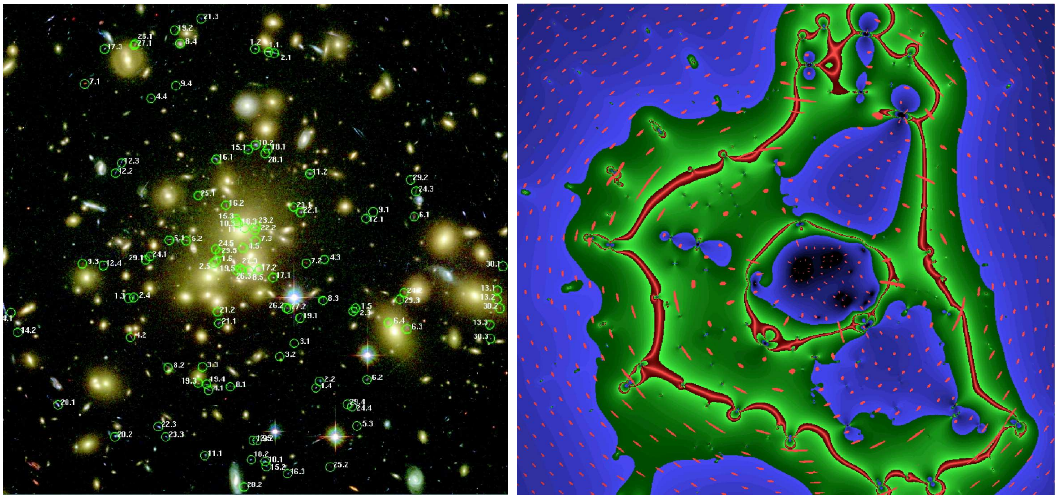

Figure 1.4: Left–The ACS composite image of the galaxy cluster Abell 1689. Over 100 images of background sources are identified in the image. Right–A map of the distortion and magnification induced by the best-fitting lens model of the cluster Abell 1689 calculated from the positions of the 106 multiple images.

X-ray Observatory, detailed, spatially extended measurements of nearby clusters with the EINSTEIN X-ray satellite could be made beginning in the late 70's. With the advent of the Chandra and XMM-Newton X-ray observatories, the study of the density profile in galaxy clusters with X-ray measurements is now routine and provides tight constraints on the mass profile, assuming that the necessary simplifications are valid.

In order to illustrate the utility of using X-ray data to constrain the mass density profile in galaxy clusters, I repeat the calculation presented by Fabricant et al. (1980) for M87 using EINSTEIN X-ray data. In a pioneering work, they showed that the emission of the gas provides a powerful probe of the cluster's gravitational potential. Two crucial assumptions are necessary for this formalism to work, each of which is certainly not true at some level. First, it has nearly always been assumed that the cluster is spherically symmetric. Second, the cluster must be in hydrostatic equilibrium; the pressure of the gas, dark matter and galaxies in the cluster must balance against the gravitational attraction of the cluster wishing to contract the system. It is still a matter of debate within the literature how grievous these assumptions are and whether they truly keep one from inferring the density profile of the cluster. Any number of situations would make the assumption of hydrostatic equilibrium invalid, most obviously if the cluster were undergoing a major cluster-cluster merger or if the central AGN of the BCG were a significant heat source in the inner regions of the cluster.

If we take p as the pressure of the gas and ρ as its density (which can vary with position in the cluster), the equation for hydrostatic equilibrium reads,

$$\frac{dp}{dr} = -\frac{GM(< r)\rho}{r^2} \tag{1.14}$$

where G is Newton's gravitational constant and $M(< r)$ is the mass enclosed within the sphere of radius r. Using the Ideal Gas Law,

$$p = \frac{\rho k_B T}{\mu m_H} \tag{1.15}$$

where m_H is the mass of the hydrogen atom and μ is the mean molecular weight (normally taken to be μ=0.6 for a fully ionised gas), and differentiating by r, we have

$$M(< r) = -\frac{k_B T r^2}{G\mu m_H}\left[\frac{d(log\rho)}{dr} + \frac{d(logT)}{dr}\right] \tag{1.16}$$

Thus, if one had measurements of the gas density and temperature as a function of radius, then one could determine the mass distribution of the cluster. Typically, the X-ray image is split up into a series of circular, concentric annuli, with the spectrum of each annulus compared to a plasma model to infer the gas density and temperature. Attempts are often made to deproject the data using an "onion peeling" technique (Buote, 2000). Then, parameterized models are fit to the gas density and temperature profile so that the derivatives in Equation 1.16 are tractable. In this way, an enclosed mass profile is calculated and compared to expectations from CDM (see Figure 1.4.2 for an illustration). It must be noted that this technique is really only sensitive to the total mass enclosed within a given radius and is unable to disentangle luminous from dark matter on its own. Normally this concern is dismissed because it is believed that galaxy clusters are dark matter dominated, however there is some indication that in the very central regions of galaxy clusters the brightest cluster galaxy may be a significant contributor to the total mass. Therefore, conclusions about the dark matter slope based on an X-ray analysis alone may need further verification.

The study of galaxy clusters in the X-ray has made great strides with the advent of the Chandra and XMM-Newton X-ray telescopes. With superb sensitivity and angular resolution (the resolution of the Chandra Observatory is roughly one arcsecond, comparable to ground-based optical images), along with spatially resolved spectra, these telescopes have uncovered a wealth of interesting phenomena in cluster cores. In particular, new high resolution observations that the hot gas in cluster cores is often highly disturbed, exhibiting filaments and holes possibly related to an AGN in the central galaxy, calls into question the standard assumption of hydrostatic equilibrium necessary to perform the mass density analysis described above. Indeed, it is also observed that a high fraction of galaxy clusters appear to be undergoing significant mergers, again calling into question the assumption of hydrostatic equilibrium.

Nonetheless, much X-ray work has been done with the mass density of clusters, with an array of results on the inner slope of the DM halo. Studies have found values of the logarithmic slope, β, of the DM halo ranging from $\beta \sim 0.6$ (Ettori et al., 2002) through $\sim$1.2 (Lewis et al., 2003) to $\sim$1.9 (Arabadjis et al., 2002). This can either mean that the DM density profile in clusters exhibits a wide range of inner slope, some of which are in conflict with CDM simulations, or that the assumption of hydrostatic equilibrium is not valid. One promising avenue which perhaps can avoid questions about the hydrostatic equilibrium of clusters has been undertaken by David Buote's group at the University of California Irvine. Their group is studying clusters which not only appear relaxed on 100 kpc - 1 Mpc scales, but which also do not harbor a central AGN in their central galaxy. Using this tactic, they seek to avoid clusters which seem to obviously not be in hydrostatic equilibrium. In the work presented so far, for the clusters Abell 2029 and Abell 2589, they have found that the total matter density profile in these systems has a inner logarithmic slope of β between 1.0 and 1.5, in accordance with CDM simulations. However, on the scales on which they are probing the mass distribution, the mass of the central BCG is also crucial, and their failure to model and subtract out its mass may lead to an overestimate of the steepness of the inner DM slope (see Figure 1.4.2).

1.4.3 Dynamics

The final method useful for probing the density profile in galaxy clusters is through the velocity dispersion profile of the cluster galaxies themselves within the cluster potential or, on smaller scales, simply using the velocity dispersion profile of the stars in the central BCG. Perhaps the best studied cluster is the Coma cluster. The classic work of Kent & Gunn (1982) initially assembled ~300 galaxy radial velocities. Later, Merritt (1987) illustrated that if a realistic amount of freedom is built into the models (if mass did not follow light, for example), then there is a strong degeneracy between the dark matter distribution and the velocity anisotropy of the system. In fact, it is this degeneracy which continues to limit the ability of galaxy dynamics alone to constrain the dark matter profile in clusters.

The basic calculations for inferring the mass density profile are similar whether one is looking at just the stars in the central BCG or are using the cluster galaxies themselves as tracers of the potential. The assumption of spherical symmetry is nearly always made because it greatly simplifies the computation of the line-of-sight velocity dispersion. The model velocity dispersion is computed starting from the spherical Jeans Equation (Binney & Tremaine, 1987):

$$\frac{d\rho_*(r)\sigma_r^2(r)}{dr} + \frac{2\alpha(r)\rho_*(r)\sigma_r^2(r)}{r} = -\frac{GM_{enc}(r)\rho_*(r)}{r^2} \tag{1.17}$$

where G is Newton's gravitational constant, $M_{enc}(r)$ is the three-dimensional mass enclosed, and σ_r is the radial velocity dispersion. The anisotropy parameter $\alpha(r)$ is defined as

$$\alpha(r) \equiv 1 - \frac{\sigma_\theta^2(r)}{\sigma_r^2(r)} \equiv \frac{r^2}{r^2 + r_a^2} \tag{1.18}$$

where σ_θ is the tangential component of the velocity dispersion. The final definition introduces the Opsikov-Merritt (Osipkov 1979; Merritt 1985a,b) parameterization of anisotropy that is often used in dynamical models. With this parameterization of the anisotropy, you can derive the radial velocity dispersion (Binney, 1980)

$$\sigma_r^2(r) = \frac{G \int_r^\infty dr' \rho_*(r') M_{enc}(r') \frac{r_a^2 + r'^2}{r'^2}}{(r_a^2 + r^2)\rho_*(r)} \tag{1.19}$$

and the projected velocity dispersion

$$\sigma_p^2(R) = \frac{2}{(M_*/L) I(R)} \int_R^\infty dr' \left[1 - \frac{R^2}{r_a^2 + r'^2}\right] \frac{\rho_*(r')\sigma_r^2(r')r'}{(r'^2 - R^2)^{1/2}} \tag{1.20}$$

with I(R) being the surface brightness profile either of the galaxy distribution in the cluster or of the BCG, depending on the measurement made. The projected velocity dispersion, σ_p, is the quantity measured at the telescope either by comparing the BCG absorption spectrum to broadened stellar templates or by measuring the galaxy velocity dispersion in different radial bins, depending on the program. Different observational effects may be taken into account in the analysis, with some discussion presented in Chapter 3.

Since it is difficult to compile the necessary radial velocities in one cluster, it is common to “stack” the results from many similar clusters. An NFW profile has been found to be consistent with the total mass distribution through this stacking technique, whether using the CNOC1 data set (van der Marel et al., 2000) or the ENACS survey (Biviano & Katgert, 2003), for example. No attempt was made to disentangle luminous from dark matter in these studies.

One study which did attempt to distinguish between luminous and dark matter by measuring the extended velocity dispersion profile of the BCG in Abell 2199 (and using archival radial velocities for the galaxies in the cluster) was performed by Kelson et al. (2002). The Kelson et al. observations are the current state of the art in measuring the extended kinematics of massive galaxies. Kelson et al. concluded that the BCG halo is dominated by dark matter outside of 20 kpc, making it necessary to model both the luminous and dark distributions simultaneously. When the model was applied, it was found that halos with an inner logarithmic slope as high as $\beta \sim 1.5$ were ruled out by the data, and those corresponding to an NFW profile ($\beta \sim 1.0$) would not work unless the stellar contribution of the BCG was unusually low (see Fig. 1.4.3). While this analysis stands out for its thoroughness, the authors did make the simplifying assumption that the stellar and galaxy orbits were isotropic. It is not clear that if anisotropy were introduced if the same results would be had.

1.5 Goals of this Thesis & Thesis Overview

When I set out on this thesis project, its basic goals were:

1. Measure the inner dark matter density logarithmic slope, β, on $\lesssim 100$ kpc scales in several galaxy clusters by disentangling luminous from dark matter using a combination of methods as discussed above.

2. Test the NFW hypothesis that the dark matter density is steeper than $\rho_{DM} \propto r^{-1}$ on these scales.

3. Make a preliminary measurement of the scatter in inner dark halo density profiles in order to verify if the profiles are universal.

This was an amibitious task. In the following I demonstrate a technique that constrains the inner dark matter density slope on these scales, with interesting results (see Chapter 5). But until this technique is performed on a larger sample of data, a comment on the scatter will have to wait.

This chapter was meant as a brief introduction to dark matter halos, both their theoretical and numerical incarnations and what is seen in actual observations. This thesis describes several different observational studies of the inner dark matter density profile in galaxy clusters as a test of the CDM paradigm for structure formation. Chapter 2 presents a combined analysis of the velocity dispersion profile of the brightest cluster galaxy and lensing in the galaxy cluster MS2137 in order to constrain the dark matter density profile in the cluster. Chapter 3 expands this type of analysis to a sample of galaxy clusters; three of which have both tangential and radial arcs and three which have only tangential arcs. Chapter 4 presents a systematic search of the HST/WFPC2 archive for gravitational arcs and use the number ratio of radial to tangential arcs to constrain the typical dark matter density profile in the galaxy cluster sample. In Chapter 5 a reanalysis of the combined lensing and dynamical constraints of the galaxy cluster MS2137 is presented. The major thrust of this reanalysis is incorporating elliptical lens models developed in the LENSTOOL software package into the mass modeling process, in order to more realistically model the mass components. Finally, Chapter 6 summarizes the material covered in this thesis and presents what can be done in the future to improve on current observations and modeling to better constrain not only the dark matter density profile in galaxy clusters but the total (dark plus baryonic) density profile from the very inner regions of the cluster out to the virial radius.

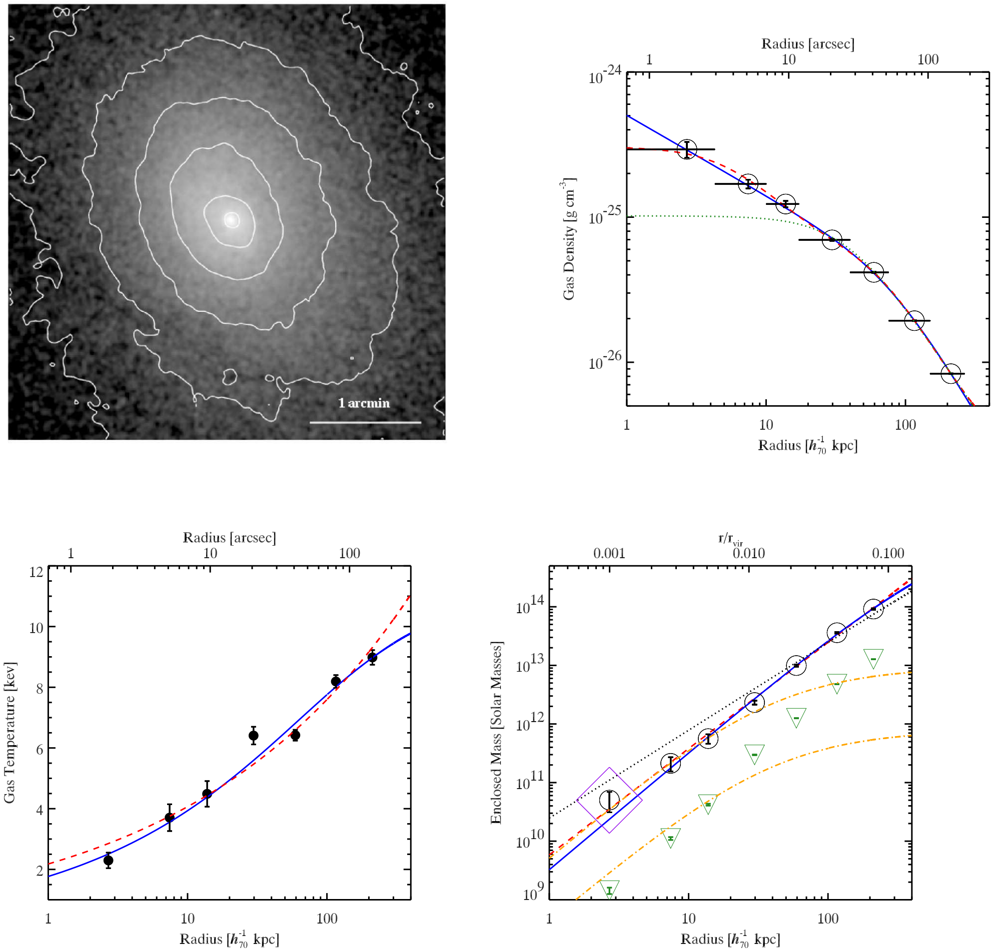

Figure 1.5: This four-part figure illustrates the basic observables and results typical for X-ray analyses of cluster mass distributions. Top Left–Chandra ACIS image of Abell 2029. Top Right–Radial gas density profile of Abell 2029 (large circles) fit to several standard parameterizations. This parameterized fit is then fed into equation 1.16, along with the temperature profile to calculate the enclosed mass profile. Bottom Left–The radial temperature profile of Abell 2029, again fit to a standard paramaterization to facilitate the hydrostatic equilibrium analysis. Bottom Right– Total enclosed cluster mass profile. The open circles are the data points and the lines are fits to the data, with the NFW profile being a very good fit. The upside down triangles show the contribution from the cluster gas mass. Note that the bright yellow band shows the possible contribution from the cluster BCG, illustrating the need for an additional technique to account for and disentangle this important mass component in order to understand the dark matter density profile. This figure has been reproduced from Lewis et al. (2002, 2003).

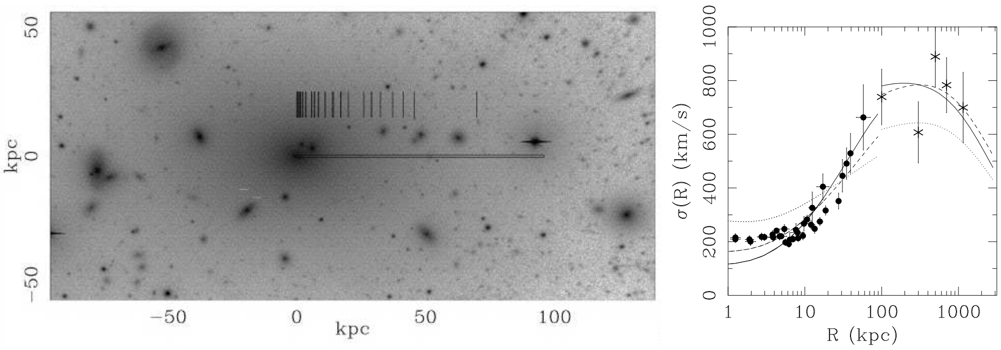

Figure 1.6: Left– An image of the BCG in Abell 2199 with the long slit position used by Kelson et al. (2002). Right– The observed velocity dispersion profile of the BCG in Abell 2199 along with cluster member kinematics. Dark matter halos that are as steep as an NFW profile are ruled out by the data.

Chapter 2

The Dark Matter Density Profile of the Lensing Cluster MS2137-23: A Test of the Cold Dark Matter Paradigm*

David J. Sand[a], Tommaso Treu & Richard S. Ellis

[a]Department of Astronomy, 105-24 California Institute of Technology, Pasadena, CA 91125, USA

Abstract

We present new spectroscopic observations of the gravitational arcs and the brightest cluster galaxy (BCG) in the cluster MS2137-23 ($z = 0.313$) obtained with the Echelle Spectrograph and Imager on the Keck II telescope, and find that the tangential and radial arcs arise from sources at almost identical redshifts ($z = 1.501, 1.502$). combine The measured stellar velocity dispersion profile of the BCG was combined with a lensing analysis to constrain the distribution of dark and stellar matter in the central 100 kpc of the cluster. Our data indicate a remarkably flat inner slope for the dark matter profile, $\rho_d \propto r^{-\beta}$, with $\beta < 0.9$ at 99% CL. Steep inner slopes obtained in cold dark matter cosmological simulations – such as Navarro Frenk & White ($\beta = 1$) or Moore (1.5) universal dark matter

---

*This chapter has been published previously as Sand et al. (2002)

profiles – are ruled out at better than 99% CL. As baryon collapse is likely to have steepened the dark matter profile from its original form, our data provides a powerful test of the cold dark matter paradigm at the cluster mass scale.

2.1 Introduction

A fundamental result arising from cold dark matter (CDM) numerical simulations is that the density profiles of DM halos are universal in form across a wide range of mass scales from dwarf galaxies to clusters of galaxies (Navarro, Frenk, & White, 1997). Internal to some scale radius r_{sc}, the dark matter profile assumes a power law form $\rho_d \propto r^{-\beta}$. While there is some dispute amongst the simulators about the precise value of β with values ranging from 1.0 to 1.5, (Moore et al., 1998; Ghigna et al., 2000; Power et al., 2003), a clear measurement of β in a range of objects would offer a powerful test of the CDM paradigm.

The largest observational effort in this respect to date has been via dynamical studies of low surface brightness (LSB) and dwarf galaxies, suggesting softer ($\beta < 1$) DM cores than expected on the basis of the numerical simulations (e.g. de Blok & Bosma 2002; Salucci & Burkert 2000), although the issue remains somewhat controversial (e.g. van den Bosch & Swaters 2001). Similar tests have recently been extended to regular spiral (Jimenez et al., 2003) and elliptical galaxies (Treu & Koopmans, 2002). Some observational constraints are available at the scale of massive clusters, from lensing (e.g. Tyson et al. 1998; Williams et al. 1999; Smith et al. 2001), X-ray analysis (e.g. Lewis et al. 2003), and dynamics of cD galaxies (Kelson et al., 2002). Since massive clusters probe a totally different scale and physical conditions than galaxies, it is crucial to understand their mass distribution to test the universality of the DM profiles.

In this paper we present the first application of a new method to determine the luminous and dark mass distribution in the inner regions of massive clusters with giant arcs around a central BCG. The method combines lensing analysis with stellar kinematical measurements of the BCG. The two ingredients provide complementary information on the relevant scales ($\sim$ 100 kpc), allowing us to disentangle the luminous and dark components of the total mass distribution.

We have chosen the cluster MS2137-23 as a first application of our method since it is an approximately round system, has an isolated BCG and a very well-studied arc system. Fort et al. (1992) first pointed out the potential significance of the radial and tangential gravitational arcs as a means of constraining the mass distribution on $\simeq$100 kpc scales, and mass models have been developed subsequently (Mellier et al., 1993; Hammer et al., 1997, hereafter M93, H97). The redshifts of the radial and tangential arcs were predicted to lie in the range $1< z <2$ (M93). A key issue in the earlier work is whether the radial arc is, in fact, a lensed feature. M93 and Miralda-Escude (1995, hereafter ME95) also point out the importance of determining the stellar velocity dispersion profile of the BCG to weigh the stellar contribution to the mass.

Following the earlier suggestions, we present new observations of the cluster MS2137-23 with the Keck II telescope. We provide spectroscopic confirmation of the arcs and measure a velocity dispersion profile for the central BCG. The spectroscopic data are used together with archival HST images to constrain the luminous and DM distribution of the cluster. In the following, r is the radial coordinate in 3-D space, while R is the radial coordinate in 2-D projected space. We adopt H_0=65 km s^{-1},Mpc^{-1}, $\Omega_m = 0.3$, and $\Omega_\Lambda = 0.7$ for the cosmological parameters.

2.2 Observations

2.2.1 Keck Spectroscopy

We observed MS2137-23 using the Echelle Spectrograph and Imager (ESI; Sheinis et al. 2002) on the W. M. Keck-II telescope for a total integration time of 4900s (2×1800s + 1300s) on 21 July, 2001. The seeing was $0\farcs6$ and the $1\farcs25 \times 20''$ slit was oriented North-South to include the BCG, radial arc, and tangential arc (Figure 1). The spectroscopic goals were two-fold: a determination of the redshift of the arcs and a measurement of the internal kinematics of the central galaxy. An IRAF package was developed for the specific task of removing echelle distortions while preserving the 2-D shape of the spectrum essential for the latter goal (EASI2D, Sand et al. 2004). The instrumental resolution of ESI was measured from unblended sky lines to be 30±7 km s^{-1}.

The velocity dispersion profile of the BCG (Figure 2) was measured using spectral templates based on several G-K giants observed with a $0\farcs3$ slit. These were smoothed to match the instrumental resolution of the $1\farcs25$ slit and redshifted to that of the BCG (z=0.313). Analysis was restricted to a region around the G band by virtue of the high signal/noise and minimal effect of sky line residuals, using the Gauss-Hermite pixel-fitting software (van der Marel, 1994). The error bars shown in Figure 2 represent a combination of uncertainties arising from Poisson noise and systematics, the latter determined from the scatter observed using different templates and continuum fits.

The high spectral resolution of ESI proved crucial in clinching the redshifts of the arcs, as the emission lines are located in a crowded region of OH sky background. The two top panels in Figure 2.2 show the relevant portion of the ESI spectra for the tangential and radial arcs, with the observed emission lines identified as the [OII] doublet at $z = 1.501$ and $z = 1.502$ respectively. The [OII] doublet is clearly resolved for the tangential arc and it is reasonable to suppose that the missing component for the radial arc is obscured by sky emission. No other lines are detected on either spectra, down to the blue cutoff of ESI at $\sim$ 3900Å. This makes it unlikely that the single line observed for the radial arc is any of the common lines such as Hα, Hβ, [OIII]4959, 5007, CIV1549, HeII1640, or C[III]1909 because bluer lines would be detected assuming typical flux ratios. The identification of the line with Lyα at $z = 6.66$ is also unlikely given that the arc is detected in the HST F702W image (Figure 2.1). Detailed modeling of MS2137-23 based on the image configurations predicted that the sources for the arcs would be at nearly the same redshift (M93, H97).

2.2.2 Hubble Space Telescope Imaging

HST WFPC2 images of MS2137-23 (GO 5402, PI: Gioia), comprising 10 F702W exposures with a total integration time of 22.2ks, were used to measure the surface photometry of the BCG and to locate arc positions. The exposures were reduced in a standard way, using the IRAF package DRIZZLE (Fruchter & Hook, 2002).

The circularized surface brightness profile (in agreement with H97) was obtained using the IRAF task ELLIPSE and a fit performed as described in Treu et al. (2001), taking into account the HST point-spread function. The best fitting $R^{1/4}$ parameters are summarized in Table 1. To convert from F702W magnitudes to V magnitudes a k-color correction was calculated using the same method as Treu et al. (1999). Rest frame photometric quantities were corrected for Galactic extinction using A_{F702W} = 2.435E(B-V)=0.122 (Schlegel et al., 1998).

2.3 Luminous and Dark Matter Distribution

We now combine the observed spectroscopic and photometric data to constrain the matter distribution in the central region of MS2137-23. First we introduce a simple two-component spherical mass model comprising the stellar mass of the BCG and a DM halo (Sec. 3.1). We then constrain the free parameters of the model using the position of the critical lines (3.2) and the velocity dispersion profile (3.3).

2.3.1 Mass Model

For the luminous component we used a Jaffe (1983)

$$\rho_L(r) = \frac{M_L r_J}{4\pi r^2 (r_J + r)^2} \tag{2.1}$$

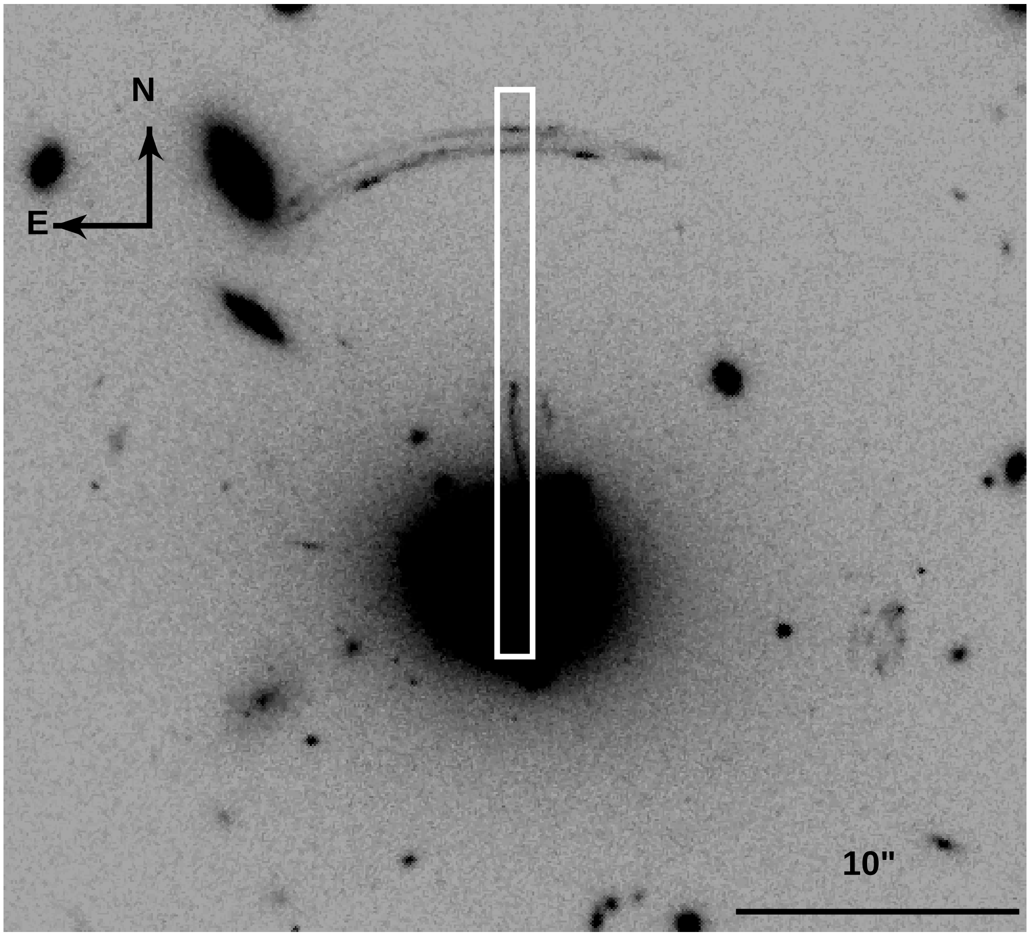

Figure 2.1: HST F702W image of MS2137-23. The rectangular box shows the dimensions ($1\overset{\prime\prime}{.}25 \times 20^{\prime\prime}$) and position of the ESI slit used to make the observations. The BCG, the radial and tangential arc are clearly visible at the bottom, center, and upper end of the slit.

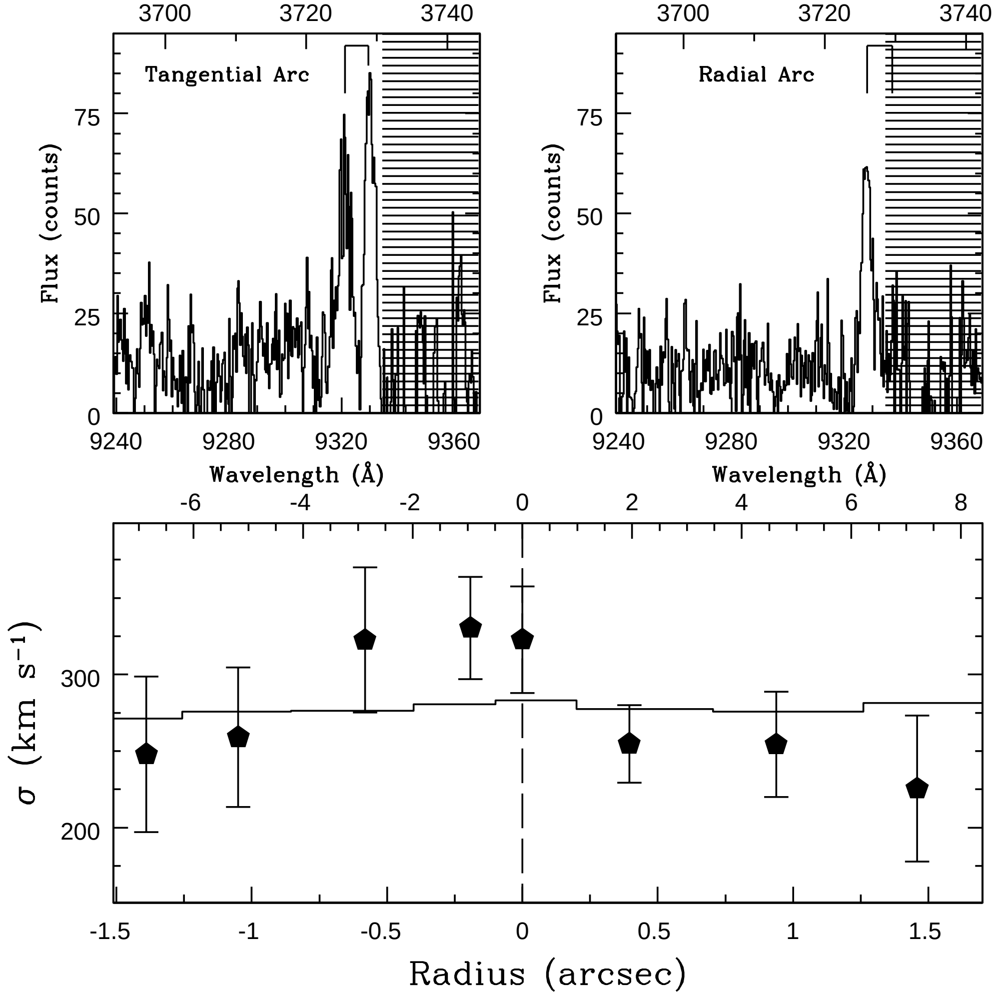

Figure 2.2: Spectroscopic results: (Top) Strong emission lines detected in the spectra of the tangential and radial arcs. These are identified as [OII]3726,3729 at $z = 1.501$ and $z = 1.502$ respectively (marked). It is argued that the missing 3729$\mathring{A}$ line in the radial arc is obscured by sky emission. (Bottom) Stellar velocity dispersion profile of the brightest cluster galaxy (points with error bars). The superimposed histogram shows the profile of the best fitting Jaffe + generalized NFW mass model (see Sec. 3 for details), taking into account the effects of seeing (0.″6), slit width, and radial binning.

mass density profile of total mass M_L, which reproduces well[1] the observed surface brightness profile (with $R_e = 0.76 r_J$). The DM halo is modeled as,

$$\rho_d(r) = \frac{\rho_c \delta_c}{(r/r_{sc})^{\beta}(1+(r/r_{sc}))^{3-\beta}} \tag{2.2}$$

representing a generalization of the CDM-motivated halos, with an inner slope β (NFW and M98 correspond to $\beta = 1, 1.5$ respectively; ρ_c is the critical density). We assume that the BCG lies at the center of the overall potential.

For a given stellar mass-to-light ratio M_*/L_V, both M_L and r_J can be deduced from the surface photometry leaving 4 free parameters in our mass model: 1) M_*/L_V; 2) the inner slope of the DM profile β; 3) the DM density scale δ_c; and 4) the DM scale radius r_{sc}.

2.3.2 Gravitational Lensing

Given our two-component spherical model, we adopted a simple lensing analysis using only the positions and redshifts of the radial and tangential arcs (Bartelmann, 1996).

The locations of the radial and tangential arcs can be estimated by calculating the position of the corresponding radial and tangential critical curves of the projected mass distribution. The Jacobian matrix of the lens mapping has two eigenvalues, $\lambda_r = 1 - \frac{d}{dx}\frac{m}{x}$ and $\lambda_t = 1 - \frac{m}{x^2}$, where $x = R/r_{sc}$ and m is a dimensionless function proportional to the mass inside projected dimensionless radius x (see, e. g., Bartelmann 1996; Schneider et al. 1992). Tangential and radial critical curves occur when $\lambda_t = 0$ and $\lambda_r = 0$, respectively. In practice, the position of the tangential arc constrains the *total enclosed mass*, while the position of the radial arc constrains its *derivative*. A proper account of ellipticity is essential for detailed lens modeling where the shape, magnification, and morphology of multiple lensed images is being reproduced. ME95, however, considered several different simple

---

[1] As a check of the results, we also considered a Hernquist (1990) luminous mass distribution. The results on β (see below) are virtually unchanged, while slightly larger values of M/L for the stellar component are obtained.

mass models where only the position of the radial and tangential critical lines were being measured and found that the position of the two was affected very little by the introduction of ellipticity. Therefore, we conclude that a spherical model is appropriate for our analysis.

For every set of free parameters $\{M_*/L_V,\ \beta,\ \delta_c,\ r_{sc}\ \}$, we can compute the predicted position of the arcs, find the likelihood assuming gaussian distributions, and constrain the acceptable mass models. The largest radius at which the mass is probed is that corresponding to the location of the tangential arc (75.8 kpc). Now r_{sc} is expected to be much greater than 100 kpc in CDM clusters (Bullock et al., 2001). In this case, the location of the critical lines depends only marginally on r_{sc} and the combined luminous and dark density profile has only 3 free parameters (we fix $r_{sc} = 400$ kpc in the following). Figure 3 shows the likelihood contours (68%, 95%, and 99%) in β vs. M_*/L_V space, obtained using the likelihood ratio statistic after marginalization with respect to δ_c. Note that with lensing alone we can rule out with greater than 95% confidence a M98 DM density profile (β=1.5).

2.3.3 Lensing + Dynamics

The full power of our analysis is only realized when we combine the earlier constraints with those made by measuring the spatially-resolved stellar velocity dispersion profile of the BCG. Given our two-component mass model (Section 3.1), we solved the spherical Jeans equation (e.g. Binney & Tremaine 1987) assuming an isotropic velocity ellipsoid for the luminous component.[2]

The assumption of isotropy in the region probed (within 30 % of R_e) is justified both on theoretical and observational grounds. Numerical simulations (e. g. van Albada 1982) and observations (e.g. Gerhard et al. 2001; Koopmans & Treu 2002) appear to rule out significant tangential anisotropy and permit some radial anisotropy only at large radii. Strong radial anisotropy in the very central

---

[2] Spherical dynamical models have been shown to reproduce accurately the kinematics of slightly elongated galaxies like the BCG (e.g. Kronawitter et al. 2000).

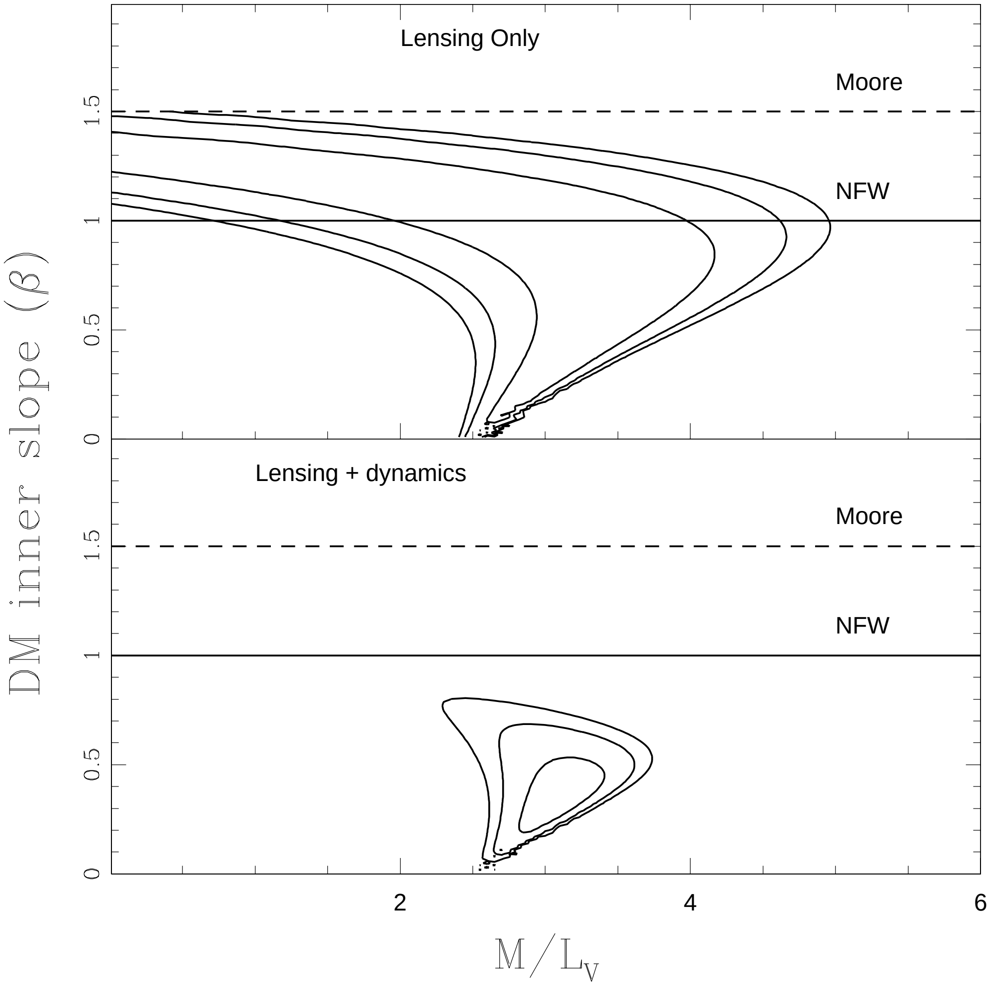

Figure 2.3: Likelihood contours (68%, 95%, and 99%) obtained for the mass modeling of MS2137-23 with a Jaffe luminous distribution plus a generalized NFW DM distribution. (Top): Contours obtained from the position of the radial and tangential arcs alone. Note that a M98 ($\beta = 1.5$) profile is excluded at the 95% level. (Bottom): Contours obtained including the measured velocity dispersion profile. Note the improved constraints on the mass parameters and that NFW profiles are clearly ruled out at the 99% level.

regions can also be ruled out based on the grounds of stability (e. g. Merritt & Aguilar 1985; Stiavelli & Sparke 1991) and consistency requirements (Ciotti, 1999). However, as a check, we ran Osipkov-Merritt (Merritt, 1985b,a) models with the anisotropy radius set equal to progressively lower radii. Moving the anisotropy radius towards zero pushes the likelihood contours towards lower values of β.

For each set of parameters in the lens model, we computed the likelihood given the velocity dispersion profile, taking into account the effects of seeing, radial binning, and finite slit width. The total likelihood was computed by multiplying the velocity dispersion likelihood by the likelihood obtained with the lensing analysis. The bottom panel in Figure 3 shows the final results of the combined analysis. With 99% confidence, M_*/L_V lies between 2.3 and 3.7 (broadly consistent with local values after passive evolution), with the inner DM slope (β) lying between 0.05 and 0.8, flatter than that expected from CDM simulations. The best-fitting parameters are $M_*/L_V = 3.1$, $\beta = 0.35$, and $\delta_c = 24000$.

To check our results, we changed R_e by 10% with a negligible effect on the likelihood contours. Similarly, the contours are virtually unchanged by offsets of $0\farcs5$ in the position of the tangential arc and by changing the seeing by 30%. Changing the position of the radial critical line by $\pm0\farcs5$ shifts the likelihood contours by ±0.1 in the β direction.

Systematic offsets of the velocity dispersion profile due to template mismatch and poor continuum fitting introduces correlation between the kinematic points that are not considered in the likelihood ratio analysis. To investigate this, we have repeated the analysis with the velocity dispersion profile shifted by the estimated systematic error (~ 15 km s^{-1}). A lower overall velocity dispersion profiles shifts our likelihood contours towards lower β ($\beta < 0.65$ 99 % CL) and viceversa ($\beta < 0.9$ 99 %CL). Our hard 99% CL upper limit is $\beta < 0.9$.

2.4 Summary and Discussion

We have secured spectroscopic redshifts for the radial and tangential arcs in the cluster MS 2137-23 and determined the velocity dispersion profile of the BCG to a physical radius of $\simeq$8 kpc. We have combined these measurements with the lensing geometry in order to construct a self-consistent model of the mass distribution in the cluster core. Using a spherically symmetric luminous and DM mass distribution, we rule out the presence of a DM halo with an inner slope $\beta > 0.9$ at greater than 99% confidence, including systematics. M98 and NFW-type halos with $\beta \geq 1.0$ are inconsistent with the mass distribution in the core of MS2137-23.

Since the infall of baryons associated with the BCG are likely to *steepen* the DM halo (Blumenthal et al., 1986; Mao et al., 1998), our measured profile may imply the original DM profile was even flatter. A full modeling of this process is beyond the scope of this letter, but this strengthens our conclusion that the inner regions of the DM halo of MS2137-23 cannot be described by CDM-motivated universal halos. A potential concern is that our models have only two mass components, but X-ray emitting gas could be a non-negligible third massive component. Using ROSAT observations of MS2137-23 (Ettori & Fabian, 1999) we estimate that removing the X-ray component will steepen the resulting DM halo slope by less than $\simeq 0.1$ and therefore does not change the result dramatically.

Finally, individual halo shapes can depart from the ensemble average behavior. Therefore it is necessary to apply such a test to a sample of clusters. Our simple method is applicable to all approximately round clusters with a massive galaxy at their center, provided that they have at least a giant tangential arc (radial arcs further enhance the sensitivity but are not required). We are in the process of collecting data for a dozen clusters with the aim of performing such a statistical test.

We are grateful to A. Benson, J.-P. Kneib, and L. Koopmans for insightful discussions and comments on this project, and to P. Shopbell for numerous computer tips. We acknowledge the use of the Gauss-Hermite Pixel Fitting Software developed by R. P. van der Marel. We acknowledge financial support for proposal number HST-AR-09527 provided by NASA through a grant from STScI, which is operated by AURA, under NASA contract NAS5-26555. Finally, the authors wish to recognize and acknowledge the cultural role and reverence that the summit of Mauna Kea has always had within the indigenous Hawaiian community. We are most fortunate to have the opportunity to conduct observations from this mountain.

Table 2.1: Relevant spectro-photometric quantities

Redshift (BCG)	0.313 ± 0.001
Radial critical line	$4''.5 \pm 0''.3$
Tangential critical line	$15''.35 \pm 0''.20$
(1-b/a)$_e$	0.17 ± 0.01
F702W (mag)	16.48 ± 0.07
SB$_{e,F702W}$ (mag/arcsec^2)	23.58 ± 0.34
R$_{e,F702W}$	$5''.02 \pm 0''.50$
M$_V$ (mag)	-24.38 ± 0.09
SB$_{e,V}$ (mag/arcsec^2)	22.76 ± 0.34
R$_{e,V}$ (kpc)	24.80 ± 1.68

Chapter 3

The Dark Matter Distribution in the Central Regions of Galaxy Clusters: Implications for CDM

David J. Sand[a], Tommaso Treu, Graham P. Smith & Richard S. Ellis

California Institute of Technology, Astronomy, mailcode 105–24, Pasadena, CA 91125

Abstract

We have undertaken a spectroscopic survey of gravitational arcs in a carefully chosen sample of six clusters, each containing a dominant brightest cluster galaxy. These systems are used to study the relative distributions of dark and baryonic material in the central regions. Three clusters present both radial and tangential arcs and provide particularly strong constraints on the mass profiles, whereas the other three display only tangential arcs and act as a control set. Following Sand et al. (2002), we analyze stellar velocity dispersion data for the brightest cluster galaxies in conjunction with the arc redshifts and lens models to constrain the dark and baryonic mass profiles jointly. For the systems containing radial arcs, we find that the inner dark matter density profile is consistent with a 3-D distribution, $\rho_{DM} \propto r^{-\beta}$, with logarithmic slope $\langle\beta\rangle = 0.52^{+0.05}_{-0.05}$ (68% CL). Similarly, we find

---

[*] This chapter has been published previously as Sand et al. (2004)

that the tangential arc sample gives an upper limit, β <0.57 (99% CL). Taking the 6 clusters together, the mean dark matter distribution is inconsistent with the standard Navarro et al. (1997) value, β=1.0, at >99 % confidence. In addition, we find considerable cosmic scatter in the β ($\Delta\beta$ ~0.3) values of the radial arc sample. We find no evidence that systems with radial arcs preferentially yield flatter dark matter profiles as might be expected if they were a biased subset. We discuss the validity of our 1-D mass reconstruction method and verify its conclusions by comparing with results of a more rigorous ray-tracing code that does not assume axial symmetry. Our results extend and considerably strengthen the earlier conclusions presented by Sand et al. (2002) and suggest the relationship between dark and visible matter in the cores of clusters is much more complex than anticipated from recent simulations.

3.1 Introduction

The Cold Dark Matter (CDM) paradigm has been extremely successful in explaining observations of the universe on large scales at various epochs, from that of the cosmic microwave background through high redshift studies of the $Ly\alpha$ forest to the distribution of galaxies and clusters in local surveys (e.g. Percival et al. 2001; Spergel et al. 2003; Croft et al. 2002; Bahcall et al. 2003). A primary tool for making the necessary predictions is that of N-body simulations, which are now able to resolve structures on highly non-linear scales so that the properties of dark matter (DM) halos can be predicted on ~kpc scales.

A central prediction arising from CDM simulations is that the density profile of DM halos is universal in form across a wide range of mass scales, from dwarf galaxies to clusters of galaxies (e.g. Navarro et al. 1997; hereafter NFW97). Within a scale radius, r_{sc}, the DM density aymptotes to $\rho \propto r^{-\beta}$ while external to r_{sc}, $\rho \propto r^{-3}$. The value of the logarithmic inner slope, β, is still a matter of debate. However, in nearly all studies, β ranges between 1 (NFW97) and 1.5 (Moore et al. 1998; Ghigna et al. 2000; hereafter referred to as the "Moore" slope for convenience). Recent work by Power et al. (2003) and Fukushige & Makino (2003) has suggested that with proper account of the timestep, force accuracy and particle number, the inner slope does not converge to a power law, as predicted from lower resolution simulations, but instead becomes progressively shallow at smaller radii. Power et al. found β=1.2 at their innermost reliable location. Further work in this area will allow for even more precise predictions of the form of DM halos.

An observational verification of the NFW97 (or Moore) form, via a convincing measurement of β and its scatter over various mass scales, has proved controversial despite the motivation that it offers a powerful test of the CDM paradigm. A major observational hurdle is the importance of convincingly separating the baryonic and non-baryonic components. Indeed, observations may guide the interpretation of the numerical simulations, both because the inclusion of baryons into simulations is difficult (e.g. Frenk 2002) and because it is expensive computationally to simulate a sufficient number of halos (with proper convergence) to characterize the expected scatter in halo shapes.

Most of the observational effort has been directed via dynamical studies of low surface brightness and dwarf galaxies, as these are thought to be DM dominated at all radii. However, analyses of the various datasets have given conflicting values of β and many of the assumptions used have been questioned (see discussion by Simon et al. 2003 and Swaters et al. 2003). Some studies have provided evidence for cores of roughly constant density (e.g. de Blok et al. 2001; de Blok & Bosma 2002; Simon et al. 2003) whereas others find their data are consistent with β=1 (e.g. van den Bosch & Swaters 2001; Swaters et al. 2003). Steep inner profiles with $\beta \approx$1.5 seem to be ruled out.

In order to test the simulations convincingly, observations should not be confined to mass scales probed by dwarf galaxies. Accordingly, several attempts have been made to constrain the DM profiles of more massive systems. Observations of spiral and early-type galaxies tend to favor inner slopes that are shallower than predicted by CDM simulations (Treu & Koopmans, 2002; Koopmans & Treu, 2003; Borriello & Salucci, 2001; Borriello et al., 2003; Jimenez et al., 2003), although the dominance of stellar mass at small scales makes it difficult to achieve an accurate measurement of the dark halo component.

More effort has been devoted to galaxy cluster mass scales. Most common has been the use of X-ray observations of the hot intracluster medium under the assumption of hydrostatic equilibrium. Whether hydrostatic equilibrium is maintained in the inner regions, where there are often irregularities and "cooling flows", remains an important question (see Arabadjis et al. 2002). Within the context of the hydrostatic equilibrium assumption, many studies have considered only a limited range of DM profiles, comparing, for example, NFW (or Moore) fits with those of a non-singular isothermal sphere (e.g. Schmidt et al. 2001; Allen et al. 2002; Pratt & Arnaud 2002). In general, X-ray analyses have led to wide ranging results, with β ranging from $\simeq$0.6 (Ettori et al., 2002) through $\simeq$1.2 (Lewis et al., 2003) to $\simeq$1.9 (Arabadjis et al., 2002). However, when using X-ray data alone, it is difficult to account for the stellar mass of a central brightest cluster galaxy (BCG), which leads to complications in interpreting the shape of the DM density profile at small radii (Lewis et al., 2003). In fact, although the stellar component is small in terms of the total mass of the system, it can dominate the mass density at small radii and mimic a cuspy DM halo if it is not taken into proper account.

Gravitational lensing offers a particularly promising probe of the total mass profile. Projected mass maps of the inner regions of clusters constrained by strongly lensed features of known redshift have been compared with CDM predictions (Tyson et al. 1998; Smith et al. 2001; hereafter S01). By using weak lensing and stacking a sample of clusters, Dahle et al. (2003) found an inner DM slope roughly in agreement with CDM predictions (albeit with large uncertainties). Recently, a combined strong and weak lensing analysis of Cl0024 has confirmed the prediction of CDM numerical simulations that the DM density profile falls off like $\rho \propto r^{-3}$ at large radii, strongly ruling out a density profile that falls off like an isothermal mass distribution (Kneib et al., 2003). A combined strong and weak lensing analysis has also been used to constrain the inner DM slope in the cluster MS2137-23 (Gavazzi et al. 2003; hereafter G03), although the precise value of the slope depends on the assumed stellar mass-to-light ratio of the BCG.

As with the X-ray studies, gravitational lensing alone is unable to separate the baryonic (luminous) and non-baryonic (dark) components. Given the observational evidence that BCGs often lie at the bottom of the cluster potential in regular, non-interacting systems (e.g. S01, G03, Jones et al. 1979), the dynamics of the stellar component offers a valuable route to resolving this problem. In practice, the stellar kinematics of the BCG provides an additional measure of the total mass at small radii. In work by Dressler (1979), the velocity dispersion profile of the BCG in Abell 2029 was found to rise significantly at large radii and this was taken as evidence that the cluster DM halo was being probed. More recently, Kelson et al. (2002) have measured an extended velocity dispersion profile in the BCG in Abell 2199, for which they concluded that the best-fitting DM density profile for the cluster was shallower than NFW. Miralda-Escude (1995) first suggested that a combination of lensing and stellar velocity dispersion measurements could separate the luminous and dark components in the inner regions of clusters (see also Natarajan & Kneib 1996 for a lensing + dynamics analysis of Abell 2218). This article highlighted the system MS2137-23 which, at the time, was unique in containing both radial and tangential gravitational arcs.

In an earlier paper (Sand et al. 2002; hereafter STE02) we combined a simple axisymmetric lensing model of MS2137-23 with stellar velocity dispersion measurements of the BCG to place strong constraints on the inner slope of the DM density profile. The resulting β value was markedly inconsistent with $\beta \geq 1$ and we demonstrated carefully how the combination of lensing and dynamics offers superior constraints to those provided by either method alone.

The goal of this paper is to extend the results of STE02 to a larger sample of six galaxy clusters. In addition to MS2137-23, we consider two additional systems containing both radial and tangential gravitational arcs. The three other clusters contain only a tangential arc and analysis of this subsample offers a valuable control from which we expect to deduce whether selecting the rarer systems with radial arcs might bias our conclusions towards flatter inner slopes. As a further test on the robustness of our results, we check our lensing model by dropping the assumption of radial symmetry.

A plan of the paper follows. In §2 we discuss how the sample of clusters was chosen. In §3 we discuss the archival Hubble Space Telescope and additional infrared imaging observations and how we derived the location of the critical lines and the surface photometry of the BCGs. In §4 we present spectroscopic measurements made with the Keck telescope which delivered the redshifts of the gravitational arcs and the stellar velocity dispersion profile of the BCGs. We discuss our analysis of the DM density profiles in the context of the assumed mass model for both the radial+tangential and tangential-only arc subsamples in §5. In §6 we present a thorough discussion of possible systematic uncertainties associated with our method. In §7 and §8 we discuss and summarize our results, respectively.

Throughout this paper, we adopt r as the radial coordinate in 3-D space and R as the radial coordinate in 2-D projected space. We assume H_0=65 km $s^{-1}Mpc^{-1}$, $\Omega_m = 0.3$, and Ω_Λ=0.7.

3.2 Sample Selection

The aim of this project is to combine constraints from the velocity dispersion profile of a BCG with those from gravitational lensing to measure the slope of the inner DM density profile in galaxy clusters, as described in STE02. Two important simplifying assumptions inherent to our method are that the BCG lies at the bottom of the cluster potential and that the BCG is a purely pressure supported system, whose dynamics can be described by the Jeans equation. For this reason, a suitable galaxy cluster for this project must have a dominant, relatively isolated central galaxy (coincident with the cluster's center of mass) with nearby strong lensing features and no indications of significant substructure or a significantly elongated potential. Radial gravitational arcs – albeit uncommon – are particularly valuable since they constrain directly the derivative of the total enclosed mass (e.g. STE02).

In order to find a sample of suitable targets, we undertook an exhaustive search of the Hubble Space Telescope (HST) Wide Field and Planetary Camera 2 (WFPC2) archive for radial gravitational arcs in galaxy clusters. In summary, all galaxy cluster pointings in the redshift range $0.1 < z < 1.0$ were retrieved from the HST archive, amounting to ∼150 different clusters in all. This is the first search of its kind and has yielded ∼15 candidate radial arc systems. Dozens of smaller lensed features have been uncovered as well, due to the high angular resolution of HST.

We performed spectroscopic follow-up at the Keck Telescope of many candidate lensing systems, with emphasis on systems with both radial and tangential arcs. Spectroscopic confirmation is particularly important for radial arc candidates. In fact, since radial arcs normally occur in the very inner regions of galaxy clusters, they can easily be confused with optical filaments associated with cluster cooling flows. Indeed, several radial features proved to be contaminant optical filaments at the cluster redshift. A description of the search, the complete catalog, and spectroscopic identifications will be described in a follow-up paper (Sand et al. 2004, in preparation).

In this paper we focus on a sample of six spectroscopically confirmed lensing clusters, for which we have also obtained a stellar velocity dispersion profile of the BCG (Table 1). The sample includes three galaxy clusters with radial and tangential arcs and three clusters with just tangential arcs, one of which does not have HST imaging (MACS 1206; Ebeling et al. 2004, in preparation).

3.3 Imaging Data and Analysis

This section describes the two measurements that are to be made from the imaging data to determine the cluster mass distribution: the surface brightness profile of the BCG and the positions of the lensing critical lines as inferred from the location of symmetry breaks in the giant arcs. In addition, two of the six BCGs in our sample (RXJ 1133 and Abell 383) have obvious dust lanes. K-band images of the cluster centers were used to correct for the dust lanes and obtain the unreddened surface brightness profile of the BCG as described in §3.2. Table 1 is an observation log of all the optical/NIR observations.

Table 3.1: Optical/NIR Imaging Log

Cluster	z_{clus}	Date	Telescope/ Instrument	Filter	Exposure time (ks)
MS2137-23	0.313	May 28-31,1995	HST/WFPC2	F702W	22.2
Abell 383	0.189	Jan 25, 2000	HST/WFPC2	F702W	7.5
		Dec 17, 2002	Keck/NIRC	K_s	1.0
Abell 963	0.206	May 7, 2000	HST/WFPC2	F702W	7.8
RXJ 1133	0.394^a	Feb 20, 2001	HST/WFPC2	F606W	1.0
		Dec 17, 2002	Keck/NIRC	K_s	0.8
MACS 1206	0.440^a	April 13, 2002	Keck/ESI	I	0.3
Abell 1201	0.169	April 7, 2001	HST/WFPC2	F606W	0.8

Imaging Observation Log of the clusters in our sample. [a]New spectroscopic measurement

3.3.1 Optical Data

Archival HST imaging is available for five of the six clusters. A gunn I-band image in good seeing conditions ($0\farcs7$ FWHM) was obtained for the final cluster, MACS1206, using the Echelle Spectrograph and Imager (ESI; Sheinis et al. 2002) at the Keck-II Telescope. Figure 1 shows the inner regions of the six clusters and their accompanying gravitational arcs. Superimposed on the images are the spectroscopic slit positions that will be described in §4.

Because our sample results from an extensive HST archive search, no specific observing strategy is common to all clusters. The HST observing strategies fall into two categories: 1) multiple-orbit observations separated by integer pixel dithers (MS 2137-23, Abell 383, and Abell 963) and 2) single orbit SNAP obser-

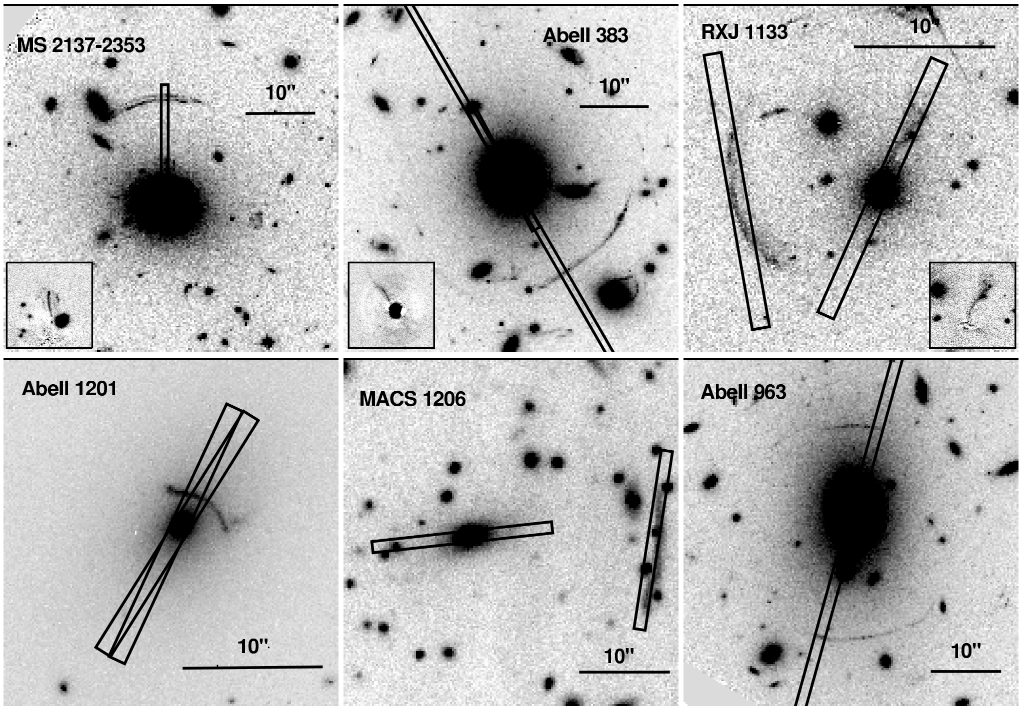

Figure 3.1: Images of the six clusters in this study. The top row features the clusters with both radial and tangential arcs. The postage stamp insets show zoomed in BCG subtracted images so that the radial arcs can be clearly seen. The bottom row contains those clusters with tangential arcs only. The overlaid "slits" correspond to the actual slit positions and sizes that were observed. See Table 3.4 for the spectroscopic observation log. North is up and East is to the left in all images.

vations comprising two CR-SPLIT, undithered exposures (Abell 1201, RXJ 1133). Accordingly, two different data reduction procedures were employed.

The clusters with dithered exposures were pipeline processed with the DITHER package (Fruchter & Hook, 2002) in IRAF to remove cosmic rays, correct for the undersampling of the point spread function, and to shift and combine the frames. The effective resolution for the images (F606W and F702W) was $\sim 0\farcs15$. The undithered targets were processed by first applying the IRAF task WARMPIX using the table data supplied by the WFPC2 website for the dates of the observations. The images were then combined with the task CRREJ to remove cosmic ray hits. A small number of residual cosmic rays were removed with the IRAF task LACOSMIC (van Dokkum, 2001).

The single, gunn I band exposure of MACS 1206 was reduced in a standard way with cosmic ray removal being performed by the IRAF task LACOSMIC (van Dokkum, 2001). Photometric calibration, good to 0.03 mag, was obtained from two photometric standard star fields (Landolt, 1992).

Table 3.2: BCG Photometric Properties

Cluster	Filter	R_e (arcsec/kpc)	M (mag)	SB_e (mag arcsec^{-2})	K-color Correction	$(1-b/a)_e$
MACS 1206	gunn I	2.08 ± 0.17	17.48 ± 0.07	22.46 ± 0.23	0.81 ± 0.03	0.35 ± 0.05
	V	12.75 ± 1.04	-23.93 ± 0.08	21.57 ± 0.23		
MS 2137-23	F702W	5.02 ± 0.50	16.48 ± 0.07	23.58 ± 0.34	0.49 ± 0.03	0.17 ± 0.01
	V	24.80 ± 1.68	-24.38 ± 0.09	22.76 ± 0.34		
RXJ 1133	F606W	5.18 ± 0.12	18.00 ± 0.06	24.96 ± 0.33	0.41 ± 0.03	0.18 ± 0.05
	B	29.73 ± 0.69	-23.44 ± 0.07	23.89 ± 0.33		
Abell 383	F702W	13.75 ± 0.60	14.67 ± 0.06	22.95 ± 0.25	0.60 ± 0.04	0.19 ± 0.03
	V	46.75 ± 2.04	-24.78 ± 0.07	22.72 ± 0.25		
Abell 1201	F606W	15.01 ± 0.10	15.44 ± 0.08	24.81 ± 0.21	0.10 ± 0.05	0.32 ± 0.02
	V	46.68 ± 0.31	-24.23 ± 0.09	24.18 ± 0.21		
Abell 963	F702W	11.04 ± 0.14	15.08 ± 0.05	23.67 ± 0.27	0.59 ± 0.03	0.36 ± 0.02

continued on next page

Table 3.2 – continued from previous page

Cluster	Filter	R_e (arcsec/kpc)	M (mag)	SB_e (mag arcsec^{-2})	K-color Correction	$(1-b/a)_e$
	V	40.19 ± 0.51	-24.38 ± 0.06	23.39 ± 0.27		

Photometric properties derived from our 2D surface brightness profile fitting. The first line for each cluster is in the observed filter while the second is in a rest filter. The K-color correction and ellipticity at the effective radius are listed as well.

3.3.2 Near–Infrared Data

Dust features in BCGs are common (see e.g. Laine et al. 2003), but hinder attempts at measuring structural parameters. To correct for internal dust extinction in Abell 383 and RXJ 1133, we observed the two BCGs with NIRC on the Keck I Telescope in the K_s band (see Table 1). The data were reduced in a standard manner using IRAF tasks to dark subtract, linearize, flat–field, align and combine the individual frames. The flat–fields were created from a rolling median of the adjacent science frames. The point–spread–function of both final reduced frames has FWHM $\simeq 0.6''$.

A dust correction is obtained as described in Treu et al. (2001) and Koopmans & Treu (2003). Briefly, we first assume that dust has a neglible effect at large radii and that any intrinsic BCG color gradient is small. Then we smooth the HST image to the resolution of the K-band image and compute an extinction map in the observer frame:

$$E_{HST,K}(x,y) = \mu_{HST}(x,y) - \mu_K(x,y) - \mu_{HST,K}(\infty) \qquad (3.1)$$

where $\mu_{HST}(x,y)$ and $\mu_K(x,y)$ are the surface brightness in a given pixel and $\mu_{HST,K}(\infty)$ is the color at large BCG radii. Adopting the Galactic extinction law of Cardelli et al. (1989) we find the following relations between the absorption coefficients in the individual bands and the color excess (Equation 1). For Abell 383, $A_{F702W} = 1.199 E_{F702W,K}$ and $A_K = 0.199 E_{F702W,K}$. For RXJ1133, $A_{F606W} = 1.164 E_{F606W,K}$ and $A_K = 0.164 E_{F606W,K}$.

The correction removes any visible trace of the dust lane. However, it reveals that the BCG in Abell 383 has a very close, compact companion. For the purpose of surface photometry analysis, the close companion is easily dealt with by fitting it simultaneously to the BCG. The companion is $\sim 0\farcs7$ from the center of the BCG and is $\sim$5.5 mag fainter with $R_e \approx 0\farcs5$. The spectrum of the companion and the BCG cannot be distinguished in the ESI spectrum so no relative velocity can be measured. Assuming that the relative masses of the two galaxies is proportional to their flux ratio, the companion galaxy should not effect our later dynamical analysis.

3.3.3 Surface Brightness Fitting

Total magnitudes and effective radii ($R_{\rm e}$) were measured from our (dust corrected) optical images by fitting two dimensional $r^{1/4}$ surface brightness profiles as described in STE02 using the software developed by Treu et al. (1999, 2001). For the purpose of the fitting, $r^{1/4}$ models were convolved with artificial Point Spread Functions (PSFs). Tiny Tim PSFs were used for the HST images, while gaussian PSFs were adopted for the ground based images. Note that uncertainties in the artificial PSF have negligible impact on the determination of the effective radii which are always much larger than the PSF HWHM (c.f. Treu et al. 2001. Figure 2 shows the measured surface brightness profile along with the best fitting $r^{1/4}$ fit (PSF convolved).

Observed magnitudes were corrected for galactic extinction using the $E(B-V)$ values and extinction coefficients calculated by Schlegel et al. (1998). Finally, observed magnitudes were transformed to rest frame absolute magnitudes through the standard filter that best matches the observed bandpass through a K-color correction as in STE02 and Treu et al. (1999, 2001). Typical error estimates on the transformation are of order 0.05 mag. All BCG photometric results (both rest and observed frame) are listed in Table 2.

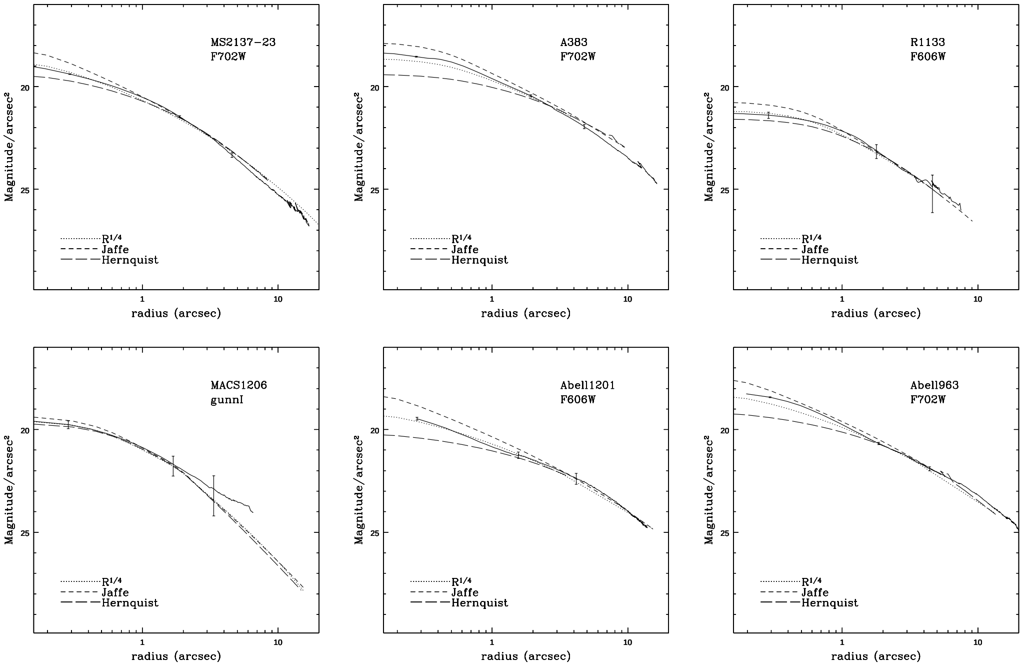

Figure 3.2: Surface brightness profile of the BCGs. The solid lines are the measured surface brightness profiles while the other curves are various parameterizations of the data based on a $r^{1/4}$ fit, convolved with the PSF of the observation. The uncertainty of the profile is given at several representative points. As can be seen, the Jaffe and Hernquist profile generally bracket the best-fitting $r^{1/4}$ at low radii. See §6.3 for a discussion of the effects our chosen luminous mass component parameterization has on our results.

3.3.4 Critical line determination

Crucial to the simple lensing method that we describe in § 4.4.1 is the location of the lensing critical line (either radial or tangential). Formally, the critical lines of a lens model are those regions where the magnification of the images diverge, although this does not occur in practice due to the extended size of the source. In addition to being strongly magnified, objects near the radial critical line will be distorted strongly in the direction radial to contours of constant density, while objects near the tangential critical line will be distorted tangentially. Typically, giant bright arcs are the result of multiple highly magnified merging images. Two merging images with opposite parity often bracket a critical line.

In this work, the critical line position was chosen by visual inspection, either in between two merging images or near strongly distorted arcs. No prior lensing analysis was performed, although for those systems that have published lens models this extra information was taken into account. The critical line positions including conservative estimates of the uncertainties are listed in Table 3.3. Note that the radial critical line uncertainties are larger due to contamination by the bright BCGs and the radial nature of these arcs. In contrast, the tangential critical line uncertainties are within a factor of ∼2-3 of the seeing disk.

3.4 Spectroscopic Data and Analysis

All spectroscopic measurements – yielding arc redshifts and/or a BCG velocity dispersion– were made with either the Low Resolution Imager and Spectrograph (LRIS) on Keck I (Oke et al., 1995) or ESI on Keck II (Sheinis et al., 2002). Table 3.4 summarizes the spectroscopic observations for each cluster.

Table 3.3: Gravitational Arc Properties

Cluster	R_{rad} (arcsec)	R_{tan} (arcsec)	z_{radial}	z_{tan}
MACS 1206	-	21.3 ± 0.4	-	1.035^a
MS 2137-23	4.5 ± 0.3	15.35 ± 0.20	1.502^b	1.501^b
RXJ 1133	3.2 ± 0.5	10.9 ± 0.3	1.544^a	1.544^a
Abell 383	1.90 ± 0.6	15.7 ± 0.4	1.010^a	1.009^a
Abell 1201	-	2.2 ± 0.3	-	0.451^c
Abell 963	-	11.9 ± 0.2	-	0.77^d

Geometric properties of the gravitational arcs and BCGs, along with the distance scale for each cluster based on the adopted cosmology. The BCG ellipticity at approximately the effective radius, R_e, and the positions of the gravitational arcs with respect to the BCG center are listed.[a]New spectroscopic measurement [b]Sand et al. 2002 [c]Edge et al. 2003 [d]Ellis et al. 1991

3.4.1 Data Reduction

The LRIS data were reduced in a standard way with bias-subtraction, flat-fielding and cosmic ray rejection. Wavelength calibration was performed using calibration arc lamps and unblended sky lines. The instrumental resolution for the 600/5000 grism (blue arm, 560 dichroic) used for the velocity dispersion measurement of Abell 963 was measured to be 175 km s^{-1} from unblended night sky lines. For the ESI observations, a set of IRAF tasks (EASI2D) were developed for the specific goal of removing echelle distortions while preserving the two-dimensional shape of the spectrum. The instrumental resolution of the reduced 2D spectra for the $1''.25 \times 20''$ slit was measured to be 32 km s $^{-1}$ from unblended night sky lines and the spatial scale ranges from 0.12 to 0.17 arcsec/pixel from the bluest to the reddest order.

EASI2D consists of the following steps: 1) Bad column interpolation, debiasing, and an initial flat-fielding are performed on the entire two dimensional spectrum.

2) The curved echelle orders are mapped using multi-hole exposures (spaced a constant 2.68 arcseconds apart (Goodrich & Radovan, private communication)) and multiple stellar exposures at prescribed positions along the slit. 3) Each order is rectified using the IRAF task TRANSFORM (conserving counts). Arc lamps and twilight sky flats are rectified along with science frames for further calibrations. 4) Sky flats are used to correct for the non-uniform sensitivity (slit function) in the spatial direction of the individual echelle orders. 5) After rectification, each exposure of each order is separated and cosmic ray cleaned using LACOSMIC. 6) After rectification, each order is separated and wavelength calibrated individually. 7) Sky subtraction is performed on each order interactively with a low order polynomial fit along the spatial direction to blank regions of the slit. Alternatively, sky subtraction can be achieved by subtracting appropriately scaled dithered science exposures from each other. This second method is preferable beyond ∼ 7000Å where sky emission lines are strongest. 8) If needed, one dimensional spectra can be extracted from the two-dimensional spectra of each order and combined on a single spectrum. This step was typically undertaken only for the kinematic template star spectra (see § 3.4.2).

Table 3.4: Spectroscopic Observation Log

Cluster	Date	Target	Instrument	Exposure time (ks)	Seeing (“)	Pos. Angle (degrees)	Slit size (“)
MS2137-23	July 21,2001	Arcs/BCG	ESI	5.9	0.6	0	1.25
Abell 383	Dec 12, 2002	Rad. Arc/BCG	ESI	5.4	0.7	28	1.25
	Oct 19, 2001	Tan. Arc	LRIS	3.8	0.7	30	1.0
RXJ 1133	Apr 11-12, 2002	BCG/Rad. Arc	ESI	12.6	0.6-0.7	-24	1.25
	Apr 11, 2002	Tan Arc	ESI	3.6	0.7	10	1.25
MACS 1206	Apr 13, 2002	BCG	ESI	9.0	0.75	98	1.25
	Apr 13, 2002	Tangential arc	ESI	3.6	0.75	273	1.25
Abell 1201	Apr 12, 2002	BCG/tan arc	ESI	3.6	0.6	-32	1.25

continued on next page

Table 3.4 – continued from previous page

Cluster	Date	Target	Instrument	Exposure time (ks)	Seeing (“)	Pos. Angle (degrees)	Slit size (“)
Abell 1201	Apr 12, 2002	BCG/tan arc	ESI	3.6	0.6	-25	1.25
Abell 963	Mar 28, 2001	BCG	LRIS	4.8	0.7	-15.5	1.5

Summary of the spectroscopic observations.

3.4.2 Redshift Measurements and Stellar Kinematics

Table 1 (BCGs), Table 3.3 (gravitational arcs), and Figure 4.3 detail all redshift measurements made. Many of these measurements were dependent on the high spectral resolution of ESI, as many emission lines were buried in the OH sky background. All arc redshift identifications are based on the detection of the [OII]3726,3729 doublet in emission. Note that for the purpose of this work we are only using the “northern” arc of Abell 963 (Ellis et al., 1991). Abell 383 has also been studied extensively by S01 (see also Smith et al. 2005), who obtained a spectroscopic redshift for the tangential arc in this cluster. We add to S01’s study by measuring spectroscopic redshifts for both the radial arc and a different portion of the tangential arc. These new data provide more stringent constraints on the gravitational potential of this cluster (§6.1).

We now describe the measurement of the line of sight velocity dispersion profile of the BCGs. The 2D spectra were summed into spatial bins corresponding approximately to the seeing during the observation, thus ensuring that each velocity dispersion measurement is approximately independent, and increasing the signal-to-noise ratio per spatial bin. In Abell 383, an entire side of the spectrum was avoided due to the interloping galaxy (§3.2) and the presence of the dust lane. Also, we avoided the side of the BCG in RXJ 1133 effected by the dust lane. Two slightly different position angles were used for Abell 1201.

Following well established procedures (Franx, 1993; van Dokkum & Franx, 1996; Treu et al., 1999, 2001; Kelson et al., 2000; Gebhardt et al., 2003; van Dokkum & Ellis, 2003), the velocity dispersion for each spatial bin is measured by comparing stellar templates (appropriately redshifted and smoothed to the instrumental resolution of the galactic spectra) broadened by Gaussian line profiles with the galactic spectrum. The fit is performed using the Gauss-Hermite Pixel Fitting Software (van der Marel, 1994) in pixel space to allow for easy masking of emission lines and regions of high night sky residuals. All velocity dispersion measurements were taken from spectral regions around the G band absorption feature. Also measured with the Gauss-Hermite Pixel Fitting Software was the relative velocity profile of each BCG. There is no evidence of rotation (within the uncertainties) in any of the BCGs. As a result, we assume in our analysis that the systems are completely pressure supported.

For each BCG, the velocity dispersion profile was measured using all of the available stellar templates with a variety of continuum fits. The stellar template that yielded the lowest χ^2 was adopted as the best fit. Table 5 contains the tabulated velocity dispersion measurements obtained. Listed uncertainties are the sum in quadrature of a random component (taken from the output of the Gauss-Hermite Pixel Fitting Software) and a systematic component due to template mismatch (the rms of the velocity dispersion obtained from all templates).

In order to measure accurate velocity dispersions, spectra with sufficient S/N are required. In general, the minimum S/N needed depends both on the instrumental resolution and the velocity dispersion to be measured. A higher S/N is needed as the velocity dispersion becomes comparable to and less than that of the instrumental resolution (e.g. Treu et al. 2001; Jorgensen et al. 1995). Since the typical central velocity dispersion of a BCG is $\sigma \sim$ 300-400 km s^{-1}(e.g. Fisher et al. 1995) compared to the 32 (175) km s^{-1} resolution of the $1\farcs25$ ($1\farcs50$) ESI (LRIS) slit, the velocity dispersion measurement should be reliable down to low S/N. In order to verify this numerically for the case of the ESI configuration, high S/N template spectra were broadened by Gaussian line profiles to known velocity dispersions (σ =50, 100, 150, 200, 250, 300, 350 km s^{-1}) and Poisson noise was added (S/N= 5, 7, 10, 12, 15, 20) for 100 different realizations. The velocity dispersion of these broadened, noisy spectra was then recovered using an area around the G band absorption feature with the Gauss Hermite Pixel Fitting software with

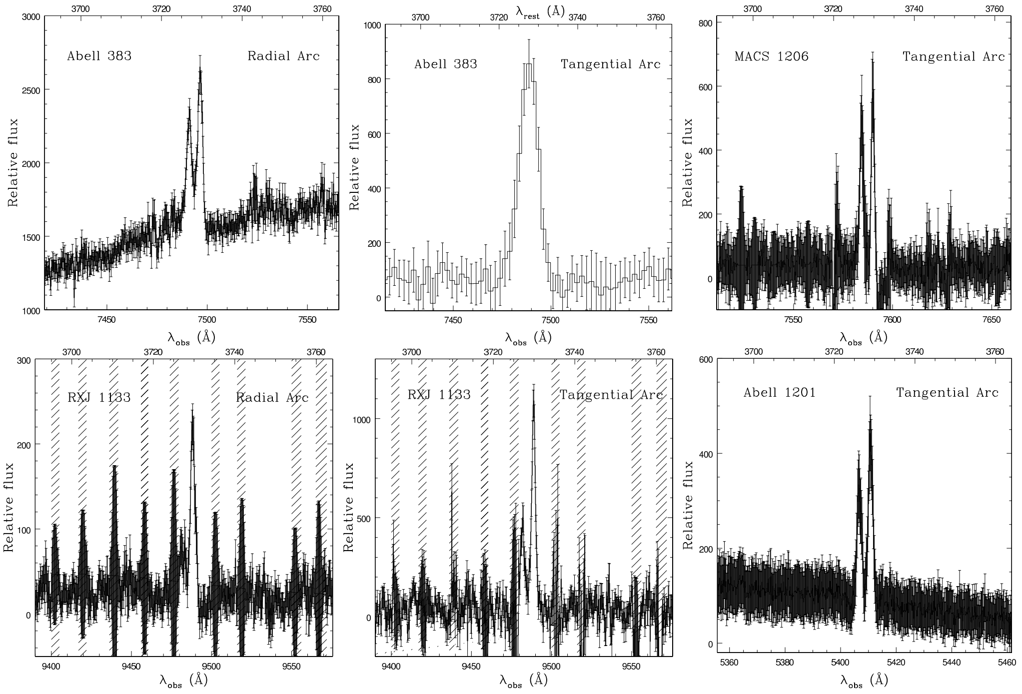

Figure 3.3: New gravitational arc redshift measurements. All new redshift measurements of gravitational arcs in this work were identified by strong [O II] in emission. Both the radial arc in Abell 383 and the tangential arc in Abell 1201 have strong continuum due to the nearby presence of the BCG. See Table 3.3 for a list of all gravitational arc redshift measurements used in this study.

both the same template (K0III) and a template with a different spectral type (G9III template used on a broadened K0III spectrum). Using the K0III template on the broadened K0III spectrum recovers the expected velocity dispersion with formal uncertainties less then 10% down to S/N of 5 (the exception being the 50 km s^{-1}measurement with S/N=5, which had an average formal uncertainty of 8 km s^{-1}). Using the G9III template on the K0III broadened spectrum did lead to systematic offsets from the input velocity dispersion of up to 6.5%, comparable to the formal uncertainty in the measurement. Thus, we will take into account possible uncertainties with regard to template mismatch in the data both in our final uncertainties and when deriving mass profiles.

Table 3.5: Velocity Dispersion Profiles

Cluster	Spatial Binning (arcsec)	σ (km s^{-1})
MACS 1206	-0.30 - 0.30	257 ± 39
	0.30 - 1.37	245 ± 50
	-0.30 - -1.37	259 ± 52
RXJ 1133	0.0 - 0.61	333 ± 30
	0.61 - 1.22	306 ± 41
	1.22 - 1.98	337 ± 67
Abell 1201	-0.35 - 0.35	231 ± 13
PA=-32	-1.06 - -0.35	257 ± 21
	0.35 - 1.06	232 ± 18
	1.06 - 1.76	224 ± 28
Abell 1201	-0.28 - 0.28	238 ± 16

continued on next page

Table 3.5 – continued from previous page

Cluster	Spatial Binning (arcsec)	σ (km s^{-1})
PA=-25	-0.99 - -0.28	252 ± 20
	0.28 - 0.99	223 ± 15
	0.99 - 1.69	207 ± 20
Abell 383	-0.49 - 0.07	319 ± 26
	-1.06 - -0.49	228 ± 25
	-1.62 - -1.06	246 ± 32
Abell 963	-0.32 - 0.32	299 ± 22
	-0.97 - -0.32	298 ± 29
	-1.61 - -0.97	271 ± 31
	0.32 - 0.97	282 ± 26
	0.97 - 1.61	253 ± 26

Velocity Dispersion Profiles. Tabulated velocity dispersion profiles of the BCGs, not including MS 2137-23, which was presented in STE02. All slit widths are $1\farcs25$ except for Abell 963, which is $1\farcs50$. All spatial values are with respect to the center of the BCG.

3.5 Analysis and Results

We now combine the observed photometric and spectroscopic properties of the BCG and giant arcs to constrain the luminous and DM distribution in the central region of the clusters. In particular, the goal of this analysis is to determine the range of inner DM density slopes permissible and to compare these to predictions from numerical CDM simulations. The key to this method is to combine the constraints on the mass from the velocity dispersion profile with that from lensing to get a better overall measurement than can be made with each individual technique. The method used is identical to that employed by STE02, with improved numerical accuracy. There is no change in our basic conclusions on MS2137-23 from that work.

3.5.1 Mass Model and Overview of the Fitting Procedure

We adopt a spherically symmetric two component mass model comprising the BCG and cluster DM halo. We assume that the BCG is coincident with the bottom of the cluster potential. To describe the luminous BCG component we used a Jaffe (1983) mass density profile

$$\rho_L(r) = \frac{M_L r_J}{4\pi r^2 (r_J + r)^2}, \tag{3.2}$$

with total mass M_L and $R_e = 0.76 r_J$. A Jaffe profile accurately reproduces the actual surface brightness profiles of the BCGs in our sample and has the extra advantage of giving analytic solutions to the surface brightness profile and line of sight velocity dispersion. We assume that a single mass-to-light ratio accurately describes the stellar component of the mass. For a given stellar M_*/L both M_L and r_j can be deduced from the observed surface photometry. We also investigated the effects on the inner DM slope by changing the luminous mass density profile to a Hernquist profile (Hernquist, 1990) in §3.6.3 as a check for robustness of our results. Note that the PSF convolved Hernquist and Jaffe luminous matter distributions bracket the observed data in all of our clusters (see § 6.3 for a discussion).

The cluster DM halo is modeled as

$$\rho_d(r) = \frac{\rho_c \delta_c}{(r/r_{sc})^{\beta} \left[1 + (r/r_{sc})\right]^{3-\beta}} \tag{3.3}$$

which is a generalization of the numerically simulated CDM halos, with ρ_c being the critical density and δ_c a scaling factor. This density profile asymptotes to $r^{-\beta}$ at $r \ll r_{sc}$ and r^{-3} at $r \gg r_{sc}$. For values of $\beta = 1, 1.5$, the DM density profile is identical to that found by NFW and nearly identical to that of M98, respectively. Thus using this general form for the DM halo allows for direct comparison to numerical results.

Considering the observations made, there are four free parameters in our mass model: (1) the stellar mass-to-light ratio, M_*/L, (2) the inner slope of the DM

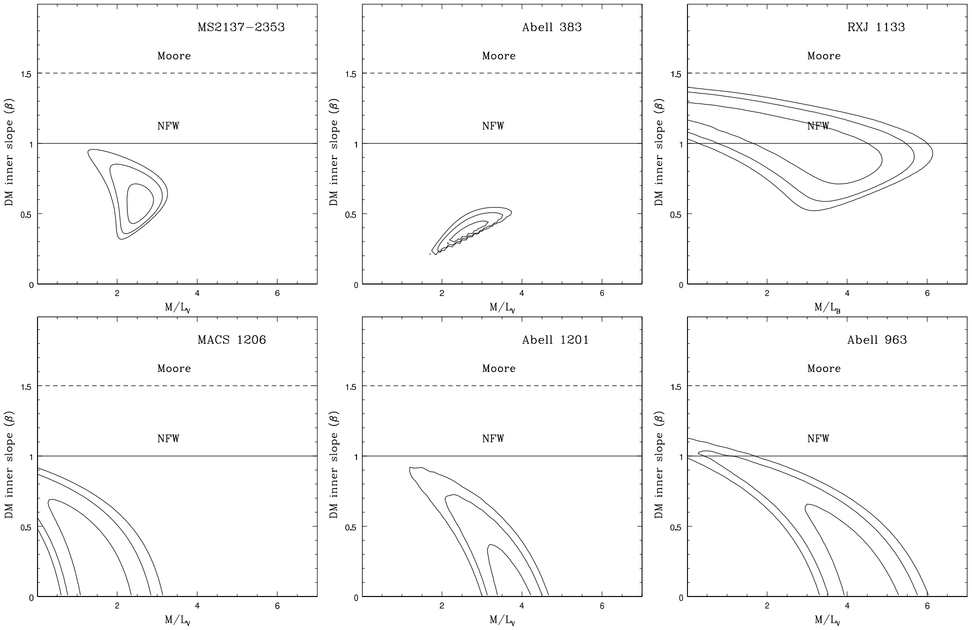

Figure 3.4: Likelihood contours (68%, 95% and 99%) obtained for the radial arc sample (top row) and the tangential arc sample (bottom row) with a Jaffe luminous distribution plus a generalized NFW DM distribution. These contours were obtained after both the lensing and dynamical analysis and marginalization with respect to δ_c.

profile β, (3) the DM density scale δ_c, and (4) the DM scale radius r_{sc}. In general, r_{sc} is much larger (greater than 100 kpc) than our most distant mass probe, tangential gravitational arcs (Bullock et al., 2001; Tasitsiomi et al., 2004). Given this, the location of the critical lines then only depend slightly on r_{sc}, since it is the projected mass that is important. In our modeling we set r_{sc}=400 kpc, leaving only three free parameters. The value of r_{sc} was chosen as a typical value seen in galaxy cluster numerical simulations for a typical cluster with virial radius of ~2 Mpc (see discussion in § 6.3). Much larger values of r_{sc} seem to be ruled out on observational grounds as well (Gavazzi et al., 2003; Kneib et al., 2003). In §6.3 we show that allowing r_{sc} to vary within reasonable bounds as proscribed by CDM simulations has a small effect on our β measurement, but that the effect is comparable to our other systematics.

We discuss in detail the analysis of both the lensing and velocity dispersion data in the Appendix. We briefly describe the method here. By comparing the observed position (and its uncertainty) of gravitational arcs with the predicted position of the arcs (given a set of free parameters $\{M_*/\mathrm{L},\beta,\ \delta_c\}$) a likelihood function can be calculated over the appropriate parameter space. Similarly, the observed velocity dispersion profile (which depends on the mass enclosed at a given radius and the relative contribution from luminous and dark matter) for a BCG in a cluster can be compared with that expected for a given set of free parameters (taking into account the seeing and spatial binning of the observations) and another likelihood function can be calculated. The total likelihood for a given set of free parameters is simply the product of the lensing likelihood and the stellar kinematics likelihood. In the next two subsections we discuss how we use these likelihood functions to place confidence limits on the inner DM density slope β.

3.5.2 Radial Arc Results

The three clusters in our sample with radial and tangential arcs (hereafter known as the radial arc sample) allow for strong constraints to be placed on the DM density profile. The tangential arc provides a measurement of the projected mass

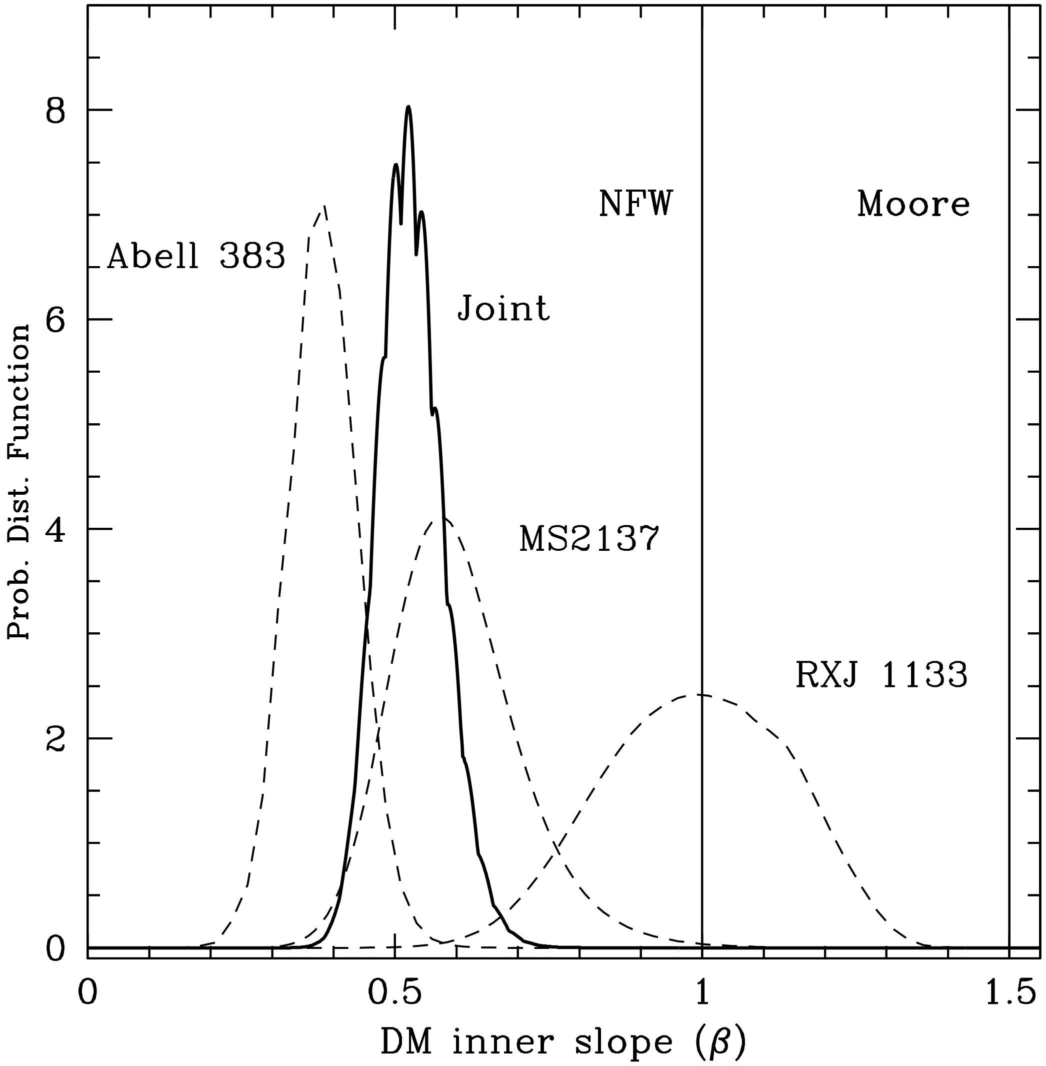

Figure 3.5: Probability distribution function of the DM inner density slope, β, for the three radial arc clusters. Note the wide scatter in preferred values of β from cluster to cluster, $\Delta\beta \sim 0.3$. The joint distribution was obtained by multiplying the individual PDFs and normalizing.

enclosed at a given radius and the radial arc gives a measurement of the derivative of the projected mass enclosed at its radius.

Assuming that all underlying distributions are normal, we can use a χ^2 minimization technique to obtain confidence contours on our parameter estimates. This involves simply taking the χ^2 difference at any point in parameter space with respect to the minimum χ^2. Confidence contours in the M_*/L-β plane allow one to visualize acceptable β values as a function of the mass of the BCG. After marginalization with respect to δ_c, the 68, 95, and 99% confidence contours in the M_*/L-β plane were placed at a $\Delta\chi^2$=2.30, 6.17, and 9.21 respectively. Figure 3 (top row) shows the contours obtained for our radial arc sample.

To constrain the inner slope β alone, we further marginalized with respect to M_*/L. The resulting probability distribution function (PDF) for β for all three clusters is shown in Figure 3.5. We adopt the peak of the distribution as best estimate of the parameters. Confidence intervals are obtained by integrating the PDF above a threshold such that the total area under the curve is 68% (95%) of the total. Doing this, we found β=$0.57^{+0.11}_{-0.08}$ ($^{+0.25}_{-0.17}$) for MS2137-23, $0.38^{+0.06}_{-0.05}$ ($^{+0.12}_{-0.11}$) for Abell 383, and $0.99^{+0.18}_{-0.14}$ ($^{+0.28}_{-0.28}$) for RXJ 1133.

Note immediately that the intervals for the individual clusters do not overlap at the 68% level. We therefore conclude that there is significant intrinsic scatter in the inner slopes of the DM halos. To assess the scatter in β values that we find in the radial arc sample, we calculate the standard deviation without account of the corresponding PDF and find $\Delta\beta$ ~0.3. The scatter and its possible consequences will be discussed in § 3.7.2.

Having noted the existence of significant intrinsic scatter, we can determine the average inner slope of DM by looking at the joint radial PDF, obtained as the product of the three individual distributions (shown in Figure 3.5 as a solid line; note that this measure is analogous to the weighted average). We find that the average inner slope and related uncertainty are $\beta = 0.52^{+0.05}_{-0.05}$ ($^{+0.11}_{-0.10}$). Assuming that our sample of clusters is representative of the entire cluster population, this means the average slope is inconsistent at $>$ 99% CL with both the NFW and

Moore profile.

3.5.3 Tangential Arc Results

Before discussing the radial arc results any further we consider the issue of sample selection bias in more detail. Are radial arc clusters a representative subsample of relaxed clusters as far as DM inner slopes are concerned? It is well known that total density distributions that are steeper than $\rho \propto r^{-2}$ do not produce radial arcs. Thus, if there is a wide range in the distribution of inner slopes, by selecting radial arc systems we might be rejecting the more cuspy systems. This bias (hereafter the radial arc selection bias) might be exacerbated by the fact that the radial arcs in our sample are buried in the BCG, a steep density profile in its own right. We investigate how robust our results on β are with respect to our choice of luminous density profile in § 3.6.3.

A clean and powerful way to address this issue is to obtain a control sample of tangential arc-only systems (hereafter the tangential arc sample). This will enable us to determine if the radial arc systems appear to be outliers in the general cluster population. At the same time this tangential arc sample will provide an additional – albeit less precise – measurement of the DM inner slope.

The bottom row in Figure 3 and 3.6 display the results for the tangential arc sample. This was subject to the same analysis as for the radial arc sample with the exception that we adopted a prior to ensure that the DM profile is monotonically declining with radius ($\beta \geq 0$). Note that the results always go toward β=0 for the tangential arc sample, at variance with the results for the radial arc sample. In fact, the shapes of the confidence contours in the M_{*}/L-β plane are markedly different from the analogous contours for the radial arc sample (see § 3.5.4). We calculated upper limit confidence levels on β, since the shape of the probability distribution function lends itself to this type of interpretation. The 68% (95 and 99%) upper limits are β =0.29 (0.62,0.82), 0.40 (0.67, 0.77), and 0.43 (0.80, 0.97) for Abell 1201, MACS 1206, and Abell 963 respectively. The joint tangential arc distribution has 68, 95, and 99% confidence upper limits of β=0.20, 0.43, and 0.57

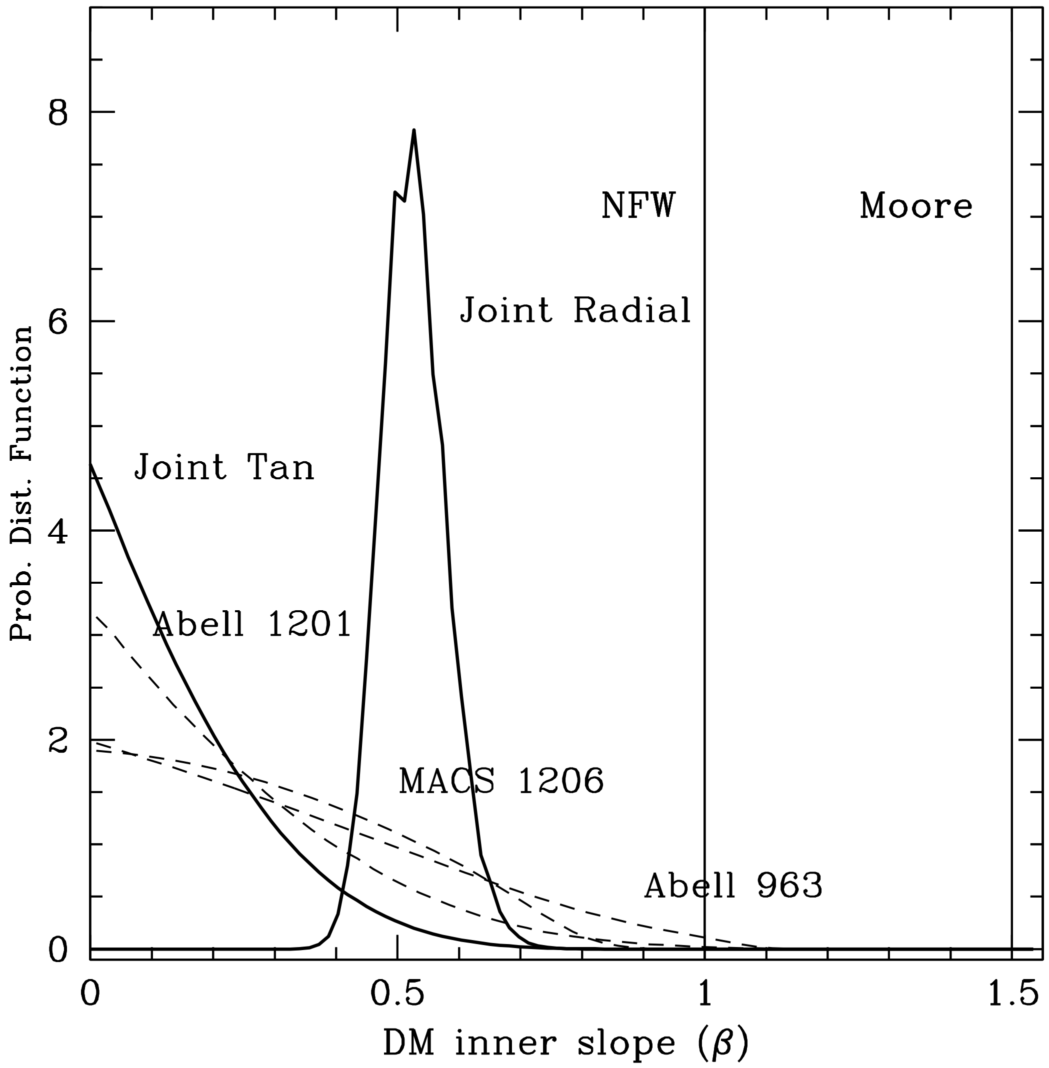

Figure 3.6: Probability distribution function of the DM inner density slope, β, for the tangential arc sample. These effectively allow us to place an upper limit on β for each cluster. Also plotted is the joint PDF for the radial arc sample and the tangential arc sample. There is no evidence that the radial arc sample is biased towards lower values of β.

respectively.

Is the radial arc sample probing an outlier population of galaxy clusters due to the fact that radial arcs cannot form in systems with density distributions steeper than $\rho \propto r^{-2}$? In the following we assume that the joint distribution for each sample is a fair representation of the underlying distribution, despite the sample size. As can be seen from Figure 3.6, the radial arc sample does not have a shallower DM density profile than the tangential arc sample, as would be expected if there was a radial arc bias. To compare the two samples, we convolved the radial and tangential arc sample probability distribution functions in order to compute the probability distribution function for the variable $\beta_r - \beta_t$, where the subscripts represent the radial and tangential arc sample values of β. Due to the one-sided nature of the tangential arc probability distribution function, it is appropriate to use upper limits to quantify the confidence region of the variable $\beta_r - \beta_t$. The value of $\beta_r - \beta_t$ is less than 0.45 and 0.57 with 68 and 95% confidence, respectively. The probability that $\beta_r - \beta_t$ is less than 0 (as would be expected if there was a radial arc bias) is $\sim 2\%$. There is no indication of radial arc bias, and the radial and tangential arc samples are reasonably consistent given the small number of systems.

3.5.4 Summary of Results

We have presented new measurements of the inner slope (β) of DM halos in clusters of galaxies, considering a sample of three radial arc systems and a sample of three tangential arc systems in carefully chosen relatively relaxed clusters.

The main results from the radial arc systems are: (i) the average $\langle\beta\rangle = 0.52 \pm 0.05$ is much smaller than that suggested by numerical DM only simulations (either NFW or Moore); (ii) our precision allows us to determine a first measurement of the intrinsic scatter in β, which we estimate to be $\Delta\beta \sim 0.3$; and (iii) individual clusters can be as cuspy as NFW (RXJ1133). The results from the tangential arc sample confirm and reinforce our findings: (i) the upper limit to the average slope is β=0.57 (99% CL), again much smaller than numerical simulations (NFW or

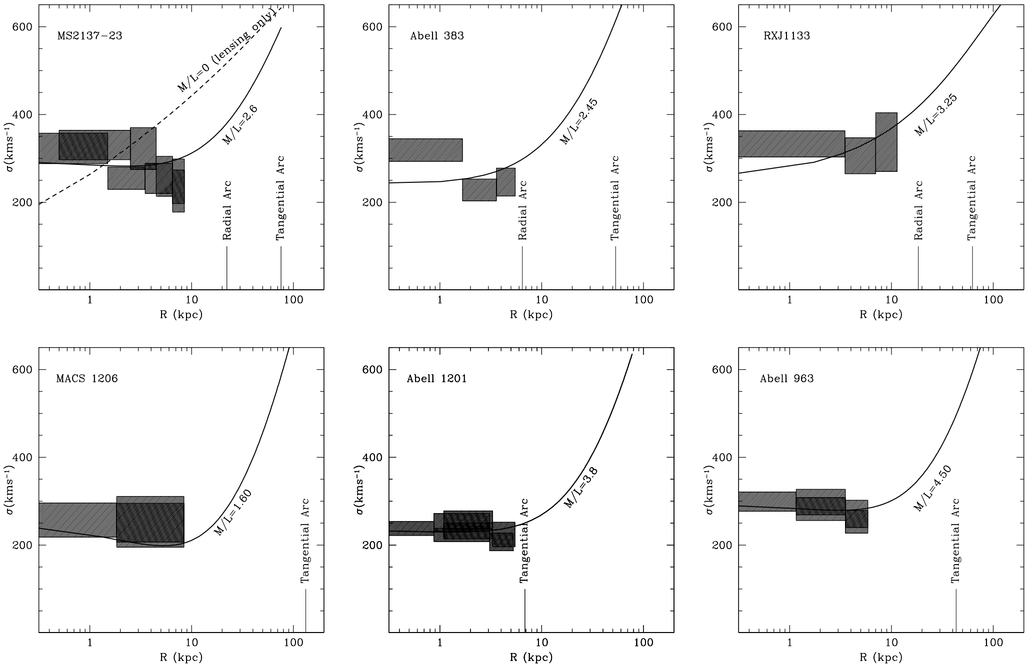

Figure 3.7: The measured velocity dispersion profile for each BCG (hatched boxes) along with the best-fitting velocity dispersion profile calculated from the combined lensing + dynamics analysis (solid curves). Note that the solid curves are not exactly equivalent to those derived from the analysis since they were not binned in accordance with the slit width, spatial binning of the measurement or smeared due to the effects of seeing. The plot of MS2137-23 (top left) illustrates the power of including the velocity dispersion profile of the BCG into our analysis. In this panel we have also shown a velocity dispersion profile from a mass model that is compatible with the lensing analysis of that cluster, but does not fit the velocity dispersion profile (β=1.30).

Moore); (ii) although with larger uncertainties, the results from the tangential arc sample are statistically consistent with those from the radial arc sample, confirming that our results are not affected by a radial arc selection bias.

Before moving on to discuss in detail the comparison with numerical simulations and consider the broader implications of these results (§3.7), we need to address two further issues. First, we would like to discuss in greater detail our method, understanding at least qualitatively some of its features. This will hopefully provide an element of physical intuition in addition to the statistical anlysis. Secondly, we need to make sure that systematic uncertainties are not dominating our error budget, which so far includes only random uncertainties. The first point is the subject of the remainder of this section. Section 4.4.3 is devoted to a careful analysis of all known systematics and related uncertainties on β.

The joint fitting of the lensing and velocity dispersion data greatly enhances our ability to distinguish between DM profiles (see STE02). The top left panel of Figure 7 illustrates why that is the case. The hatched boxes represent the velocity dispersion measurement for MS2137-23 and their 1-σ uncertainties. The solid black curve shows the best fitting velocity dispersion profile model obtained with our combined lensing and velocity dispersion analysis. The dashed curve shows a velocity dispersion profile for a set of free parameters that agrees extremely well ($\Delta\chi^2 < 1$; β=1.30) with the gravitational lensing measurements alone, but does not match the measured velocity dispersion profile of the BCG. This special case (where the M_*/L=0 indicates that the luminous component is a massless tracer of the potential) clearly shows that mass models with too steep an inner profile cannot both match the velocity dispersion profile measurement and reproduce the positions of the gravitational arcs. The remaining panels in Figure 6 plot both the observed and best-fitting velocity dispersion profile for each of the six clusters.

Our best-fitting mass models produce density profiles that are remarkably similar in their makeup (Figure 7). On $\lesssim$10 kpc scales, the matter distribution is dominated by the luminous, BCG component, with the DM component dominating at larger radii. Dubinski (1998) has found a similar result by numerically simulating the formation of a BCG in the presence of a cuspy DM halo. As can be seen from Figure 7, the velocity dispersion measurement of the BCG allows us to probe the matter distribution where luminous matter is important, while the gravitational arcs probe regions where DM dominates. The measurement techniques complement each other.

It is appropriate to assess the goodness-of-fit of our best-fitting models. While $\Delta\chi^2$ is distributed as a χ^2 distribution with three degrees of freedom (representing the three free parameters in our model), the best-fitting model (with χ^2_{min}) is distributed as a χ^2 distribution with $N-3$ degrees of freedom, where N is the number of data points and three again represents the number of free parameters (see e.g. Press et al. 1988). The total best-fitting χ^2 for each cluster is: Abell 383, χ^2/dof=8.3/2; MS2137-23, χ^2/dof=8.9/7; RXJ 1133, χ^2/dof=1.0/2; Abell 1201, χ^2/dof=6.6/6; Abell 963, χ^2/dof=2.9/3; and MACS 1206, χ^2/dof=1.4/1. Of the total, the contribution from the gravitational lensing portion of the χ^2 is never more than 0.2, meaning that the bulk is due to the velocity dispersion profile (see Figure 6 for the best-fitting velocity dispersion profiles). The one cluster with a relatively high χ^2 is Abell 383. However, given the simplicity of our mass model, this relatively high χ^2 should not be alarming. In section 6 we explore in detail possible systematic effects in our current analysis, any of which could be responsible for a less than perfect fit to the data. Since all of these systematic checks indicate that $\Delta\beta \lesssim 0.2$, we are confident in the robustness of our results.

What causes the difference in the confidence contour shapes in the M_*/L-β plane between the radial arc sample and the tangential arc sample? Both samples do not allow a steep DM inner density profiles because of their inability to match the observed BCG velocity dispersion profile described in the previous paragraph. However, it seems as if the radial arc sample is capable of pinpointing the DM inner density slope, while the tangential arc sample can give just an upper limit. Due to the functional form of the radial eigenvalue (see Equation A5), radial arcs cannot form in total density profiles steeper than $\rho \propto r^{-2}$. For our mass model, as M_*/L increases and β becomes small, the above criteria for radial arc formation

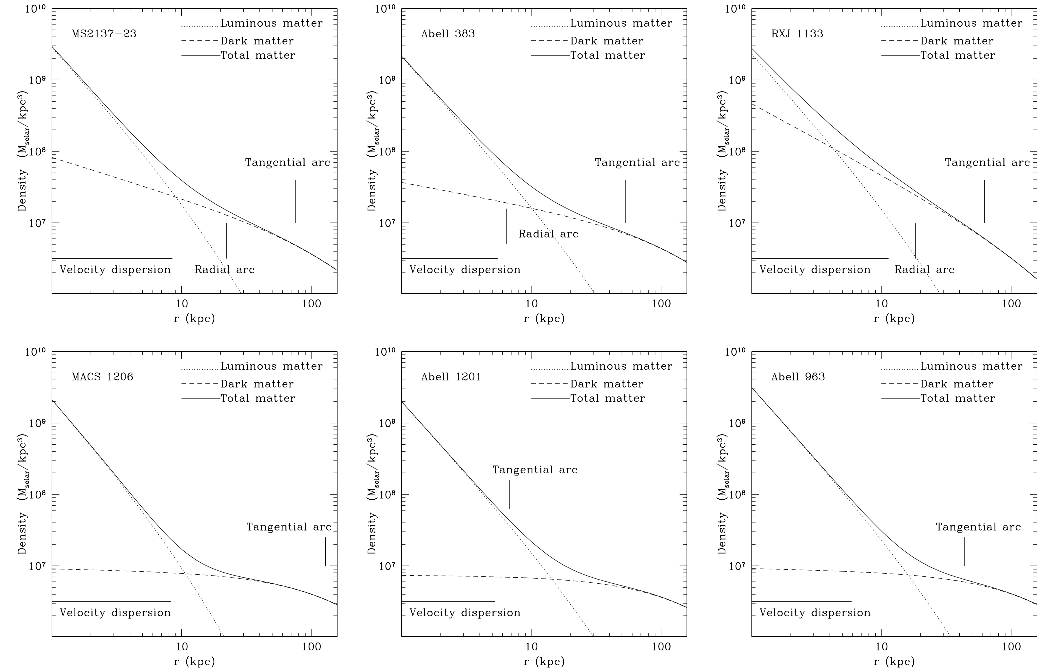

Figure 3.8: Best-fitting total density profile for the entire sample. The positions of the gravitational arcs and the range over which we were able to measure the velocity dispersion profile are noted. Within $\lesssim$ 10 kpc the total density distribution is dominated by the BCG.

is not met unless the radial arc position is pushed out radially (where DM will have a larger contribution and thus soften out the effects of the cuspy luminous distribution) to a point where it is incompatible with its observed position. It is for this reason that low values of β are not allowed in the radial arc analysis and the DM inner density slope can be pinpointed.

The summary of the results presented in this subsection are at odds with predictions of CDM simulations and have claimed to measure the intrinsic scatter in the inner DM slope, β. In order for such results to be taken seriously, it is imperative that our method is tested thoroughly with respect to our simplifying assumptions. It is our goal in the next section to systematically test all of our assumptions before we discuss the implications of our results for CDM.

3.6 Systematics

During the course of our analysis, many simplifying assumptions were made. As an exploratory study aiming to obtain tight constraints on the DM density profile, we strived to simplify our model and its inputs while still extracting the correct inner density profile. However, it is possible that these simplifications are giving systematically different values of the DM inner density slope than a more complex modeling. To judge the robustness of our method we have performed a battery of tests. First, in § 6.1, we explore the fact that we neglected both ellipticity and substructure in our lensing treatment. Second, in § 6.2, we look at possible complications in our analysis of the BCG dynamics (e.g. orbital anisotropy and template mismatch). Finally, in § 6.3 we report on tests run to check our results depending on changes in our luminous mass model and due to possible uncertainties in our measurements. Abell 383 has the tightest constraints in our sample (see § 5.2) and by using it to illustrate our test results (in § 6.2 and § 6.3) we demonstrate the impact our assumptions have on our determination of β.

3.6.1 Impact of Cluster Substructure and Ellipticity

Our cluster sample has been selected to comprise relaxed systems with no obvious signatures of strong ellipticity and/or bi–modality in their underlying mass distributions. Nevertheless, previous analyses of two of the clusters (Abell 383 and MS 2137-23) reveals that they are not perfectly circular in projection (e.g. S01; Miralda-Escudé 2002). Our simple lensing method deliberately does not attempt to fit the detailed positions of all the multiply–imaged features of the clusters, concentrating instead on the positions of relevant critical lines, estimated from visual inspection of symmetry breaks in the observed multiple–images. In this section we exploit sophisticated two–dimensional lens models to investigate whether the simplifying assumptions in our one–dimensional models introduce any systematic bias into our results. Qualitatively, the key differences between the models discussed in this section and those upon which our main analysis is based is that in this section we include the ellipticity and substructure (arising from bright cluster ellipticals) of the clusters in the models and fit the models to all of the observed multiple–image systems.

We use the LENSTOOL ray–tracing software to construct a detailed model of each of the clusters in the radial arc sample. The details of this method are explained elsewhere, and we refer the interested reader to the relevant articles (Kneib, 1993; Kneib et al., 1996; Smith et al., 2005). Briefly, we use the observed positions, redshifts, shapes and orientations of the observed multiple–image systems to constrain a model of the *total* surface mass density in each cluster core. We stress that we do not attempt to decompose the best–fit total matter distributions into their respective dark and luminous components. Each model therefore consists of the minimum number of analytic matter components (each one parametrized as a truncated pseudo–isothermal elliptical mass-distribution – /citealtKassiola93,Kneib96) required to fit the observables. In practice, each model contains a central dominant cluster–scale mass component that is centered on each BCG, plus an additional central mass component for the BCG, and a small number (≤ 4) of smaller mass components to account for contributions from likely cluster members that lie adjacent to the observed multiple–image systems. We briefly describe each model:

MS 2137-23 – This cluster has been extensively modeled by several authors (Mellier et al., 1993; Hammer et al., 1997; Gavazzi et al., 2003). We adopt STE02's spectroscopic redshifts for the dominant tangential and radial arcs as constraints on our LENSTOOL model. A four component model is able to produce an acceptable fit to these constraints ($\chi^2/\mathrm{dof} \simeq 1$). These components comprise the cluster–scale potential, the BCG and two galaxies lying $3''$ North-West of the BCG, adjacent to the radial arc (Figure 1). This model predicts a central fifth image of the galaxy that appears as the giant tangential arc that is in broad agreement with that predicted by G03's model. However, when subtracting a model of the BCG from the *HST* frame, we are unable to confirm G03's claimed detection of the fifth image. We therefore do not include this image as a constraint on the model. The ellipticity of the best–fit fiducial model is $\epsilon = (a^2 - b^2)/(a^2 + b^2) = 0.18$.

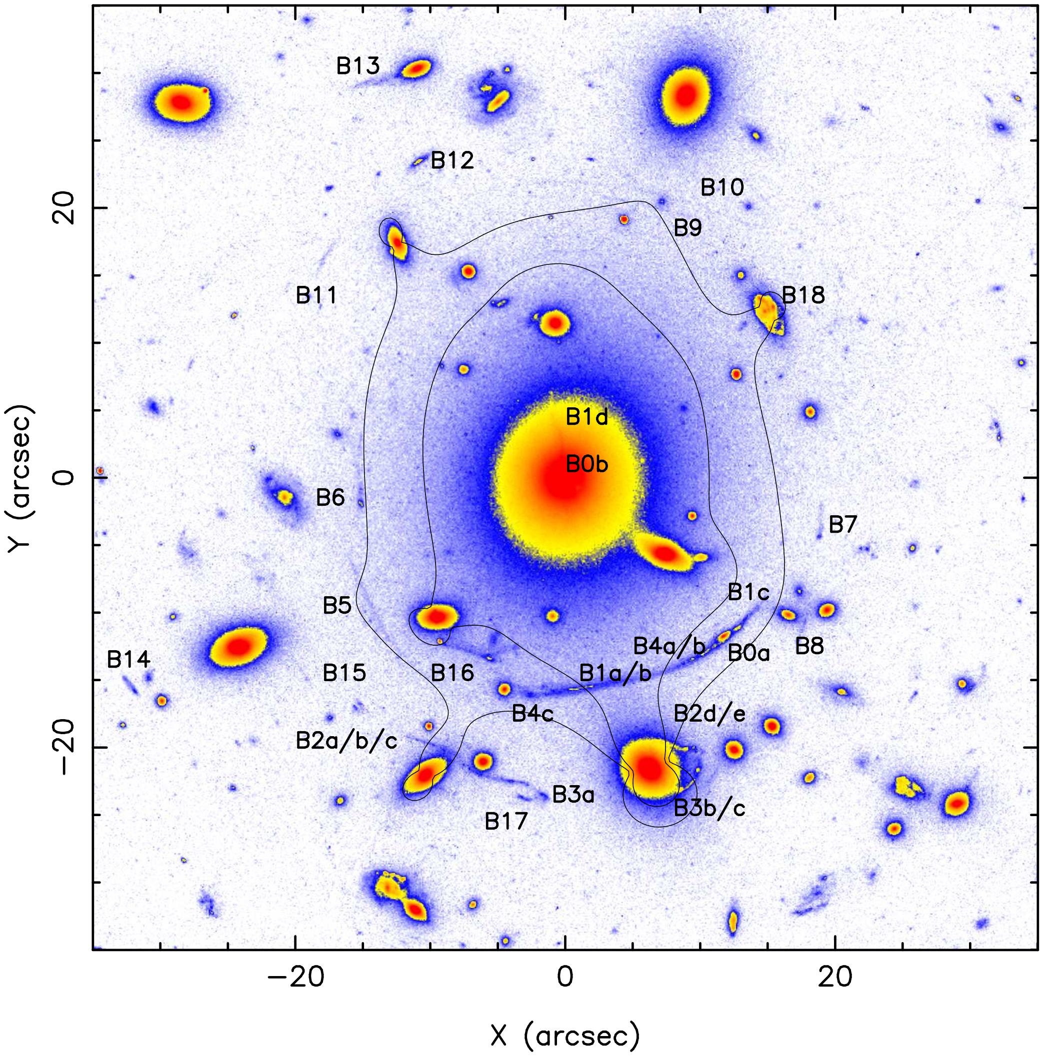

Figure 3.9: The central region of Abell 383 as seen with HST WFPC2. Overlaid are the $z = 1$ and $z = 3$ tangential critical lines calculated from the LENSTOOL analysis using the updated S01 model. The alphanumeric labels are identical to those in Fig. 1 of S01 and identify several of the lensing and cluster galaxy components used to construct the model.

Abell 383 – S01 constructed a detailed lens model of this cluster based on their spectroscopic redshift of the brightest component (B0a) of the tangential arc (see also Smith et al. 2001). We build on this analysis to add the spectroscopic redshifts of B1a/b and the radial arc into S01's model. These new spectroscopic redshifts constrain the volume of parameter space occupied by the family of acceptable models. The best–fit model lies within the family of models identified by S01 as providing an acceptable fit to the data. Figure 8 illustrates the resulting lensing model for this cluster, showing the derived tangential critical curves for $z = 1, 3$. The detailed multiple-image interpretation of this cluster is described by Smith et al. (2005).

RXJ 1133 – We identify the tangential and radial arcs as comprising two images each of the background source. The compact high surface–brightness feature in the radial arc has a profile shape and FWHM similar to a point source. The origin of this point source is unclear since it does not appear in the other lensed images. It is likely a foreground star, or possibly a transient event in the lensed galaxy that only manifests itself in the radial arc due to time delays. To obtain an acceptable fit to the lensing constraints, we use a five component model: cluster–scale potential, BCG, two dwarf galaxies adjacent to the fifth image, and the moderately bright likely cluster member $7''$ away from the BCG directly opposite these two dwarfs. The ellipticity of the best–fit fiducial model is $\epsilon = 0.19$.

After obtaining the best–fit fiducial lens model for each cluster, we systematically explored the parameter space of each model to determine the family of acceptable models ($\Delta\chi^2 \leq 1.0$). We then compare this family of models with the family of acceptable models with $\Delta\chi^2 \leq 1.0$ (projected from 3D to 2D) from the analysis presented in §5.2 (this is equivalent to the 68% confidence interval for one parameter). Fundamentally, the lensing constraints contain information about the enclosed mass at the position of the tangential arcs and the derivative of the projected mass enclosed at the position (i.e. symmetry break between the two components) of the radial arc. We extract azimuthally averaged projected density profiles from these two sets of models for each cluster and compare

$M(\leq R_{\text{tangential}})$ and $d(M/R)/dR(R_{\text{radial}})$, taking due account of the uncertainties in the determinations of $R_{\text{tangential}}$ and R_{radial}.

We plot the results of this comparison in Figure 9. The difference in $M(\leq R_{\text{tangential}})$ between the two methods is never more that 8% of that of the LENSTOOL result. Note that the 1D method presented in this work is robust in its measurement of β when the position of the tangential critical line is shifted $\pm 0\farcs5$ (see §6.3). A shift in the tangential critical line position is equivalent to changing $M(\leq R_{\text{tangential}})$, and so we defer to that subsection for a discussion of how a mismeasurement of $M(\leq R_{\text{tangential}})$ effects our conclusions on the DM density profile.

We concentrate here on the radial arc comparison, focusing on the discrepancy identified in MS 2137-23 (the most discrepant in the sample). In the following we will assume that any correction necessary in the method is solely a correction that must be made to the DM component. This is certainly a very conservative estimate since the luminous BCG mass component contributes significantly on the scales of the radial gravitational arcs. For simplicity, we assume that we are dealing with power-law surface density profiles, $\Sigma(R) \propto R^{\gamma}$. This implies that $M(< R) \propto R^{\gamma+2}$ and $\rho(r) \propto r^{\gamma-1}$. In MS2137-23, γ =-0.29 and -0.50 for the method in this work and the LENSTOOL results respectively, at the position of the radial critical line. A systematic mismeasurement of $\Delta\gamma$ =0.2 will cause a similar sized mismeasurement in the value of β: $\Delta\beta$ =0.2. This is roughly twice the size of the random error component ($\beta = 0.57^{+0.11}_{-0.08}$) quoted in §5.2 for MS2137-23. Note that the correction implied from the LENSTOOL analysis is in the direction of lower β values, even further away from predictions made by CDM numerical simulations. We conclude that any systematic effect due to the axisymmetric lens modeling in this work can affect our β measurement by of order the random error components we have calculated.

To aid comparison of our empirical measurements with future observational and theoretical studies, we list here the values of γ, assuming that $\Sigma(R) \propto R^{\gamma}$. Using the 1-D approach presented in this work, $\gamma(R_{radial}) = -0.29 \pm 0.03$ for

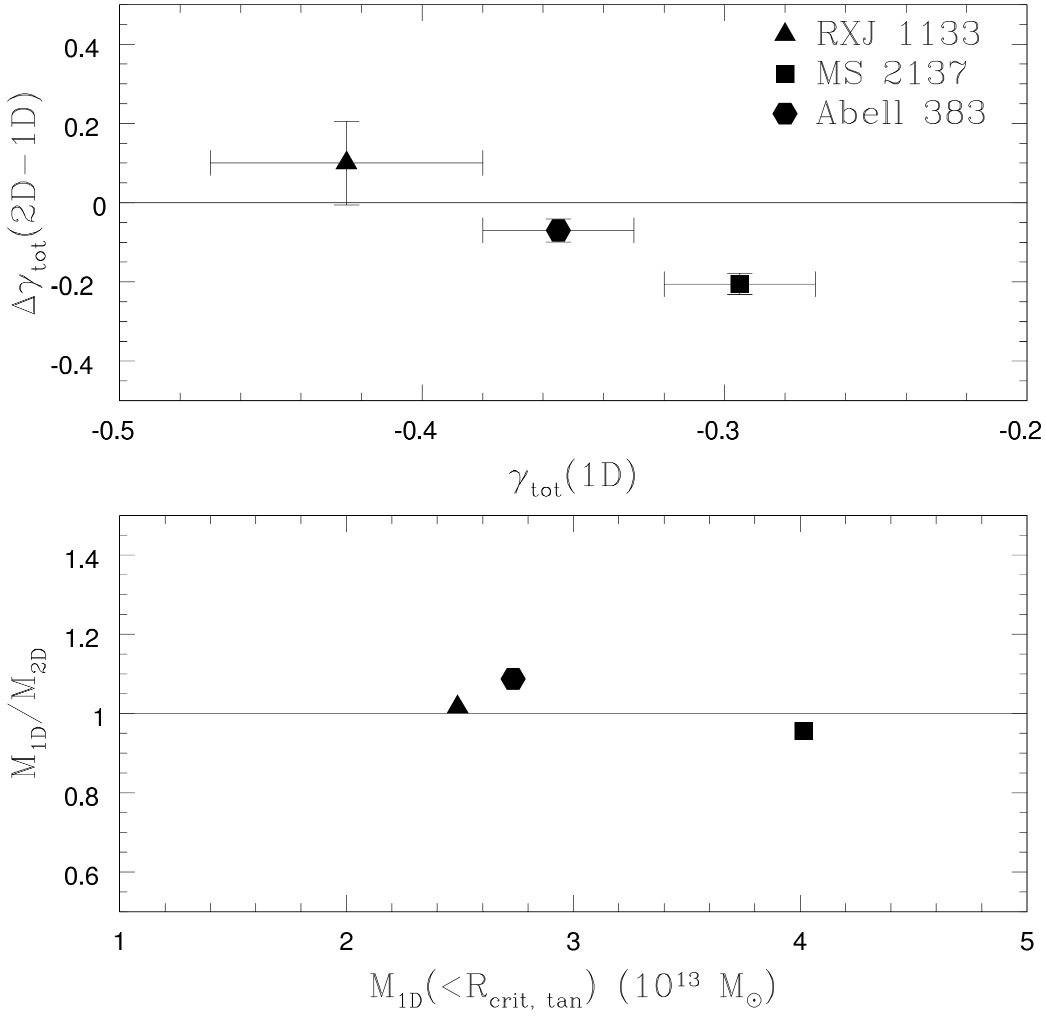

Figure 3.10: Comparison between the 1D models and the 2D check performed with the LENSTOOL software package. We use γ to parameterize the logarithmic slope of the surface density profile. At the radial critical line, γ should be identical for the two methods. (Top panel) The difference in the logarithmic slope between the two methods versus the 1D logarithmic slope. The most discrepant cluster, MS2137-23, would at most effect the DM halo by $\Delta\beta$ ~0.2 in a direction further away from that predicted by simulations. (Bottom panel) Ratio of the mass enclosed at the tangential critical line, $M(< R = R_{\rm tangential})$, for the two methods versus the mass enclosed for the 1D method. There are no deviations greater than ~8%. The uncertainties in a given data point are approximately the same size as the points themselves.

MS2137-23, -0.43 ± 0.05 for RXJ1133, and -0.36 ± 0.03 for Abell 383. With the 2D LENSTOOL analysis $\gamma(R_{radial}) = -0.50 \pm 0.01$ for MS2137-23, -0.33 ± 0.10 for RXJ1133, and -0.43 ± 0.02 for Abell 383.

3.6.2 Velocity Dispersion Measurements & Modeling

In §4.3 we presented the velocity dispersion measurements such that the final uncertainty tabulated in Table 5 is the addition in quadrature of a random component (taken from the output of the Gauss-Hermite Pixel Fitting Software) and a systematic component associated with template mismatch. Template mismatch is due to the fact that we used a single stellar spectral type to determine the kinematics of the BCGs. We quantified the effect of template mismatch in §4.3 by taking the rms deviation among the different stellar templates used to represent a possible systematic offset. While we incorporated this uncertainty into our mass modeling analysis, it is nonetheless necessary to understand how robust our results are to systematic offsets of the velocity dispersion profile. For each BCG we shifted the measured velocity dispersion profile up and down by the systematic uncertainty (typically ~15-20 km s^{-1}) and reran our analysis to determine the impact on our results. Because the typical shift in the M_*/L-β plane is about $\Delta\beta \sim \pm0.15$, and we conclude that template mismatch can not greatly alter our final results.

In our dynamical modeling of the BCGs we assumed isotropic orbits (see Appendix A.2) for the constituent stellar tracers. This assumption is justified on several grounds. From an observational point of view, Kronawitter et al. (2000) found that in their sample of galaxies the best-fitting models were nearly isotropic with typical $\alpha \simeq 0.3$ (α is the anisotropy parameter, see Appendix Equation A8) at $R_e/2$, fallin to $\alpha = 0$ at larger radii. There was little indication of any tangential ($\alpha < 0$) anisotropy in that study. Gerhard et al. (2001) obtain complementary results from an extended sample. Similar conclusions have been obtained theoretically (e.g. van Albada 1982), with strong radial anisotropy leading to instability (Merritt & Aguilar, 1985; Stiavelli & Sparke, 1991).

Nonetheless, it is still instructive to rerun the analysis with anisotropy, espe-

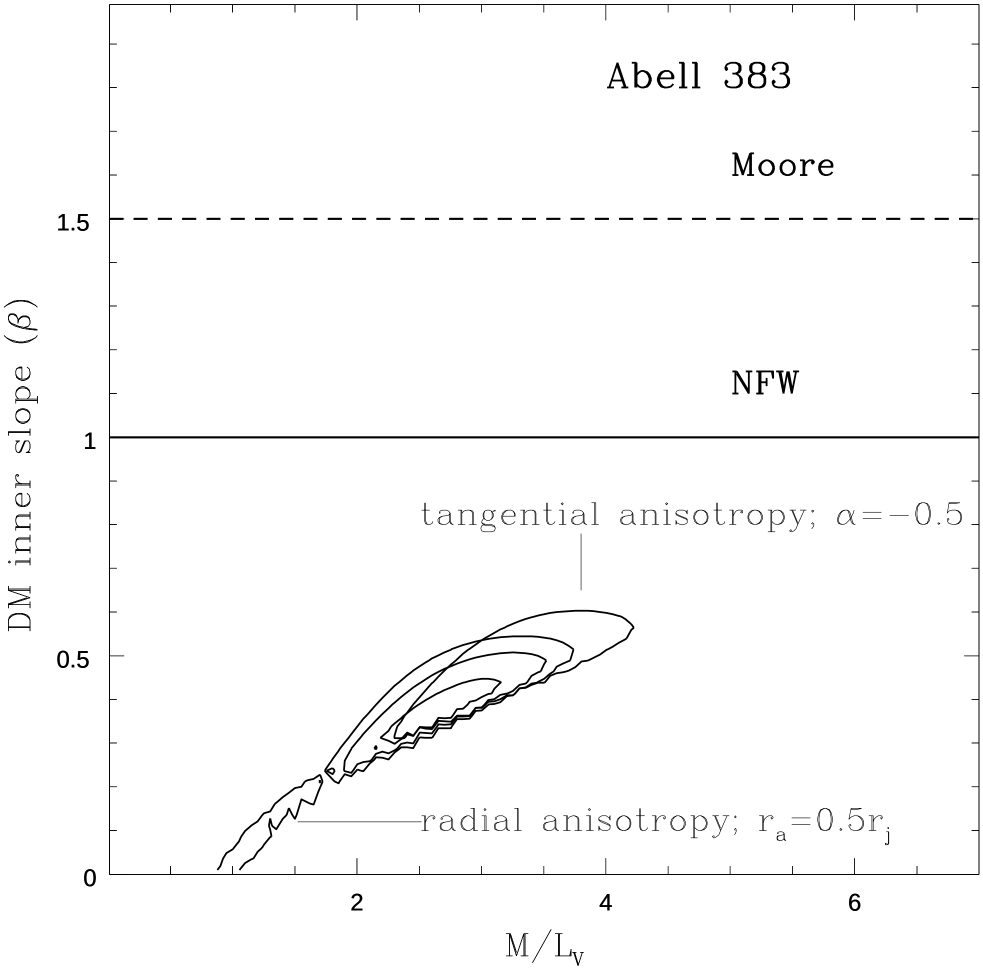

Figure 3.11: The 68%, 95% and 99% confidence contours of Abell 383 along with the 95% confidence contours for the orbital anisotropy tests in § 6.2 that were most discrepant with our original results. No test causes a shift in the β direction greater than $\Delta\beta$ ∼0.2.

cially radial anisotropy. Using an anisotropy radius, r_a (implementing the Osipkov-Merritt parametrization, Equation A8), equal to $0.5r_j$, approximately at the point where observations have indicated that orbits are somewhat radially anisotropic, we have investigated the effects on our confidence contours. Note that with this parametrization, stellar orbits become more and more radially anisotropic with increasing radius. The confidence contours in the M_*/L-β plane move towards lower acceptable values of β ($\Delta\beta \sim -0.20$ for $r_a = 0.5r_j$; see Figure 11), increasing the disagreement with predictions of N-body simulations. We conclude that modest radial anisotropy will only strengthen our claim that the observed DM profiles are shallower than predicted theoretically.

Likewise, we have introduced a constant tangential anisotropy of $\alpha = -0.5$. Observationally, tangential anisotropy in the inner regions of giant ellipticals is very rare (e.g. Kronawitter et al. 2000; Gerhard et al. 2001). As expected, the results indicate a slight steepening of the DM halos ($\Delta\beta \sim$+0.20; see Figure 11). Given the extreme case presented here, we conclude that our results are robust to slight tangential anisotropy in the BCG.

In the present work we have used Gaussian line profiles to represent the line-of-sight velocity dispersions of the BCGs. This approach provides a good low-order fit to galactic spectra, but in the outer parts of galaxies deviations from Gaussian can be of order ∼10%, leading to systematic mismeasurements of rotation velocities and velocity dispersions of the same order (van der Marel & Franx, 1993). Higher order velocity moments are routinely measured for nearby galaxies giving information on their orbital structure (e.g. Kronawitter et al. 2000; Gerhard et al. 2001; Carter et al. 1999). In the inner regions of galaxies, these studies have indicated that deviations from a Gaussian line profile are small, especially on the scales probed in this work ($\lesssim$0.5R_e). However, to make these measurements, high signal-to-noise is needed, making it hard to measure these parameters at even modest redshift due to cosmological surface brightness dimming. For this reason, we were unable to measure deviations from Gaussian line profiles in even the central regions of the BCGs. Any systematic introduced due to the Gaussian line profiles used must be small on the scales we are probing. Earlier in this section, we have shown that our results are robust to orbital anisotropies (which would lead to deviations from Gaussian line profiles). Miralda-Escudé (1995) suggested that in the rapidly rising portion of the velocity dispersion profile expected from BCGs at large radii (e.g. Figure 6) that deviations from Gaussian line profiles should be expected, even in systems with isotropic orbits. At the moment, this can only be verified in nearby BCGs where higher-order moments could be measured to high radii, beyond the scales probed in this work.

3.6.3 Other Assumptions and Measurement Uncertainties

We have subjected our data to several additional tests. We changed the luminous mass model to a Hernquist profile, systematically altered the seeing by 30%, adjusted R_e of the BCG by 10%, modified the scale radius of the DM halo, r_{sc}, and shifted the radial and tangential critical lines. All tests were performed by changing one parameter at a time. We report the results of these tests below.

(1) We replaced the Jaffe luminous density profile with a Hernquist profile to see how robust our constraints on β are with respect to our choice of the Jaffe density profile for the BCG. We have chosen the Jaffe and Hernquist profiles because they give analytic solutions to the surface brightness profile and line of sight velocity dispersion. As can be seen from Figure 2, the Jaffe and Hernquist profile bracket the data at low radii (< 1"). The Hernquist luminous mass density profile goes like $\rho \propto r^{-1}$ at small radii. A Jaffe density profile is slightly more cuspy than an $r^{1/4}$ profile, while a Hernquist profile is slightly less cuspy. We obtained confidence contours in rough agreement with the original mass model. However, a Hernquist profile give a much larger best-fitting χ^2 ($\Delta\chi^2 \sim 10$ with respect to the best-fitting Jaffe luminous density profile results). Since we are bracketing the true surface brightness profile with our Jaffe and Hernquist parameterizations and we get roughly equivalent results on β, we are confident that our choice of the Jaffe luminous distribution is not biasing our results towards shallow DM halo profiles.

(2) We argued in § 5.1 that our final results are not very sensitive to the scale

radius, r_{sc}, that we assume for the DM density profile, although there should be some dependence due to projection effects. Since it is the goal of this work to test the predictions of CDM, it is important that a range of r_{sc} compatible with numerical simulations are checked to make sure that this possible systematic is not large. Using the parameterization of the concentration parameter, c_{vir}, adopted by Bullock et al. (2001) for a $\sim 10^{15} M_{\odot}$ halo with $R_{vir} \sim 2$ Mpc, we expect r_{sc} to lie between 240 and 550 kpc (68% CL). Recently, Tasitsiomi et al. (2004) have simulated fourteen cluster-sized DM halos having cuspy profiles with mean r_{sc} of 450 ± 300 kpc. These values seem reasonable observationally as well. For example, G03's best fitting NFW profile for MS2137-23 using weak lensing had $r_{sc} = 67^{+300}_{-24}$ kpc. As a test, we briefly considered r_{sc} as a fourth free parameter, taking a flat prior on r_{sc} between 100-800 kpc, in accordance with the range of r_{sc} found by Tasitsiomi et al. (2004). After marginalization with respect to the other free parameters, this analysis caused a shift of $\Delta\beta \sim 0.15$ towards steeper values of β, giving us confidence that for reasonable values of r_{sc} our constraints on β are robust.

(3) Since the seeing is one of the measured inputs in the velocity dispersion portion of the analysis (see Equation A11 in the Appendix), we changed the seeing value by ±30% to determine how robust our conclusions are to mismeasurements in the seeing. We found shifts of $\Delta\beta \sim$0.05 and thus concluded that even significant mismeasurements in the seeing do not effect our final results.

(4) Additionally, we perturbed the positions of the effective radius of the BCG surface photometry fits by ±10%. As mentioned earlier, mismeasurements in the luminous mass distribution could possibly alter the shape of the inferred DM halo. However, changing R_e had a negligible effect on the measured confidence contours.

(5) Finally, although the visual measurement of the critical lines agrees to within 1-σ with those obtained from the 2D averaged results of the LENSTOOL analysis, we still tested to see how sound our results are to perturbations in the critical line positions. In our tests, both radial and tangential critical lines were perturbed by $\pm 0\farcs5$ from their reported positions. We found that changing the

tangential critical lines by this amount had a negligible effect, while adjusting the position of the radial critical lines produced shifts on order $\beta \lesssim 0.1$. We conclude that our results are not extremely dependent on the exact location of the critical lines.

3.6.4 Summary of Systematics

In this section, we have performed a wide variety of tests to our model and mass measurement technique, with no test indicating that our method is incomplete or lacking. The main conclusions of these tests of the systematics can be summarized as follows:

(1) In § 3.6.1, we explored the consequences of our axisymmetric gravitational lens models by comparing our results with the sophisticated 2D ray-tracing software, LENSTOOL. A comparison suggests that at most our constraints on the inner DM density logarithmic slope are shifted by $\Delta\beta \sim 0.2$.

(2) In § 3.6.2, we checked the robustness of our method in the face of possible systematics associated with the dynamics of the BCGs. Stellar template mismatch and orbital anisotropies can at most shift β by ~ 0.2.

(3) In § 3.6.3, we performed a battery of tests to check our luminous mass model and our sensitivity to the observations. The most serious effect is associated with our assumed value of r_{sc}. For reasonable values of this parameter, the inner DM density logarithmic slope is shifted by $\Delta\beta \sim 0.15$.

Figure 3.11 plots the results for those tests performed in § 3.6.2 and § 3.6.3 that produce the largest changes in our estimation of β.

3.7 Discussion

3.7.1 Comparison with Simulations

The results of N-body simulations indicate that we should expect DM inner density profiles of between $\beta = 1$ and 1.5, even with the current refinements in modern N-body work that pay special attention to issues of convergence (e.g. Power et al.

2003; Fukushige & Makino 2003). We have found a range of acceptable values of the inner logarithmic slope, with $\langle\beta\rangle = 0.52^{+0.05}_{-0.05}$, for our radial arc sample and β <0.57 (at >99% confidence) for all three clusters in our tangential arc sample. We detect scatter in our radial arc sample, which we will discuss in § 7.2.

What, therefore, can account for the apparent discrepancy between observations and simulations? There are two questions that must be addressed. First, do the scales probed in the observations correspond to those resolved in the simulations? Second, what effect do baryons have in our comparison?

In this work, we are only able to probe the mass distribution out to the distance of the tangential gravitational arc, which for our sample is <100 kpc. The original work by NFW97 had a gravitational softening radius of ∼20 kpc (for their largest mass, galaxy cluster sized halos), although it is not clear that they achieved proper convergence down to this radius. Subsequent higher resolution work (e.g. Ghigna et al. 2000; Klypin et al. 2001) focused on the issue of convergence and reported that their results for the DM density profile were reliable down to scales of ∼50 kpc at the cluster scale, and both groups found β ∼1.5. Even more recently, Power et al. (2003) and Fukushige & Makino (2003) have performed extremely high resolution simulations, with density profile results reliable down to ∼5 kpc (∼0.002 R_{vir}). Note that all of these works used different criteria for convergence. It seems safe to say that modern N-body simulations are becoming reliable down to the ∼10 kpc scale for galaxy clusters, which is comparable to the scales being probed in this study. It is also comparable to R_e in a typical giant BCG, and so it is clear that baryons should play a more central role in further investigations.

It must be emphasized that these simulations include only collisionless CDM particles. It is unclear how baryonic matter, especially in regions where it may dominate the total matter density, may affect the DM distribution. Several possible scenarios have been presented in the literature, and the following discussion is not exhaustive. One possible situation, known as adiabatic contraction, is that as baryons sink dissipatively into the bottom of the total matter potential they are likely to steepen the underlying DM distribution simply through gravitational processes (Blumenthal et al., 1986). This situation would only exacerbate the difference between our observed shallow slopes and those expected from N-body simulations. It has also been suggested by Loeb & Peebles (2003) that if stars form at high redshift ($z > 6$) before large structures form that they can be treated in a similar manner as the underlying DM particles. This scenario would suggest that instead of separating dark and luminous components of the matter distribution for comparison with simulations we should compare the total mass distribution observed with the DM distribution found in N-body simulations. However, Loeb & Peebles (2003) admit that this scenario is not strongly motivated and that some dissipative process must still take place within the baryonic material. Recently, Dekel et al. (2003) have suggested that DM halos must be as cuspy as NFW due to the merger process, unless satellite halos are disrupted at large radii, possibly due to baryonic feedback. One final scenario describes a situation in which baryonic material is initially concentrated in small clumps of mass ($\geq 0.01\%$ of the total mass) with dynamical friction causing the final DM halo shape to flatten due to these clumps (El-Zant et al., 2004, 2001). The issue of baryons must be looked into further. It is possible that the DM “core” problem cannot be resolved until baryonic material can be properly incorporated into the numerical experiments.

We have gone to great lengths in this paper to disentangle the luminous BCG component from the overall cluster DM in our mass model so that we could compare directly our results with those of N-body simulations. Albeit with considerable scatter, the average DM density profile is too shallow, especially if adiabatic contraction accurately describes the interaction between dark and baryonic matter. Does this indicate that something may be wrong with the ΛCDM paradigm of structure formation? Dark matter only simulations do not appear to be sufficient, especially as they begin to probe down to scales where complicated gaseous physics play a significant role. While work has been done to model the formation of cDs and BCGs (see e.g. Dubinski 1998; Nipoti et al. 2003), these have mainly focused on the accretion of galaxies to form cD-like objects, and have not been concerned with the resulting effect on the DM halo.

3.7.2 Is the DM Slope Universal?

This is a question that begs to be asked after looking at Figure 4. We detect an intrinsic scatter in β values of $\Delta\beta$ ~0.3 in the radial arc sample. Unfortunately, the tangential arc sample can give only an upper limit on β, and thus does not provide any further measure of the scatter.

The most recent and highest resolution N-body simulations of eight galaxy clusters performed by Fukushige & Makino (2003) did show some signs of run-to-run inner slope variations, and although they claimed that this argued against a "universal" inner DM profile, they did not quantify the scatter. Several claims have been made that the DM density profile is dependent on the DM halo mass (e.g. Ricotti 2003; Jing & Suto 2002), however, these studies have focused on the difference in slopes between different mass scales (e.g. individual galaxies versus clusters of galaxies) while the clusters in this study are all roughly the same mass. It is plausible that the formation history of any given cluster sized halo can cause a natural cosmic scatter in β (e.g. Nusser & Sheth 1999). Ultimately, numerical simulations should be able to reproduce not only the observed mean slope of the DM density profile in galaxy clusters, but also its measured scatter.

3.8 Summary

We have performed a joint gravitational lensing and dynamical analysis in the inner regions of six galaxy clusters in order to constrain the inner DM density slope β. By studying the velocity dispersion profile of the BCG, we were able to disentangle luminous and DM components of the total matter distribution in these clusters on scales $<$ 100 kpc. The main results of the paper can be summarized as follows:

1) The average inner slope of the 3 systems with both radial and tangential arcs is $\langle\beta\rangle = 0.52^{+0.05}_{-0.05}$. The 3 clusters with only tangential arcs provide an upper limit of $\beta < 0.57$ (99%CL). The measured slopes are thus inconsistent at high confidence level ($>$ 99%CL) with the cusps ($\beta = 1-1.5$) predicted by dark matter

only cosmological numerical simulations.

2) The agreement of the results from the radial arc sample and the tangential sample shows that the shallow slopes found for MS2137-23 (Sand et al., 2002) and the other radial arc systems are not the result of a selection effect.

3) Our precise measurements allow us to give a first estimate of the intrinsic scatter of the inner density DM slope ($\Delta\beta \sim 0.3$) of clusters of galaxies. The analysis of a larger sample of systems to better characterize the intrinsic scatter of the inner slope would provide a further observational test for future numerical simulations.

4) Our method is robust with respect to known systematic effects, including those related to the choice of the mass model, the description of orbital anisotropy in the dynamical models, and the simplifying assumptions inherent to our axisymmetric lensing analysis. A comprehensive and detailed analyis of these effects shows that the related systematic uncertainties on β are smaller than 0.2. Therefore, even for the system with the smallest random uncertainties (Abell 383) systematic errors do not dominate the error budget.

In conclusion, our results are in marked disagreement with the predictions of dark matter only cosmological simulations. The inclusion of baryons in the models via a simple adiabatic contraction mechanism would further steepen the theoretical dark matter halo, making the disagreement even more pronounced. Therefore, a more sophisticated treatment of baryons in the simulations appears necessary if one wants to reconcile the CDM paradigm with the present observations.

3.9 Appendix:Analysis Technique

3.9.1 Lensing

Given our simple, spherically symmetric two-component mass model, we adopted a simple lensing analysis using only the positions and redshifts of the gravitational arcs in our sample. Our method is a generalization of that used by Bartelmann (1996).

Since the extent of the galaxy cluster (lens) is much less than the distance from the observer to the lens and the lens to the source, we make the thin-screen approximation in our gravitational lensing calculations. The total surface mass density is the sum of the luminous and DM components: $\Sigma_{tot} = \Sigma_{DM} + \Sigma_L$. The surface mass density of our chosen DM halo profile, $\Sigma_{DM}(R)$, is

$$\Sigma_{DM}(R) = 2\rho_c r_{sc} \delta_c x^{1-\beta} \int_0^{\pi/2} d\theta \sin\theta (\sin\theta + x)^{\beta-3} \tag{3.4}$$

where x = R/r_{sc} (Wyithe et al., 2001). The surface mass density of the luminous component is $\Sigma_L = I(R)M_*/L$, where I(R) is given in Jaffe's (1983) original paper.

Using standard gravitational lensing nomenclature (see, e.g., Schneider et al. 1992) we describe Σ_{tot} in terms of the critical surface mass density Σ_{cr}

$$\kappa(R) = \frac{\Sigma_{tot}(R)}{\Sigma_{cr}} \tag{3.5}$$

where

$$\Sigma_{cr} = \frac{c^2}{4\pi G} \frac{D_s}{D_l D_{ls}} \tag{3.6}$$

and D_l, D_{ls}, and D_s are the angular diameter distance to the lens, between the lens and source and to the source, respectively. Another convenient quantity when describing the mapping from the source plane to the lens plane is dimensionless and proportional to the mass inside projected radius x

$$m(x) = 2 \int_0^x dy \kappa(y) y \tag{3.7}$$

With these definitions, the two eigenvalues of the Jacobian mapping between the source and image plane read:

$$\lambda_r = 1 - \frac{d}{dx}\frac{m(x)}{x}, \lambda_t = 1 - \frac{m(x)}{x^2}. \tag{3.8}$$

The root of these two equations describes the radial and tangential critical curves of the lens. Since the magnification of the source is equal to the inverse of the determinant of the Jacobian, the radial and tangential critical curves are where the magnification of the source formally diverges. While this does not happen in practice (due to the spatial extent of the source), it guarantees that when an image of a source lies near a critical line it is strongly distorted (in the radial direction in the case of radial arcs and tangentially for the case of tangential arcs). Merging lensed images merge across critical lines, providing a simple way of approximating their position by visual inspection. Thus highly distorted image pairs are an excellent way of approximating the position of the critical line for a lens. For the simple, axisymmetric lens model explored in this work, both the radial and tangential critical lines are circular with the radial critical curve always lying inside that of the tangential critical curve. Our sample of clusters (approximately round clusters with little visible substructure) was chosen specifically with this concern in mind (tests of our lens model are described in § 3.6.1). However, this is not always the case. Therefore, extreme caution must be exercised when applying our simple lens model to other samples of clusters.

Given our mass model (§5.1), the measured redshifts of the arcs and clusters, and a set of free parameters $\{M_*/\mathrm{L},\beta,\ \delta_c\}$, we can compute the predicted position of the arcs (assuming they lie very close to their associated critical line) by finding the root of the appropriate eigenvalue from Equation 4.5. By comparing the predicted position of the arcs with the actual position taken from the images, we can calculate the likelihood function,

$$P(M_*/L,\delta_c,\beta) \propto exp\{-\frac{1}{2}\Sigma_i \left[\frac{y_i - \tilde{y}_i(M_*/L,\delta_c,\beta)}{\Delta_i}\right]^2\} \tag{3.9}$$

assuming that our underlying distributions are normal. Here, y is the distance of the arc from the center of the cluster potential (as measured from the center of the BCG), Δ_i is our assigned uncertainty to the position of the critical line, and the sum in the exponential is over all the critical line arcs with known redshift.

3.9.2 Dynamics

In addition to the gravitational arc redshifts, we have also measured extended velocity dispersion profiles for all of the BCGs in our sample. This is used as an additional constraint on our mass model, using a joint likelihood analysis.

We compute the model velocity dispersion starting from the spherical Jeans Equation (Binney & Tremaine, 1987):

$$\frac{d\rho_*(r)\sigma_r^2(r)}{dr} + \frac{2\alpha(r)\rho_*(r)\sigma_r^2(r)}{r} = -\frac{GM_{enc}(r)\rho_*(r)}{r^2}, \tag{3.10}$$

where G is Newton's gravitational constant, M(r) is the three-dimensional mass enclosed, σ_r is the radial velocity dispersion. The anisotropy parameter $\alpha(r)$ is defined as,

$$\alpha(r) \equiv 1 - \frac{\sigma_\theta^2(r)}{\sigma_r^2(r)} \equiv \frac{r^2}{r^2 + r_a^2}, \tag{3.11}$$

where σ_θ is the tangential component of the velocity dispersion. The final definition introduces the Opsikov-Merritt (Merritt, 1985b,a) parameterization of anistropy that we mainly use in our dynamical models. By default, we use isotropic orbits (i.e $r_a = \infty$) that appear to be a realistic description of the inner regions of early-type galaxies. However, in §6.2 we explore the consequences of anisotropic velocity dispersion tensors on DM density profiles we measure, by considering $r_a \geq 0$ models and models with constant tangential anisotropy ($\alpha < 0$).

Using our parameterization of the anisotropy, we can readily derive the radial velocity dispersion (Binney, 1980)

$$\sigma_r^2(r) = \frac{G \int_r^\infty dr' \rho_*(r') M_{enc}(r') \frac{r_a^2 + r'^2}{r'^2}}{(r_a^2 + r^2)\rho_*(r)} \tag{3.12}$$

and the projected velocity dispersion

$$\sigma_p^2(R) = \frac{2}{(M_*/L)I(R)} \int_R^\infty dr' \left[1 - \frac{R^2}{r_a^2 + r'^2}\right] \frac{\rho_*(r')\sigma_r^2(r')r'}{(r'^2 - R^2)^{1/2}} \tag{3.13}$$

with I(R) being the surface brightness profile (modeled as a Jaffe profile with parameters derived from surface photometry).

Before comparing the model with the observations, it is necessary to take two further steps. First, we must account for the atmospheric seeing, which blurs spectroscopic measurements in the spatial direction. This can be modeled as:

$$\sigma_s^2(R) = \frac{\int d^2R' P(R - R') I(R') \sigma_p^2(R')}{\int d^2R' P(R - R') I(R')} \tag{3.14}$$

where we assume a Gaussian point-spread function, P(R-R') (see discussion in Binney & Merrifield 1998; Eqnuations 4.6-4.8). Second, we must account for the non negligible slit width and spatial binning used. This was calculated numerically such that,

$$\sigma_b^2(R) = \frac{\int_A dA' I_s(R') \sigma_s^2(R')}{\int_A dA' I_s(R)}, \tag{3.15}$$

where A is the area of the slit used for a given measurement and $I_s(R)$ is the seeing corrected intensity at a given projected radius.

With an understanding of the observational setup and seeing conditions one can calculate the expected velocity dispersion for a given set of free parameters, $\{M_*/$L,β, $\delta_c\}$. Analogous to the likelihood technique employed in the lensing appendix subsection, one can construct a likelihood for the velocity dispersion profile of the BCGs by comparing the expected velocity dispersion for a given set of free parameters with the measured velocity dispersion,

$$P(M_*/L, \delta_c, \beta) \propto exp\{-\frac{1}{2}\Sigma_i \left[\frac{\sigma_i - \tilde{\sigma}_i(M_*/L, \delta_c, \beta)}{\Delta_i}\right]^2\} \tag{3.16}$$

Here, σ is the velocity dispersion in a given bin and Δ_i is the uncertainty in the measurement.

With both the lensing and velocity dispersion likelihoods calculated, it is now possible to find constraints on the inner dark matter density slope, β. Since the two techniques are independent, the total likelihood for a given set of free parameters is just the product of the lensing and velocity dispersion likelihoods.

Chapter 4

A Systematic Search for Gravitationally-Lensed Arcs in the Hubble Space Telescope WFPC2 Archive

David J. Sand, Tommaso Treu, Richard S. Ellis and Graham P. Smith

California Institute of Technology, Astronomy, mailcode 105–24, Pasadena, CA 91125

Abstract

We present the results of a systematic search for gravitationally-lensed arcs in clusters of galaxies located in the Hubble Space Telescope Wide Field and Planetary Camera 2 data archive. By carefully examining the images of 128 clusters, we have located 12 candidate radial arcs and 104 tangential arcs, each of whose length to width ratio exceeds 7. In addition, 24 other radial arc candidates were identified with a length to width ratio of less than 7. Keck spectroscopy of 17 candidate radial arcs suggests that contamination of the radial arc sample from non-lensed objects is ∼30-50%. With our catalog, we explore the practicality of using the number ratio of radial to tangential arcs as a statistical measure of the slope β of the dark matter distribution in cluster cores (where $\rho_{DM} \propto r^{-\beta}$ at small radii). Despite the heterogeneous nature of the cluster sample, we demonstrate that this

---

[*] This chapter has been published previously as Sand et al. (2005)

abundance ratio is fairly constant across various cluster subsamples partitioned according to X-ray luminosity and optical survey depth. We develop the necessary formalism to interpret this ratio in the context of two-component mass models for cluster cores. Although the arc statistics in our survey are consistent with a range of density profiles – $\beta \lesssim 1.6$ depending on various assumptions, we show that one of the prime limiting factors is the distribution of stellar masses for the brightest cluster galaxies. We discuss the prospects for improving the observational constraints and thereby provide a reliable statistical constraint on cluster dark matter profiles on $\lesssim$100 kpc scales.

4.1 Introduction

The imaging cameras on Hubble Space Telescope (*HST*) provide a valuable resource for studies of gravitational lensing. For example, the improved image quality compared to ground-based telescopes has enabled the morphological recognition of tangential arcs (e.g. Smail et al. 1996; Kneib et al. 1996; Gioia et al. 1998). The analysis of such arcs has led to detailed mass models of great utility both in determining dark and baryonic mass distributions (e.g. Kneib et al. 2003; Gavazzi et al. 2003; Smith et al. 2005) and in the study of highly magnified distant galaxies (e.g. Franx et al. 1997; Seitz et al. 1998; Pettini et al. 2000; Smith et al. 2002; Swinbank et al. 2003; Ellis et al. 2001; Kneib et al. 2004; Santos et al. 2004).

HST images have also been invaluable in studying *radial* gravitationally-lensed arcs (e.g. Gioia et al. 1998; Smith et al. 2001; Sand et al. 2002, 2004). These arcs are often embedded in the envelope of the central luminous cluster galaxy and thus a high angular resolution is essential to uncover their presence. Radial arcs straddle the inner critical line whose location has long been known to provide a valuable constraint on the form of the mass profile on $\lesssim$100 kpc scales (e.g. Fort et al. 1992; Miralda-Escude 1993, 1995; Bartelmann 1996; Williams et al. 1999; Meneghetti et al. 2001).

A long-standing field of inquiry has been the comparison of theoretical predictions and ground-based observations of the *abundance of arcs* for example as a constraint on cosmology. Bartelmann et al. (1998) originally found that the number of strongly-lensed arcs greatly exceeds that expected from ΛCDM simulations, preferring instead an open CDM cosmology. Various systematic effects have been proposed to explain the apparent excess, including cluster substructure (e.g. Flores et al. 2000; Torri et al. 2004), the influence of the brightest cluster galaxy (BCG; Meneghetti et al. 2003a), and uncertainties in the background redshift distribution of lensed sources (Dalal et al., 2004; Wambsganss et al., 2004). Many of these effects can be calibrated through high resolution simulations of galaxy clusters and accurate background redshift distributions based on photometric redshift surveys. Indeed, several recent articles reconcile the expected number of gravitational arcs in a ΛCDM universe with observations (Dalal et al., 2004; Wambsganss et al., 2004; Oguri et al., 2005), and attention is now focusing on how to use such observations to constrain dark energy models (e.g. Meneghetti et al. 2004; Dalal et al. 2005).

It is also possible to use arc statistics to constrain the *central density profiles* of clusters (e.g. Wyithe et al. 2001), thereby testing the prediction that CDM halos have profiles steeper than $\rho \propto r^{-1.0}$ (e.g. Navarro et al. 1997; Moore et al. 1998; Power et al. 2003; Fukushige et al. 2004; Tasitsiomi et al. 2004; Diemand et al. 2004). These analyses are subject to uncertainties and systematics similar to those discussed above.

To date, several ground-based optical surveys have been used for statistical studies of gravitational arcs (e.g. Le Fevre et al. 1994; Luppino et al. 1999; Zaritsky & Gonzalez 2003; Gladders et al. 2003). Despite different cluster selection and redshift criteria, these surveys have measured roughly comparable giant tangential gravitational arc incidences which have guided theoretical understanding of the processes responsible for strong lensing on the galaxy cluster scale. Given typical ground based seeing, however, these are of marginal utility in searches for radially-elongated thin, faint arcs buried in the halos of bright cluster galaxies.

The primary goal of this paper is to compile a list of the gravitationally lensed arcs found in the HST/WFPC2 archive and to explore the feasibility of using the number ratio of radial to tangential arcs as a means of constraining the inner density profiles in cluster cores. Molikawa & Hattori (2001) have shown that the abundance ratio of radial to tangential arcs is sensitive to the mean density profile of the cluster sample. Oguri et al. (2001) studied the predicted ratio of radial to tangential arcs as a function of not only the inner dark matter density slope, but the concentration parameter, c, of the halos as well. Oguri (2002; hereafter O02; see also Keeton 2001) has suggested that the various systematics that effect the cross section for lensing are significantly reduced when considering the number ratio of radial to tangential arcs rather than their absolute number. To constrain the dark matter density profile, we adopt the methodology presented by O02, extending their technique to include a second mass component arising from the central cluster galaxy. Our analysis is intended to complement studies of the DM density profile in clusters performed on individual systems (e.g. Kneib et al. 2003; Smith et al. 2001; Gavazzi et al. 2003; Sand et al. 2002, 2004; Buote & Lewis 2004; Łokas & Mamon 2003; Kelson et al. 2002) and through other statistical techniques (e.g. van der Marel et al. 2000; Dahle et al. 2003; Mahdavi & Geller 2004).

A plan of the paper follows. In §2 we discuss the archival sample of clusters, how representative sub-samples can be defined for later analyses, and describe our reduction procedure. In §3 we describe the procedures we adopted for identifying lensed arcs and how they are characterized by their length-to-width ratio. We also present new follow-up spectroscopy for several candidate radial arcs as a means of estimating the likely contamination by other sources (e.g. foreground galaxies). In §4 we present our methodology for calculating the expected radial to tangential arc number ratio and discuss the various assumptions and their limitations. In §5 we derive constraints on the inner DM density slope and discuss our results. In §6 we summarize and discuss future prospects for improving the constraints. An Appendix describes and presents the cluster catalog, arc catalog, and finding charts for the newly-located radial arcs.

Throughout this paper, we adopt r as the radial coordinate in 3-D space and R as the radial coordinate in 2-D projected space. We assume H_0=65 km $s^{-1}Mpc^{-1}$,

$\Omega_m = 0.3$, and Ω_Λ=0.7.

4.2 Cluster Selection

The Hubble Space Telescope data archive is now sufficiently extensive to provide the basis for a search for gravitational arcs in galaxy clusters. In this work, we restricted our search to images taken with the Wide Field Planetary Camera 2 (WFPC2). Exploitation of the archival set of images taken with the more recently-installed and superior Advanced Camera for Surveys (ACS) is left for a future study.

As the overarching goal is to identify all tangentially and radially-elongated gravitational arcs, regardless of any preordained intrinsic property of the galaxy cluster, fairly liberal criteria were used for selecting observations from the archive. Only clusters of known redshift with $0.1 < z < 0.8$ were considered. We stipulated that images of the cluster had to be available in one or more of the following broad band filters: F450W, F555W, F606W, F675W, F702W, and F814W. Procedurally, an abstract search was done on the HST archive and proposals containing the words "galaxy" and "cluster" or "group" were flagged. This initial list of abstracts was pared by inspection, so that only data for those proposals directed at galaxy clusters or groups were requested. All of the data from this edited abstract list was requested if they satisfied the camera, filter, and redshift requirements. This search technique ensured only programs deliberately targetting clusters were examined.

The resulting cluster catalog is listed in Table 4.3, in the Appendix. The total sample includes 128 galaxy clusters. A histogram of the redshift distribution is shown in Figure 4.1.

4.2.1 Uniform Cluster Subsamples

The resulting cluster sample is heterogenous with factors such as exposure time, redshift, richness/mass/X-ray luminosity, and filter choice, all affecting the sensitivity to gravitational arcs. Although this may not seriously affect our goal of

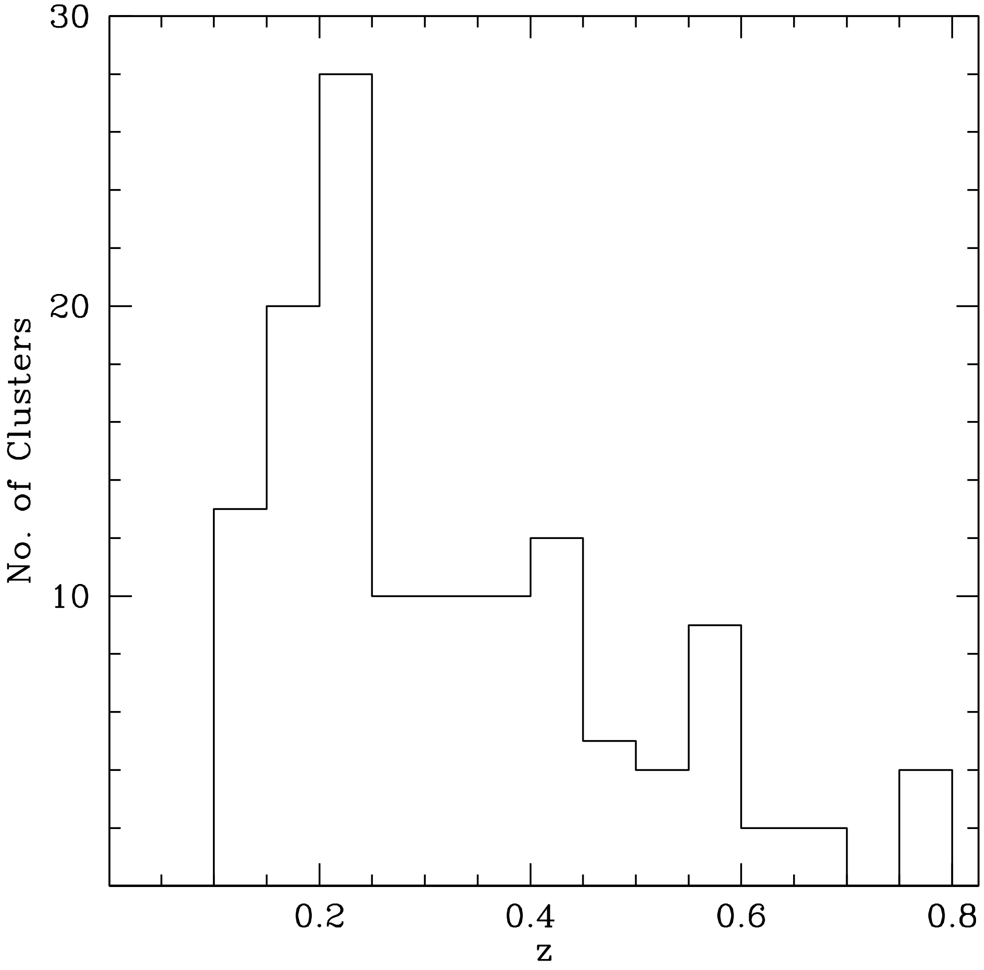

Figure 4.1: Histogram illustrating the number of clusters in the sample as a function of redshift.

measuring the abundance ratio of radial to tangential arcs and constraining the inner slope of the DM density profile (see O02; the arc ratio is relatively robust with respect to cluster mass and observational selection effects), it is helpful to consider the possibility of partitioning the large sample into more complete subsets for later use. Membership of each cluster in the various sub-samples introduced below is indicated in Table 4.3.

X-ray selected sub-samples will be beneficial given the correlation between cluster mass and X-ray luminosity. We define two in particular that have been discussed in the literature and which link directly to specific HST programs.

1.*Smith sample:* This sample follows the work of Smith et al. (2001,2002a,2002b,2003,2005) and includes 10 clusters. Clusters in this sample are X-ray luminous ($L_{\rm X} > 8\times10^{44}$ ergs s^{-1}; 0.1-2.4 keV; Ebeling et al. 1996) and lie in the redshift range $0.17 < z < 0.25$.

2.*EMSS sample:* Another X-ray sub-sample can be drawn from the EMSS cluster survey (0.3-3.5 keV; limiting sensitivity of 5×10^{-14} ergs cm^2 s^{-1}; **?**). Of the 93 clusters identified by Henry et al. twelve have been imaged with HST/WFPC2. Two previous gravitational arc searches were conducted with a subsample of this kind using ground-based images (Le Fevre et al., 1994; Luppino et al., 1999).

3. *Edge sample:* This refers to a sample of clusters whose imaging was conducted to a uniform depth (although the clusters are not all the same redshift). Such a sample should, broadly speaking, pick out all lensed features to a certain surface brightness threshold. Two large SNAPSHOT programs are prominent in this respect: PID 8301 and 8719 (PI: Edge) which image together 44 z >0.1 clusters in the F606W filter with exposure times between 0.6 and 1.0 ks. According to the HST proposals, this program sought to understand the morphological properties of central cluster galaxies. Clusters were selected from the Brightest Cluster Sample (BCS – Ebeling et al. 1998) for which optical spectra of the central cluster galaxies are available (Crawford et al., 1999). The primary sample was selected from those BCS clusters hosting a BCG with optical line emission. A secondary control sample of BCS clusters that do not host an optical line emitting BCG

was also selected to span the same range in redshift and X–ray luminosity as the primary sample (Edge, private communication). Optical line emission from BCGs is one of the least ambiguous indicators of clusters for which the central cooling timescale is less than the Hubble time (Crawford et al., 1999). These "cooling flow" clusters are also typically classified as relaxed clusters (e.g. Smith et al. 2005). The clusters in the control sample were also selected to appear relaxed at optical and X–ray wavelengths. While there are undoubtedly some exceptions (e.g. Edge et al. 2003), the "Edge sample" is likely dominated by relaxed clusters.

4.2.2 WFPC2 Data Reduction

Although our cluster sample is drawn from the HST/WFPC2 archive, the various goals of each original program means the observing strategy varied from case to case. Fortunately, there are only two basic approaches to taking the observations. The first includes those CRSPLIT or SNAPSHOT observations in which two or more non-dithered exposures were taken. The second refers to the case where two or more dithered (either with integer or half-integer pixel offsets) exposures were taken either to enhance the sampling of the WFPC2 point spread function or for better cosmic ray removal (or both). A standard data reduction script was written for each of these cases and is described here briefly.

In the SNAPSHOT case, cosmic ray rejection was first performed on each individual exposure using the IRAF task LACOSMIC (van Dokkum, 2001). The cleaned images were then combined with the task CRREJ, which also served to remove residual cosmic ray hits. Background counts subtracted from each of the WFPC2 chips were noted and used in later photometric calculations. The WFPC2 chips were combined using the IRAF task WMOSAIC.

For the multiple dithered exposures, the data were reduced using the IRAF package DRIZZLE (Fruchter & Hook, 2002) with a fixed parameter set. In particular, the final pixel size (represented by the DRIZZLE.SCALE parameter) was set to 0.5 resulting in a pixel size half that of the original image. The drizzled "drop" size (represented by the DRIZZLE.PIXFRAC parameter) was set to 0.8 regardless of

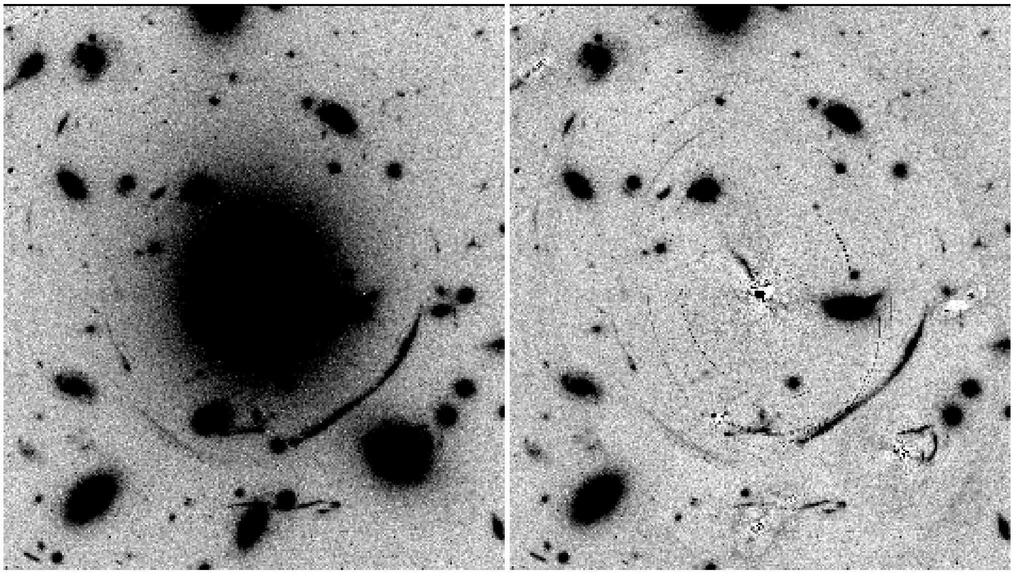

Figure 4.2: An example of galaxy subtraction performed to secure photometry and length to width ratio for the arcs in Abell 383. Although the galaxy subtraction process leaves tangentially-oriented residuals, these are easily distinguished from true arc candidates by visual inspection. Radial arc candidates will not generally be confused with these residuals.

the observational program. The final images of the WFPC2 chips were combined using the IRAF task GPREP. The sky background determined for each WFPC2 chip was again noted for later photometric use.

To aid in locating radial arcs, which are often buried in the halo of the BCG, we also examined images after subtracting the (assumed symmetrical) light of the most luminous galaxies (usually but not always just the central member). In order to do this, we employed the IRAF task ELLIPSE allowing both the position angle and ellipticity of the fitted isophotes to vary as a function of semi-major axis. We discuss in §3.1, §3.2, and §3.3 how the galaxy subtraction and residuals might affect arc identification, photometry, and derived length to width ratios, respectively.

4.3 The Arc Sample

In this section we discuss how the sample of tangential and radial arcs were identified in a consistent manner from the reduced data. The resulting catalog is presented in Table 4.4 in the Appendix.

4.3.1 Arc Identification

Each mosaiced image was visually examined for lensed features by one of the authors (DJS), both in its original and bright galaxy-subtracted incarnations. A candidate gravitational arc was designated according to one of two categories: tangential or radial arc. The distinction between tangential and radial arcs is determined by the arc orientation with respect to the cluster center (assumed to be roughly coincident with the dominant BCG) and is rarely ambiguous, even in bi- or multi-modal clusters. Twenty-five of the HST clusters were also examined by one other author (TT). Within this subsample, DJS found 2 radial and 37 tangential arcs with a $L/W > 7$ (see §4.4.1 for justification of this L/W criterion), while TT found 2 radial and 41 tangential arcs, resulting in arc number ratios of $0.054^{+0.077}_{-0.036}$ and $0.049^{+0.069}_{-0.032}$, respectively. Thirty-six of the tangential arcs and both of the radial arcs were in common between the two samples. Given the consistency between these measurements, we conclude that our results are not sensitive to the person doing the identification.

A serious concern given our motivation to measure the *ratio* of the radial to tangential arcs, is the likelihood that radial arcs are harder to locate in the noisier region underneath the envelope of the brightest cluster galaxy. Taking the ten cluster Smith sample (see § 4.2.1) as an example, we find the rms background noise to be 1.5 to 3 times higher in the central regions after galaxy subtraction than in the periphery of the WFPC2 fields appropriate for the identification of tangential arcs. To investigate the bias this might cause in the preferential loss of radial arcs at a given image surface brightness, we re-examined the selection of tangential arcs after artificially increasing the background noise by a factor 3. Of the 38 tangential arcs (with $L/W > 7$) observed in the Smith sample (see Table 4.2), 32 were still identifiable as arcs after the background noise was increased. This implies that ∼20% more radial arcs would be found if they were looked for at an identical surface brightness limit as the tangential arc population. On its own, this systematic effect does not affect our conclusions on the mean dark matter density profile in this cluster sample, as will be shown in § 4.5.

When searching for radial arcs, our strategy of examining images after central galaxy subtraction is best suited for the case of a single, dominant central galaxy. However, eight clusters in our sample contain multiple bright galaxies in their core for which our central galaxy subtraction technique is less effective. The conservative results presented in § 4.5 do not change within the uncertainties if these clusters are excluded from our study. The photometric properties and length-to-width ratio (L/W) of arcs found in these clusters are also less certain than those found in clusters dominated by a single central galaxy (see Table 4.4 for details).

4.3.2 Arc Photometry

Photometric magnitudes were measured for all candidate arcs. This is a complex task for two reasons. First, arcs are by definition often highly distorted, making them poorly-suited to automatic source identification codes such as SExtractor

(Bertin & Arnouts, 1996). Second, contamination from bright, nearby galaxies can affect the result, particularly for the radial arcs buried in galaxy halos.

Our procedure was as follows. Polygonal apertures were determined for each arc using the IRAF task POLYMARK. Additionally, all possible galaxy interlopers were digitally subtracted with ELLIPSE (in addition to the BCG; see § 4.2.2), as illustrated for Abell 383 in Figure 4.2. In order to measure the photometric uncertainties, a master "sky" frame was made by summing the initial sky subtraction of the image (see § 4.2.2) and the subtracted contaminating galaxies. Identical apertures were applied to both the "sky" frame and the object frames to determine the magnitude and associated uncertainty for each arc.

The subtraction of flux from cluster galaxies adjacent to an arc is not a perfect process. The subtraction of these galaxies leaves residuals which typically appear as thin ($< 2-3$ pixels), tangentially oriented features (see Figure 4.2). Fortunately, upon close inspection these are readily distinguished from true gravitational arcs. Other residuals arise from nearby WFPC2 chip boundaries, tidal features in the cluster, double nuclei in BCGs, dust-lanes, and spiral arms. Those arc candidates whose photometry appears to have been compromised due to such residuals are flagged in Table 4.4 in the Appendix. Both the photometry and measured L/W for these flagged objects are more uncertain than the formal uncertainty listed in the table.

4.3.3 Arc Length-to-Width Ratio

The arc length-to-width ratio (L/W) is often used for characterizing how strongly a source has been lensed. Limiting our arc sample according to some L/W criterion provides a means for undertaking comparisons with earlier work and with theoretical predictions (e.g. Bartelmann & Weiss 1994).

In practice, we measured L/W ratios at three different signal to noise per pixel thresholds: 2.0,1.5 and 1.0. The mean and rms of these three measurements is given in Table 4.4. All L/W measurements were done on the polygonal apertures used for photometry, limiting the possibility of contamination from nearby sources, and also limiting the chances of a very spurious L/W measurement. In the case where a cluster has multi-band data, the final L/W ratio is the mean found across the bands and the uncertainty includes measures in all bands. Arc lengths are measured by first finding the intensity weighted centroid of the arc within the same polygonal aperture that was used to obtain photometry. From there, the pixel furthest from the arc centroid above the threshold S/N is calculated. Finally, the pixel (above the S/N threshold) furthest from this pixel is found. The final arc length is the sum of the two line segments connecting these three points. The width is simply the ratio of the contiguous area above the S/N threshold to the length. If the arc width was found to be $<0\farcs3$ (the typical WFPC2 PSF is $\sim0\farcs15$), then the feature was determined to be unresolved in that direction. In this case, the measured L/W is a lower limit (with the width set to $0\farcs3$) as noted in Table 4.4. As discussed in the arc photometry subsection, there are several arcs whose L/W measurement was possibly compromised due to residuals from the galaxy subtraction technique, and these arcs have been flagged in Table 4.4.

Because this is the first systematic search for radial arcs, all candidates are presented in Table 4.4 with an accompanying finding chart in Figure 4.9, regardless of their L/W. For the tangential arcs, only those with $L/W > 7$ are presented, unless there is a spectroscopically-confirmed redshift in the literature (even though these arcs were not used in our final analysis, § 4.5).

4.3.4 Spectroscopic Follow-Up

To gauge possible contamination of the radial arc candidate list by non-lensed sources, we have undertaken a limited Keck spectroscopic campaign as part of our quest to obtain deep spectroscopy of lensed systems for detailed individual study (Sand et al., 2002, 2004). Possible sources of contamination in the arc candidate list include optical jets and cooling flow features associated with the central cluster galaxy and foreground edge-on disk galaxies. A summary of the spectroscopic results are given in Table 4.1. In this table we also present a compilation of spectroscopic redshifts for several tangential arcs (those which have not yet been published). The new arc spectra are shown in Figure 4.3.

Table 4.1: New Spectroscopic Observations

Cluster	Date	Target	Instrument	Exposure time (ks)	Redshift	Notes
Abell 2259	July 27, 2001	Tan Arc	ESI	7.2	1.477	Arc A1
MS 1455	July 27, 2001	Rad Arc Cand	ESI	4.5	-	Not lensed
Abell 370	Oct 19, 2001	Rad Arc	LRIS	7.2	-	No detection
Abell 1835	April 11, 2002	Rad Arc	ESI	1.8	-	No detection
Abell 963	Nov 22, 2003	Tan Arc	LRIS	7.2	1.958	Arc H1
GC0848+44	Feb 22, 2004	Rad Arc	LRIS	3.0	-	Faint Cont.
Abell 773	Feb 22, 2004	Tan Arc	LRIS	5.4	1.114	Arc F11
GC 1444	July 19, 2004	Rad Arc	ESI	7.2	1.151	Arc A1
3c435a	July 19, 2004	Rad Arc Cand	ESI	5.4	-	Not lensed
Abell 2667	July 19, 2004	Rad Arc Cand	ESI	3.6	-	Not lensed
Abell 2667	July 19, 2004	Tan Arc	ESI	3.6	1.034	Arc A1
AC 118	July 19,20, 2004	2 Rad Arc	ESI	4.6/7.2	-	Faint Cont.
MS 0440	Dec 12, 2004	Rad Arc	LRIS	5.4	-	No detection; arc A17
IRAS 0910	Dec 12, 2004	Rad Arc	LRIS	0.6	-	Not lensed
3c220	Dec 12, 2004	Rad Arc	LRIS	2.4	-	Not lensed
R0451	Dec 13, 2004	Tan Arc	LRIS	3.6	2.007	Arc A1
RCS0224	Dec 13, 2004	Rad Arc	LRIS	5.4	1.050	Arc R1

Discussing the radial arc candidates in more detail:

- *GC 1444 & RCS 0224:* These are the new radial arc redshifts presented in this work, based on single emission lines assumed to be O[II]. Both radial arc candidates have continuum blueward of the emission line making its interpretation as Lyα unlikely.

- *Abell 370, Abell 773, GC0848, Abell 1835, MS0440 and AC118:* The spectra of these radial arc candidates were inconclusive. The spectrum was either faint and featureless or not detected at all. Note that spectra were taken for two radial arc candidates in AC118 (A1 and A2). The spectral coverage of all observations was continuous between ∼4000 and 10,000 Å.

- *MS 1455, 3c435a, 3c220, IRAS 0910 & A2667:* These radial arc candidates are sources at the cluster redshift. The spectra exhibit numerous emission

> lines including: [OII], Hγ, Hβ, [OIII] 4959 and 5007, [O I] 6300 and 6363, [NII] 6548, Hα, [N II] 6583, and [SII] 6716 and 6731. These features each have velocity structures that can span hundreds of kilometers per second.

In addition to the spectroscopy presented in Sand et al. (2002, 2004), we have now attempted spectroscopic verification for 17 candidate radial arcs. Five spectra are consistent with the lensing hypothesis (Abell 383, MS2137, GC1444, RCS0224 (arc R1) and RXJ1133), seven are inconclusive (Abell 370, Abell 773, GC0848, Abell 1835, MS0440 and two arcs in AC118), and five turn out to be spectroscopically coincident with the cluster redshift (MS1455, 3c435a, 3c220, IRAS 0910 and A2667).

Although not all radial candidates selected for Keck spectroscopy have L/W >7, it is fair to assume this sample is representative of the archive catalog list, since targets were selected on availability at the telescope (e.g. RA & DEC) and not towards arcs with any specific quality. A key issue, however, in deriving a contamination fraction is the question of the identity of those candidate radial arcs whose nature we were unable to confirm. Most likely these are either optical synchrotron jets associated with the BCG (which would have featureless spectra) or 1< z <2 lensed systems with a weak absorption line spectrum. Based on our current spectroscopy, we estimate that at least ∼30% of the radial arc candidates are likely to be non-lensed features. If we assume that half of the inconclusive spectra are also contaminants, then the fraction would increase to ∼50%. The basic conclusions of this paper regarding the mean inner DM density slope are not sensitive to even a ∼50% decrease in the total number of radial arcs.

New redshifts were obtained for five tangential arc systems and are summarized in Table 4.1. One comment is warranted concerning the redshift of the southern arc in Abell 963. After considerable effort, an absorption line redshift (z=1.958) was finally obtained for this low surface brightness feature (H1 in Smith et al. 2005) using the blue arm of LRIS on Keck I. Another portion of the southern arc (H2) seems to have a similar spectrum but of lower S/N. The redshift and brightness of arc A1 in R0451 are interesting. At $z = 2.007$ and $F606W = 20.24 \pm 0.03$, this object is of similar brightness as the highly magnified Lyman break galaxy cB58.

4.3.5 Arc Statistics: A Summary

To summarize, using the archive of HST/WFPC2 galaxy clusters, we have visually identified candidate gravitationally lensed features, performed appropriate photometry, and measured the L/W ratios. The arc catalog is presented in the Appendix as Table 4.4, along with published redshifts where available (or if presented in this work).

As this is the first systematic search for *radial arcs*, we list *all* such features found in Table 4.4 and provide finding charts in Figure 4.9. The charts present the original HST image and a galaxy-subtracted version. In the case of the *tangential arcs*, since our subsequent analysis (§4 and §5) will focus only on those with $L/W > 7$, we only list those which either have a measured redshift or $L/W > 7$. Candidate arcs demonstrated spectroscopically to be foreground non-lensed sources are not included. However, where the spectroscopy is inconclusive, the candidates are retained. Offsets from the brightest cluster galaxy are provided in Table 4.4 to aid in their identification.

As discussed in §4, our statistical analysis will be based on both radial and tangential arcs with $L/W > 7$. In the total cluster sample we have found 12 radial arc candidates and 104 tangential arc candidates out of a total sample of 128 galaxy clusters. In Table 4.2 we summarize the arc statistics for both the total sample and those subsamples introduced in §2.1. The 68% confidence range for the radial to tangential number ratio was computed using binomial statistics, appropriate for small number event ratios (Gehrels, 1986). It is reassuring that the total sample and subsamples give similar results for this ratio, since this implies that the heterogeneous selection of clusters inherent in our analysis of the archival data is unlikely to be a dominant uncertainty.

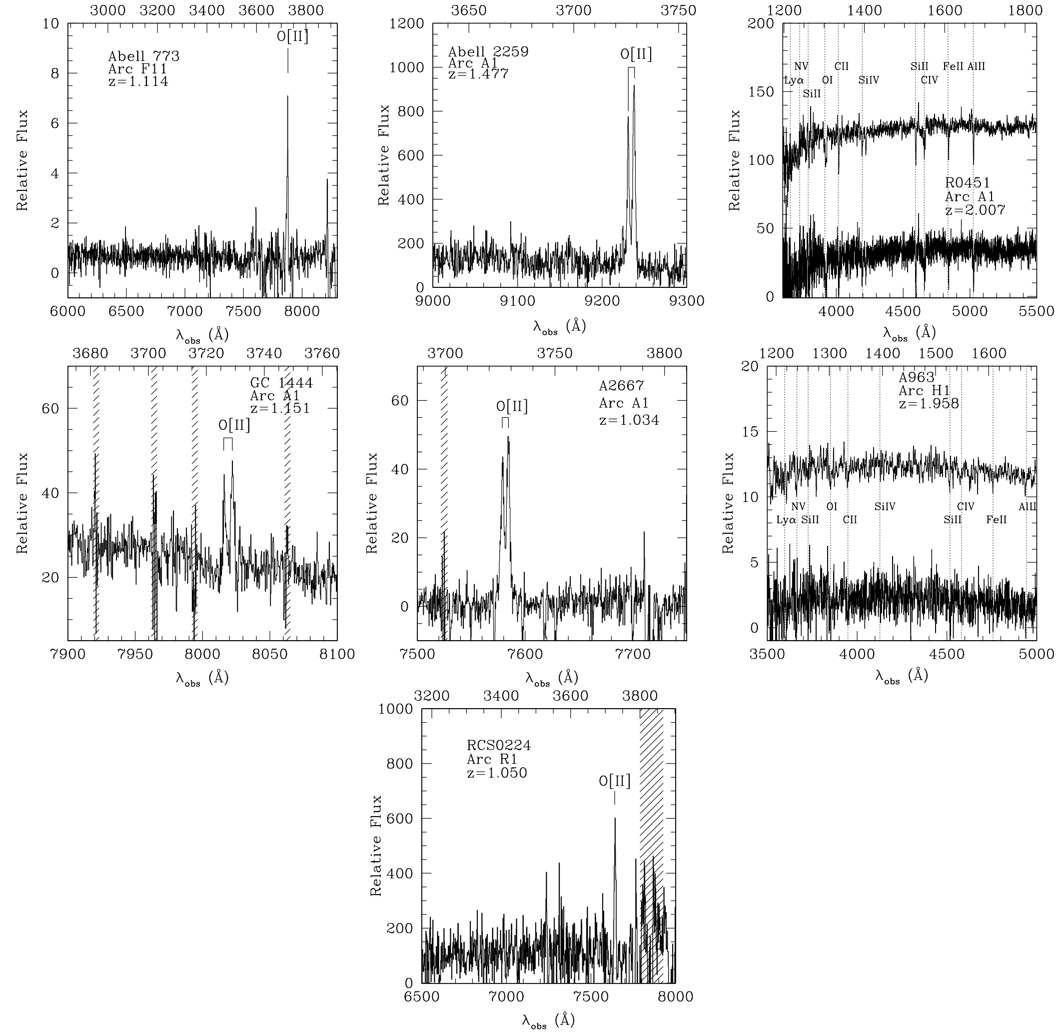

Figure 4.3: New gravitational arc redshift measurements. The new radial arc redshifts are in GC1444 and R0451. A smoothed version of the arc spectrums in Abell 963 and R0451 are also pesented so that the weak absorption features can be more readily discerned.

Table 4.2: Summary of Giant Arcs with $L/W > 7$

Cluster Sample	No. of Clusters	Tangential	Radial	Ratio R/T	68% Confidence Range
Edge	44	15	4	0.27	0.13-0.53
Smith	10	38	1	0.03	0.005-0.09
EMSS	12	13	2	0.15	0.05-0.40
Total	128	104	12	0.12	0.08-0.16

4.4 Deriving Mass Distributions from Arc Statistics

In this section we discuss our methodology for calculating the expected number ratio of radial to tangential arcs, which is based on the precepts developed by O02 (§4.1). We will include the effect of the finite source size of the radial arc sources into our calculation, confirming that this is a significant contributor to the radial arc cross section which ultimately affects the deduced inner DM slope. We introduce our mass model in §4.2 and show further that the effects of a central BCG are also significant. In §4.3 we summarize those systematics that have been studied in previous analyses. Finally, in §4.4 we show how we use the arc cross sections to deduce the number ratio of radial to tangential arcs. Utilizing the tools presented in this section, we will place constraints on the inner DM profile in §5.

4.4.1 Methodology

We follow the prescription presented by O02 for calculating the expected number ratio of radial to tangential arcs. The lens equation is given by (e.g. Schneider et al. 1992)

$$y = x - \alpha(x) = x - \frac{m(x)}{x} \tag{4.1}$$

where y and x are scaled radii in the source and lens plane, respectively. Throughout this work, we choose the generalized-NFW scale radius, r_{sc}, as our scaling radius, meaning that $x = R/r_{sc}$ and $y = \eta D_l/(r_{sc}D_s)$. The deflection angle, α, is determined by the mass distribution of the lens where the quantity $m(x)$ is defined by

$$m(x) = 2\int_0^x dy\kappa(y)y \tag{4.2}$$

The quantity $m(x)$ is proportional to the mass inside projected radius x, and $\kappa(x)$ is the surface mass density scaled by the critical surface mass density, Σ_{cr},

$$\kappa(R) = \frac{\Sigma_{tot}(R)}{\Sigma_{cr}} \tag{4.3}$$

where

$$\Sigma_{cr} = \frac{c^2}{4\pi G}\frac{D_s}{D_l D_{ls}} \tag{4.4}$$

and D_l, D_{ls}, and D_s are the angular diameter distance to the lens, between the lens and source and to the source, respectively.

With these definitions, the two eigenvalues of the Jacobian mapping between the source and image plane can be written as

$$\lambda_r = 1 - \frac{d}{dx}\frac{m(x)}{x}, \lambda_t = 1 - \frac{m(x)}{x^2} \tag{4.5}$$

The root of these two equations describes the radial and tangential critical curves of the lens. Since the magnification of the source is equal to the inverse of the determinant of the Jacobian, the radial and tangential critical curves define regions where the magnification of the source formally diverges. For a simple spherical lens, an infinitesimal source at x in the image plane is stretched by a factor $\mu_t = 1/\lambda_t$ in the tangential direction and $\mu_r = 1/\lambda_r$ in the radial direction. For an infinitesimal source, the cross section for either a radial or tangential arc is then simply the area in the source plane where

$$R(x) = \left|\frac{\mu_r(x)}{\mu_t(x)}\right| \geq \epsilon \tag{4.6}$$

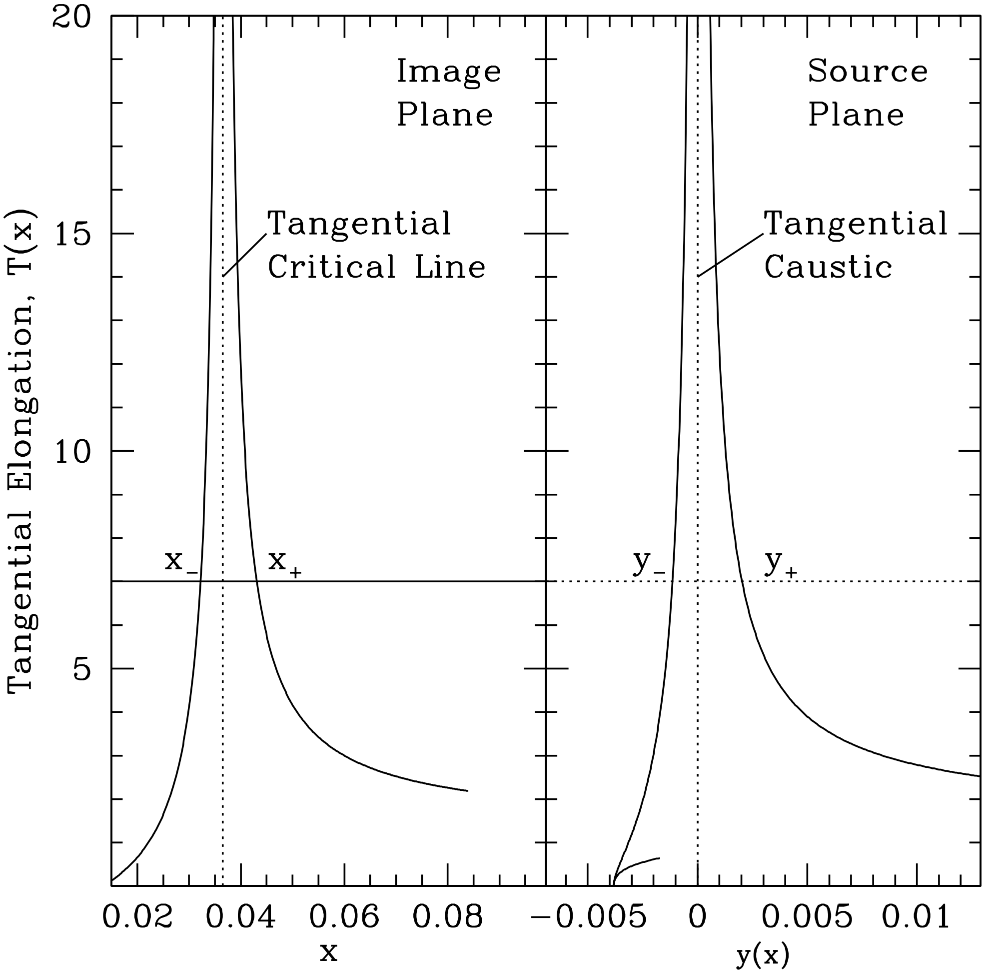

Figure 4.4: An illustration of how the tangential arc cross section is found with a $1.0 \times 10^{15} M_\odot$ NFW ($\beta = 1.0$) profile at z=0.3 with a background at z=1.0. The x and y positions corresponding to a tangentially oriented axis ratio (L/W) greater than 7. The value of y_- or y_+ with the largest absolute value is used in Eqn. 4.8 for calculating the cross-section.

$$T(x) = \left|\frac{\mu_t(x)}{\mu_r(x)}\right| \geq \epsilon \tag{4.7}$$

with ϵ being the minimum arc axis ratio to be considered. O02 demonstrates that only for $\epsilon \geq 7$ is the ratio of radial to tangential arcs relatively robust with respect to systematic uncertainties such as source and lens ellipticity (see § 4.4.3). Even then, the finite source size of radial arcs must be taken into account. Throughout this work we will only consider situations in which $\epsilon \geq 7$, corresponding to $L/W \geq 7$.

As in O02, we first take the source size to be small for typical tangential arcs and so use Equation 4.7 directly (see e.g. Hattori, Watanabe, & Yamashita 1997 for justification and Figure 5; left panel of O02). Then the cross section for tangential arcs is

$$\sigma_{tan} = \pi \left(\frac{r_{sc} D_S}{D_L}\right)^2 (max(|y_{t,+}|, |y_{t,-}|))^2, \tag{4.8}$$

where $y_{t,+}$ and $y_{t,-}$ correspond to the position on either side of the tangential caustic which satisfies Equation 4.7. Figure 4.4 illustrates the situation.

We now consider the effect of the finite source size for the radial arc sources. Useful diagrams for illustrating the relevant geometry are provided in Figures 1 and 2 of O02, and we will adopt the nomenclature and procedure of that work. We assume that the sources are circular with a finite radius, and consider situations where the source touches, crosses, or lies within the radial caustic. Figure 4.5 illustrates the dramatic effect that the finite source size can have on the radial arc cross section.

To allow for this important effect, we require the true (unlensed) size distribution of a representative sample of $z \simeq$1-1.5 galaxies typical of those being lensed by our clusters. Fortunately, a $z \sim$1.4 size distribution has been presented by Ferguson et al. (2004) based on the GOODS survey (see Figure 2; top panel, of that work), and we will adopt this for the remainder of our analysis. Galaxy sizes in this redshift bin were found to have half-light radii (which we will take as the

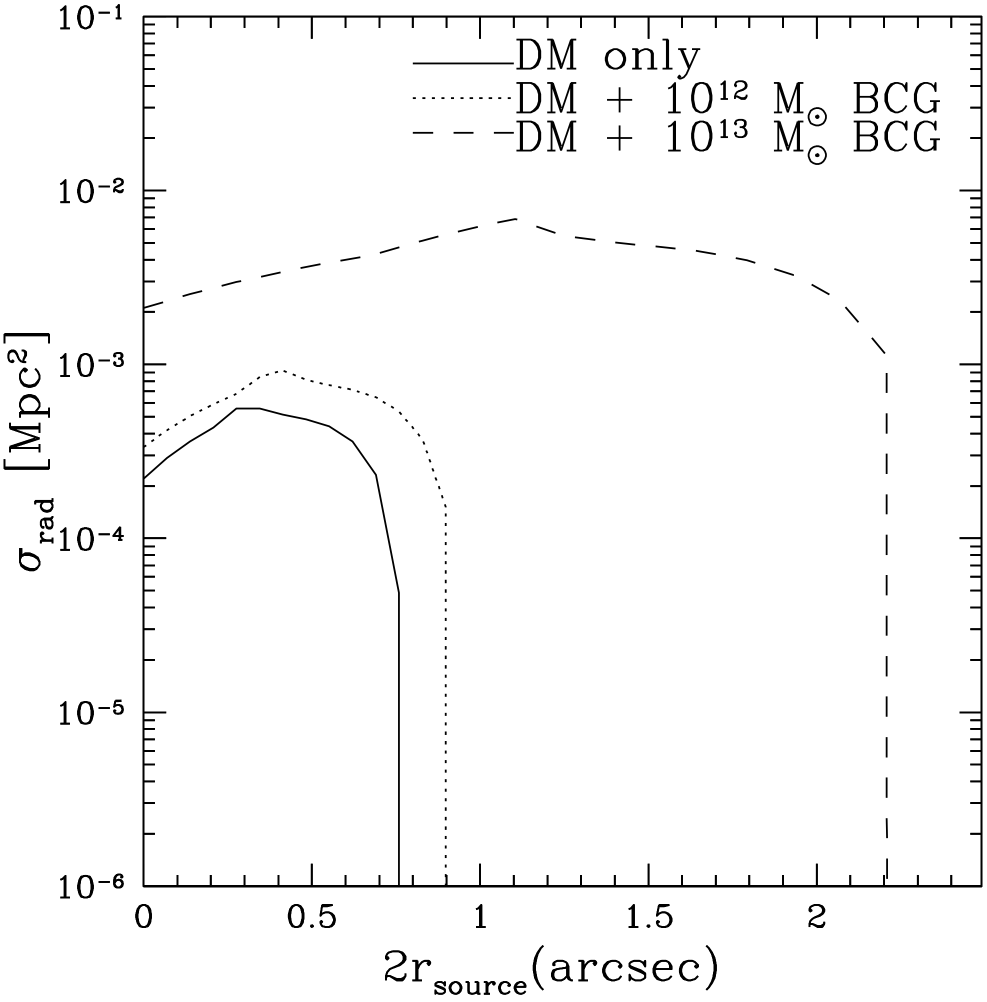

Figure 4.5: The radial arc cross section as a function of source size. Shown are models with $1.0 \times 10^{15} M_{\odot}$ in DM with profile slopes β=1.5 and various reasonable BCG masses included. The lens redshift is at $z = 0.2$ and the background redshift is at $z = 1.4$. See § 4.4.2 for a description of the mass models used. Given the strong radial arc cross section dependence, we adopt the z∼1.4 size distribution of Ferguson et al. (2004) taken from the GOODS fields.

radius of our sources) between ~0.″2 and ~1.″1 with the peak of the distribution at ~0.″7. We shall show later that the arc number ratio is relatively insensitive to source redshift, making this redshift bin choice unimportant (although it does roughly correspond to that observed for typical arcs in our sample).

4.4.2 Mass Models

For the density profiles of our clusters we will adopt a simple, spherically symmetric two-component mass model. The simplicity of this model is justified by O02, who showed that the number ratio is a relatively robust quantity with respect to ellipticities in the cluster mass distribution (see § 4.4.3).

The adopted model comprises the DM halo of the galaxy cluster (as represented by the gNFW profile) and a luminous baryonic component, representing the central cluster galaxy. Previous work on constraining the inner DM slope β through the number ratio of arcs neglected the possibly important contribution of the BCG luminous component or concluded that the effects are small (Molikawa & Hattori, 2001). Given that most of the radial arcs found in our sample are buried in the halos of a bright, centrally located galaxy (or a compact group of galaxies), it seems appropriate to revisit this assumption. For example, it has been shown numerically and theoretically (Meneghetti et al., 2003a) that the central cluster galaxy can increase the cross section for radial gravitational arcs significantly, especially if the underlying DM halo slope is shallow.

Dark Component

The cluster DM halo is modeled as

$$\rho_d(r) = \frac{\rho_c(z)\delta_c}{(r/r_{sc})^{\beta}\left[1+(r/r_{sc})\right]^{3-\beta}} \tag{4.9}$$

which represents a generalization of the numerically-simulated CDM halos, where ρ_c is the critical density and δ_c is a scaling factor. This density profile asymptotes to $\rho \propto r^{-\beta}$ at $r \ll r_{sc}$ and $\rho \propto r^{-3}$ at $r \gg r_{sc}$. For values of $\beta = 1, 1.5$, the

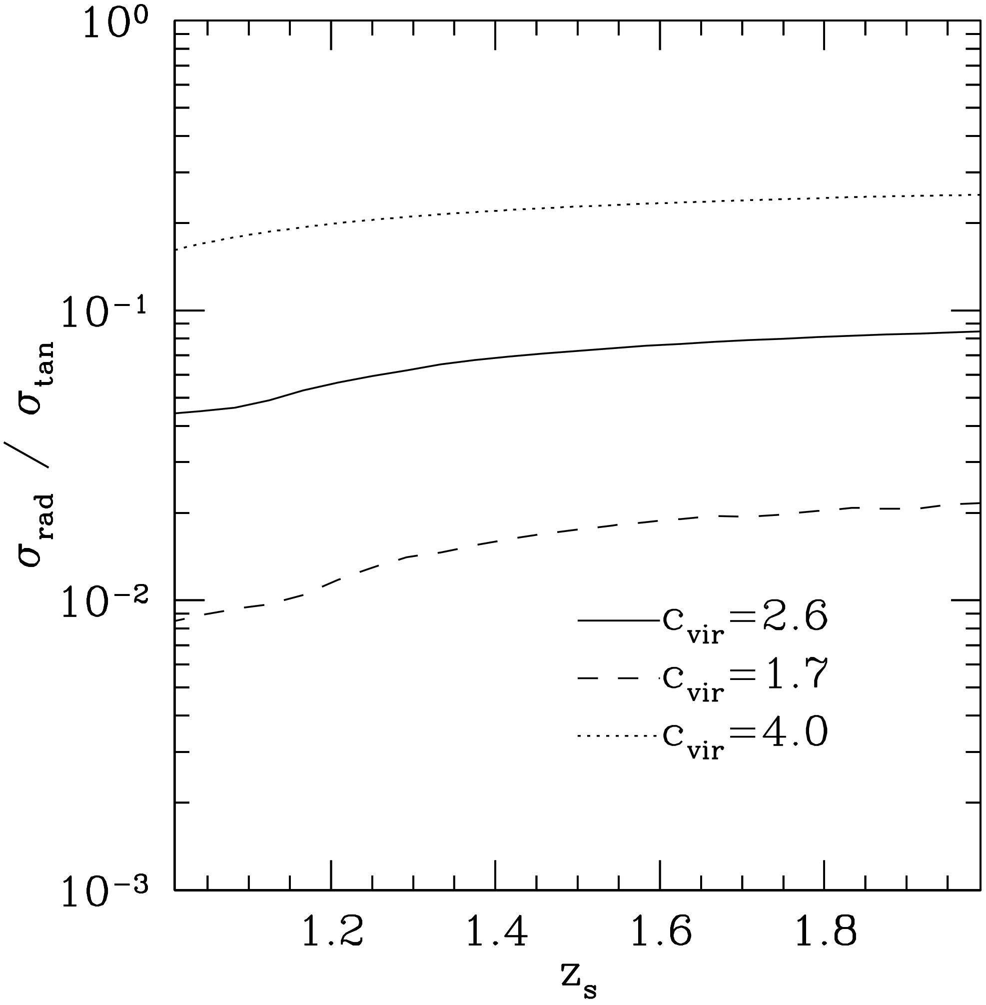

Figure 4.6: The radial to tangential cross section ratio as a function of background source redshift while varying the concentration parameter of the DM halo by ±1-σ as prescribed by Bullock et al. (2001). Shown are models with $1.0 \times 10^{15} M_\odot$ in DM with β=1.5 at a lens redshift $z = 0.2$. The assumed radial arc source size distribution is that found by Ferguson et al. Note that the cross section ratio is relatively constant as a function of background source redshift.

DM density profile is identical to that found by NFW and nearly identical to that of Moore et al. (1998), respectively. Using this general form for the DM halo allows for comparison to earlier numerical results, although the latest generation of DM halo simulations indicates that the DM profile may not converge to a simple asymptotic slope (e.g. Power et al. 2003; Tasitsiomi et al. 2004). Basic lensing relations for the gNFW form have been presented elsewhere (e.g. Wyithe et al. 2001).

The profile of the DM halo is characterized further by the concentration parameter, c_{vir}. In this work we follow O02 and Oguri et al. (2001) in determining the critical parameters of the mean DM halo for a given mass. Following Bullock et al. (2001) in characterizing the median and scatter in concentration parameters for a given mass, we use

$$c_{vir} = \frac{r_{vir}}{r_{sc}}, \tag{4.10}$$

$$c_{vir} = (2-\beta)c_{-2}, \tag{4.11}$$

where

$$c_{-2} = \frac{8}{1+z_{lens}}\left(\frac{M_{vir}}{10^{14}h^{-1}M_{\odot}}\right)^{-0.13}, \tag{4.12}$$

where the factor of $(2-\beta)$ generalizes the situation to $\beta \neq 1$ (Keeton & Madau, 2001). From this relation, it is possible to calculate both r_{sc} and δ_c for a typical halo of a given mass and inner DM density slope.

As Bullock et al. and others have found, there is significant scatter around the median value of the concentration parameter. Taking Equation 4.12 and using the Bullock et al. 1-σ dispersion around the median value of the concentration parameter

$$\Delta(log c_{-2}) = 0.18 \tag{4.13}$$

we have investigated the effect of a varying value of c_{vir} (Figure 4.6). As can

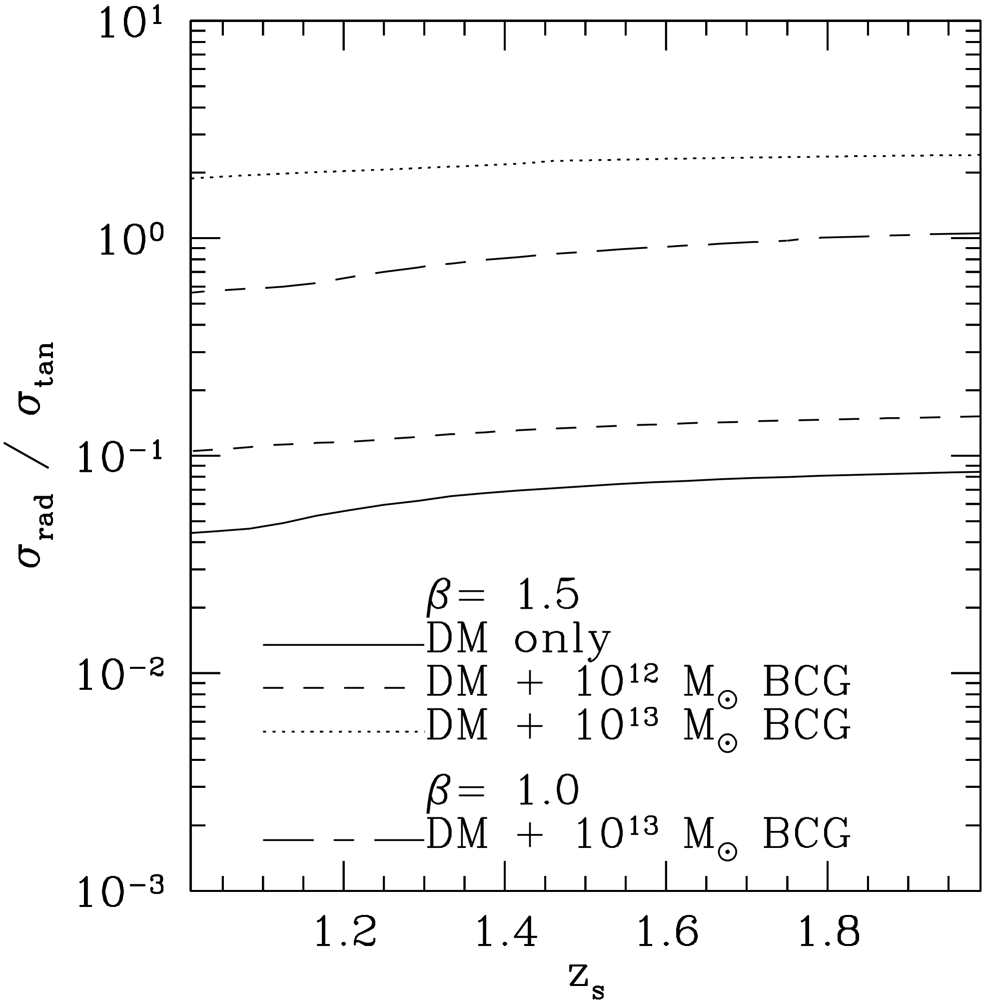

Figure 4.7: The radial to tangential arc cross section ratio as a function of background source redshift while varying the BCG mass and inner slope of the DM profile. The assumed radial arc source size distribution is that found by Ferguson et al. which we assumed stays constant throughout the relevant source redshift range. Shown are models with $1.0 \times 10^{15} M_\odot$ in DM at a lens redshift $z = 0.2$. Note that the β=1.0 and β=1.5 models with a $10^{13} M_\odot$ BCG have expected arc number ratios within a factor of few of each other.

be seen, the arc cross section ratio can vary by an order of magnitude between low and high concentration halos of the same mass and inner slope. For this reason, the dispersion in halo concentrations will be taken into account when we present our results in §5. It is important to note that the cross section ratio across concentrations is relatively constant as a function of source redshift (see § 4.4.4).

Luminous Component

Nearly all of the radial arc candidates discovered in our HST search were either buried in the halo of a central BCG or that of a compact multi-galaxy core. It thus seems reasonable to include a luminous baryonic mass component in our model. We used a Hernquist (1990) mass density profile

$$\rho_H(r) = \frac{M_L r_H}{2\pi r (r_H + r)^3} \tag{4.14}$$

with total mass M_L and $R_e = 1.8153 r_H$. The Hernquist luminous density distribution is found to be a good representation of actual BCGs (see e.g. Sand et al. 2004). Throughout this work we choose R_e=25 kpc which is a typical BCG effective radius (e.g. Gonzalez et al. 2005).

Figure 4.7 illustrates the significant effect that adding a massive central galaxy can have on the arc ratio. A major degeneracy can be seen. The expected cross section ratio is similar for both a β=1.0 and β=1.5 DM halo if a $10^{13} M_\odot$ BCG is inserted. Note again that the arc cross section ratio is a relatively constant function of the background redshift for a given mass model. We also experimented with different values for the BCG effective radius (15< R_e <45 kpc) and found that the resulting number ratio varies by a factor of ∼5. Clearly the more precise the information on the mass of the BCG, the more useful will be the constraints on the DM profile.

4.4.3 Summary of Systematic Effects

Here we summarize the model assumptions which affect our subsequent analysis. The most thorough earlier investigation was by O02. Oguri considered the effect of finite source size, lens ellipticity, and mass dependence of the cluster lens.

The finite source size greatly affects the radial arc cross-section and O02 introduced an analytic formalism to correct for this. This analytic formalism reproduces well the expectation from numerical simulations and is used throughout this work. The tangential arc cross section, on the other hand, changes relatively little as a function of finite source size, particularly for the $L/W > 7$ condition considered here (e.g. O02; Figure 5). Accordingly, no correction was made.

Lens ellipticity primarily changes the *absolute* number of arcs (see also Bartelmann et al. 1998). For a minimum axis ratio of $L/W=7$, the arc ratio changes only by a factor of order unity. Likewise, while changing the mass of the galaxy cluster has large consequences for the absolute number of arcs expected, the effect on the ratio of radial to tangential arcs for our minimum axial ratio is also small.

It is for these reasons that the arc ratio is an attractive statistic. No prior knowledge of the cluster mass is necessary and relatively heterogeneous samples (such as the current HST sample) may be used to find the average density profile.

Keeton (2001) studied the effect of source ellipticity on the number ratio of arcs. The basic conclusion of this work was that the ratio of radial to tangential arcs decreases with increasing source ellipticity. The size of the effect is a factor of order unity. For the purposes of the present paper where we are applying the arc number ratio test on the first observational sample of radial arcs, we will not consider the effects of source ellipticity.

4.4.4 The Arc Number Ratio

Thus far we have presented predictions in terms of the ratio of arc *cross sections*. We now take the final step towards a comparison with the observations by determining the number ratio. To do this, for a given mass, inner DM slope, con-

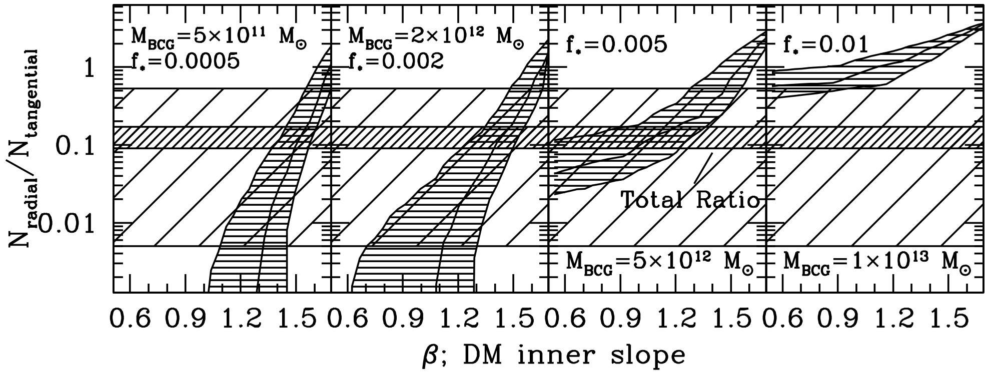

Figure 4.8: Constraints on the inner DM profile, β, as a function of the BCG mass (or BCG mass fraction, f_*, see text for details). The narrow and wider hashed horizontal bars represent respectively 68% confidence limits on the observed arc number ratio for the total sample and the range in such limits for the individual cluster sub-samples. The other band represents the range of theoretical predictions if the concentration parameter is changed by $\pm 1-\sigma$ for our fiducial cluster model. The left two panels span the BCG mass range found in the detailed analysis of Sand et al. (2004). Virtually no constraint on β is found if the typical BCG mass is higher than $5 \times 10^{12} M_\odot$ ($f_* = 0.005$).

centration parameter, and redshift, it is necessary to integrate the product of the cross section and the number density of galaxies over some range in background (source) redshift.

Since the arc cross section ratio is largely independent of source redshift (see Figures 4.6 and 4.7), the expected number ratio of radial to tangential arcs should be well-represented by the ratio of their cross sections, for a given halo model. Moreover, the ratio is also fairly insensitive to the mass of the underlying galaxy cluster. Therefore, with a single reasonable fiducial model of fixed mass, lens redshift,and source redshift we can obtain constraints on the DM inner slope for the average galaxy cluster in our sample.

It is not clear whether magnification bias will be significant in our survey.

Our visually-based search method is not likely to be flux-limited; it is largely the persistence of a relatively high contiguous surface brightness signal that is noticed by a human searcher. As lensing conserves surface brightness, our arc search should not be unduly affected by magnification bias. Miralda-Escude (1993) discusses the possible magnification bias in arc searches and notes these may be significant in data affected by ground-based seeing. Given the improved point spread function of HST, it seems safe to conclude that our search for resolved arcs is effectively surface brightness limited.

4.5 Results

In this section we compare the observed arc number ratio with theoretical predictions based on the methodology presented in § 4.4 and derive the first statistical constraints on the inner slope β of the DM distribution. We discuss the remaining sources of observational error and review the prospects for reducing their effect.

4.5.1 Constraints on the Inner DM Slope and the Role of the BCG

Taking the formalism presented in §4.4, we now calculate the expected number ratio of radial to tangential arcs as a function of the DM inner slope, β, for a two-component mass model. We assume a fiducial model representing the typical galaxy cluster in our sample with M_{DM}=$1\times10^{15}M_{\odot}$ at z_{lens}=0.2 and a background at z_{source}=1.4. As discussed, we used the background size distribution from Ferguson et al. in order to calculate the radial arc cross section. We re-evaluate the concentration parameter c_{vir}, according to Equations 4.11 and 4.12 at each value of β.

We present our constraints on the inner DM slope, β, in Figure 4.8. The two horizontal hatched bands represent two estimates of the uncertainty in our measured radial to tangential arc number ratio. The inner, tightly hatched band represents the 68% confidence limit on the ratio across the total, heterogenous, archival sample. The outer horizontal band represents the maximum range of the 68% confidence regions amongst the cluster subsamples presented in § 4.2.1 (see Table 4.2). Although this enlarged region may not take into account possible systematics associated with identifying arcs in each sub-sample, it probably gives a reasonably cautious upper limit on the uncertainties in the number ratio. The other, diagonally oriented band (with horizontal hatches) in each panel shows the predicted values of the number ratio for our fiducial cluster, taking into account the expected 1-σ dispersion of the concentration parameter according to Equation 4.13, given different BCG masses.

The various panels in Figure 4.8 represent different assumed values for the mean stellar mass of the BCG, recognizing that this is a key variable. The left two panels span the range of stellar masses ($5\times10^{11} < M_{\odot} < 2\times10^{12}$) derived by quantitative dynamical and photometric analysis in the sample studied by Sand et al. (2004). The two right-most panels represent more extreme stellar masses, the third ($5\times10^{12}M_{\odot}$) being within the likely range, and the fourth ($1\times10^{13}M_{\odot}$) somewhat extreme. Also noted in the panels of Figure 4.8 is the BCG to DM mass fraction, f_{*}, which is an alternative way to parameterize the importance of the BCG for calculating the arc number ratio.

Depending on the mean BCG stellar mass, very different conclusions can be drawn about the DM profile. If the Sand et al. (2004) sample is representative of the archive sample discussed here, the constraints on the inner DM slope are reasonably tight with $1.2 \lesssim \beta \lesssim 1.6$ for the total sample (and $0.7 \lesssim \beta \lesssim 1.7$ for the range spanned by the individual subsamples). In this case, it would be reasonable to conclude the sample is consistent with both NFW and the Moore profiles given the uncertainties. However, if typical BCG masses are as high as $5\times10^{12}M_{\odot}$, we can only constrain the dark matter density profile to have $\beta \lesssim 1.3$ (1.6 for the subsamples). If the mean BCG mass were as as high as $10^{13}M_{sol}$, then no acceptable solutions would be found unless the true ratio of radial to tangential arcs was at the upper end of the range of observed values.

Even if precise stellar masses for each BCG were available, it is important to probe the sensitivity to the *cluster* properties. We thus explored the effect on β of changing the fiducial cluster model, namely one with M_{DM}=$1\times10^{15}M_\odot$ at z_{lens}=0.2. In fact, reducing the cluster mass to M_{DM}=$5\times10^{14}M_\odot$ or changing the redshift to z_{lens}=0.5 produces only a marginal change in the acceptable values of β, illustrating again that the arc number ratio is a robust tool if the BCG parameters can be constrained.

4.5.2 Additional Uncertainties and Sample Selection Effects

Of the uncertainties discussed earlier, those relating to the identification and characterization of the *radial arcs* through galaxy subtraction would lead to an *underestimate* of their true number (and hence the radial to tangential number ratio), while contamination from non-lensed radially oriented objects would work in the opposite direction. Remarkably, the total number of radial arcs would need to change by nearly an order of magnitude for our conclusions on β to be significantly altered. This, we believe, is highly unlikely given the tests we have performed.

For the *tangential arcs*, contamination may arise from chance alignment of elongated foreground objects or tidal debris associated with galaxies merging with the BCG. Spectroscopic identification of a large sample of arcs would be necessary to understand this contamination rate in detail. However, none of the tangential arcs identified in *HST* imaging and targeted in our Keck spectoscopic program have turned out to be spurious. It seems safe to conclude that the contamination rate is very low. As mentioned in § 4.3.1, the tangential arcs found independently by two of the authors disagreed only at the $\sim$10% level, providing an estimate of the noise associated with visual identifications.

A further uncertainty related to our mass modeling technique is that arising from cluster substructure. In common with previous studies, the modeling framework presented in §4.4 assumes that clusters comprise a single central DM halo spatially coincident with the BCG. However, Smith et al. (2005) show that 70% of X–ray luminous cores in their sample (Table 3) are unrelaxed with $\sim$20–60% of the mass in structures not spatially coincident with the BCG.

We explore the implications of possible substructure using the Smith sample. Interestingly, the radial to tangential arc ratio in the Smith sample is lower than for the other cluster samples which may arise from the substructure issues noted above. To improve the statistics, we also considered the larger Edge sample which was selected to be dominated by relaxed systems (Edge, private communication, see § 4.2.1). Contrasting the Edge (predominantly relaxed) and Smith (predominantly unrelaxed) samples, we find the ratio $r_{EDGE}= 0.27^{+0.26}_{-0.14}$ and $r_{SMITH}= 0.03^{+0.06}_{-0.025}$, differing at the $\sim$2–σ level.

Conceivably, r_{SMITH} is depressed relative to r_{EDGE} by the substructure present in the Smith clusters. This idea is supported by numerical simulations (Jing, 2001) which show that DM halos in equilibrium (relaxed) have higher typical concentrations than DM halos out of equilibrium (unrelaxed). If true, this would naturally explain the different arc ratios seen in the Smith and Edge samples, since higher concentration halos yield higher arc number ratios (see Figure 4.6). In this respect, the scatter between the subsamples, as indicated in Figure 4.8, may be a reasonable measure of the effects of substructure.

This can also be understood in terms of lensing cross-sections (see similar argument in Molikawa & Hattori 2001). Introducing irregularities (substructure) into a cluster mass distribution generally increases the shear, γ. Because the tangential critical line forms where $1-\kappa-\gamma = 0$, increasing γ pushes the tangential arcs towards regions with lower κ, i.e. further from the center of the cluster, and thus the cross-section to tangential arc formation increases. The effect works in the opposite sense for radial arcs, which form where $1 - \kappa + \gamma = 0$. Additional shear shifts radial arcs toward regions with higher κ, i.e. closer to the center of the cluster and thus reduces the cross-section to radial arc formation. Therefore, clusters with significant substructure are expected to display a lower arc number ratio than clusters that are more axisymmetric with little substructure.

It will be important to quantify this effect more rigorously in future experiments that combine BCG mass estimates with arc number ratio measurements. A key aspect of such work would be to study a large, well–defined sample of clusters (of order ∼100) for which both homogeneous *HST* data and reliable cluster substructure diagnostics are available.

4.6 Summary and Prospects

In this work we have undertaken a systematic search for gravitational arcs in the HST/WFPC2 cluster archive. Because we digitally subtracted bright cluster galaxies, this is the first arc survey which is sensitive to radial gravitational arcs. Using this unique data set, we have attempted to place constraints on the inner DM density slope, β, for this sample of clusters.

The main results of the paper can be summarized as follows:

1. A careful search of the 128 galaxy clusters reveals 12 radial and 104 tangential arc candidates with a length-width ratio $L/W > 7$.

2. Taking the entire sample of galaxy clusters, we have constructed 3 smaller subsamples: two based on X-ray properties and one with a roughly uniform optical imaging depth. The arc number ratio is roughly consistent across all three samples and confirms the hypothesis that the radial to tangential arc number ratio is a relatively robust statistic with respect to intrinsic cluster properties.

3. Employing an analysis similar to that of O02, but with the important addition of a BCG mass component, we have found that the observed arc number ratio is consistent with a wide range of DM inner slopes ($\beta < 1.6$), depending on the assumed BCG mass.

The archive sample presented in this paper has illustrated a potentially powerful method of constraining the profile of dark matter in clusters. Although statistical in nature, as with all gravitational lensing techniques, some assumptions are necessary. We have argued that the *ratio* of the abundance of radial and tangential arcs minimizes many of these leaving the mass of the baryon-dominated BCG, cluster substructure and sample uniformity as the key issues. All of these are, in principle, tractable problems given sufficient data. We thus remain optimistic that a valuable constraint on the distribution of DM slopes can be derived via the methods described in this paper given adequate observational effort.

4.7 Appendix

4.7.1 The Cluster Catalog

Here we present our HST/WFPC2 cluster catalog used to identify gravitational arcs. The criteria for being included in the sample are detailed in § 4.2. For each cluster entry, the redshift, RA & DEC, exposure time, filter, and X-ray luminosity are listed. If the cluster is associated with one of the three cluster subsamples present in § 4.2.1, it is noted as well. A cluster is flagged if it has an associated arc which is presented in Table 4.4. The cluster RA & DEC are taken from the HST world coordinate system directly at approximately the position of the BCG.

4.7.2 The Arc Catalog

Here we present the gravitational arc catalog derived from Table 4.3. For each arc, the redshift (if available), magnitude, filter, length to width ratio, and offset from the BCG are presented. Also noted is whether or not the arc is radial or tangential. For the tangential arcs, only those with a $L/W > 7$ are listed, unless they have a spectroscopic redshift. For the radial arcs, all candidates are listed without regard to their L/W value. Note that only those arcs with a $L/W > 7$ are included in the analysis presented in § 4.5. If possible, the arc nomenclature from previous work has been adopted. Otherwise, an arc is labeled with the prefix 'A' followed by a sequential number. Those arcs whose photometry and measured L/W have possibly been affected by poor galaxy subtraction are flagged (see discussion in § 4.3.2 and 4.3.3).

4.7.3 Radial Arc Finding Charts

Here we present finding charts for all clusters with candidate radial arcs, whether or not the arc has a $L/W > 7$. For each chart, the left panel is of the original image, while the right panel is the BCG-subtracted image from which the radial arc was identified, along with a label corresponding to that presented in Table 4.4. Note that for Cl0024 and A1689, no bright galaxies were removed in the finding chart. Two finding charts are presented for MS0451 since one of the radial arcs (A6) is associated with a bright elliptical away from the cluster center. No finding charts were made of tangential arc candidates, although offsets from the BCG are listed in Table 4.4. North is up and east is always towards the left hand side of the page.

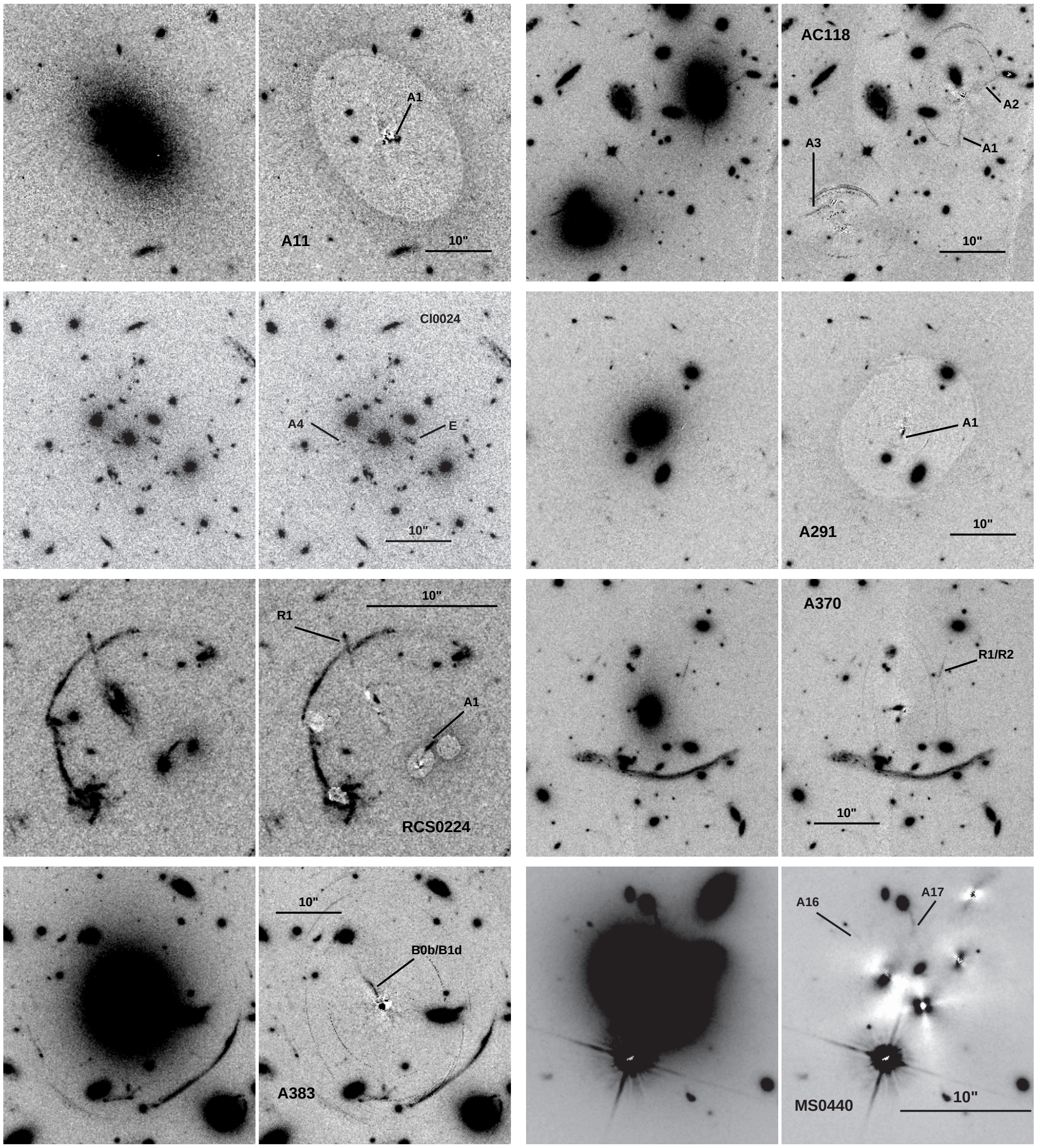

Figure 4.9: Radial arc finding charts

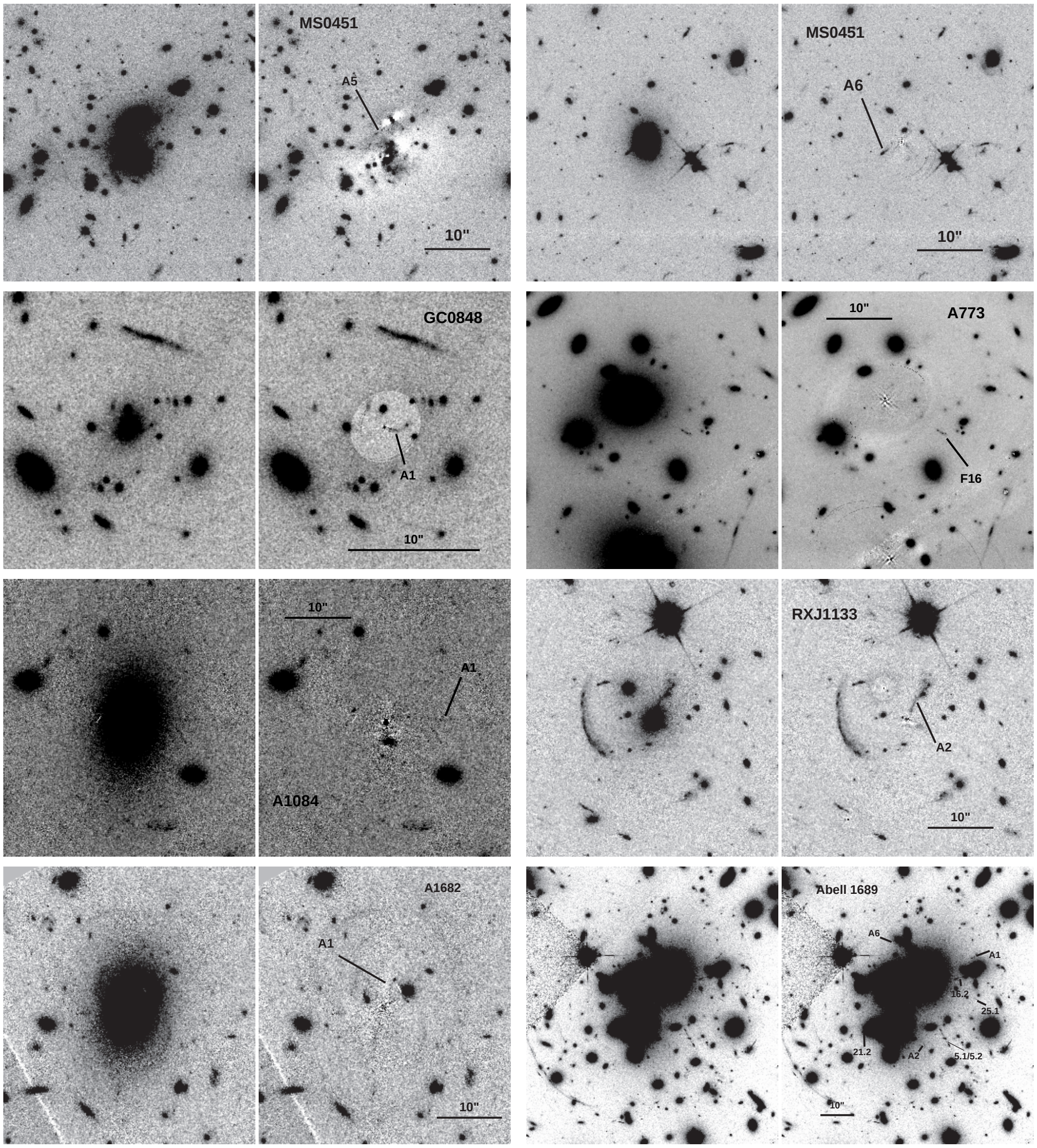
MS0451
A5
10"
MS0451
A6
10"
GC0848
A1
10"
10"
A773
F16
10"
A1
A1084
RXJ1133
A2
10"
A1682
A1
10"
Abell 1689
A6
A1
16.2
25.1
21.2
A2
5.1/5.2
10"

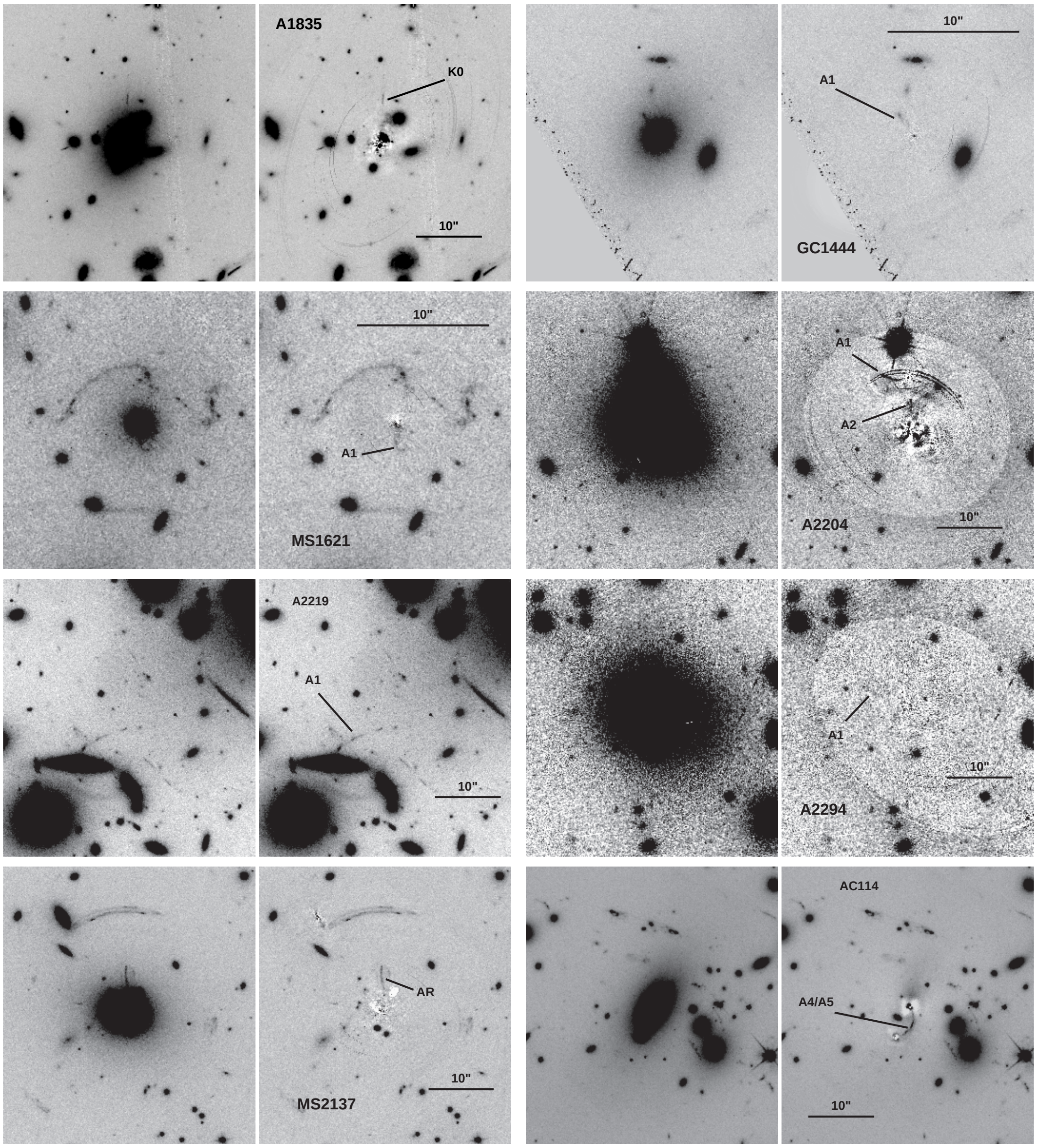
A1835
K0
10"
10"
A1
GC1444
10"
A1
MS1621
A1
A2
A2204
10"
A2219
A1
10"
A1
10"
A2294
AR
10"
MS2137
AC114
A4/A5
10"

Table 4.3: WFPC2 Cluster Catalog

Cluster	PID	z_{clus}	α (J2000.0)	δ (J2000.0)	Exp. time (ks)	Filter	Cluster Sample
$A11^{\dagger}$	8719	0.166	00 12 33.9	-16 28 06.9	0.8	606	1
$AC118^{\dagger}$	5701	0.308	00 14 20.6	-30 24 01.5	6.5	702	..
MS0016	5378	0.541	00 18 33.6	+16 26 16.0	12.6/16.8	555/814	3
$Cl0024^{\dagger\ddagger}$	5453	0.39	00 26 35.5	+17 09 50.7	23.4/19.8	450/814	..
$A68^{\ddagger}$	8249	0.255	00 37 06.8	+09 09 23.4	7.5	702	2
3c16	6675	0.405	00 37 45.4	+13 20 09.8	7.1	702	..
$GC0054^{\ddagger}$	5378	0.560	00 56 56.9	-27 40 29.6	12.6/16.8	555/814	..
PKS0101	6675	0.390	01 04 24.1	+02 39 43.4	7.5	702	..
$A209^{\ddagger}$	8249	0.206	01 31 52.6	-13 36 40.8	7.8	702	2
$A267^{\ddagger}$	8249	0.230	01 52 41.9	+01 00 25.9	7.5	702	2
$A291^{\dagger}$	8301	0.196	2 01 39.90	-02 11 39.7	0.8	606	1
GC0210	8131	0.270	02 10 26.0	-39 29 42.9	7.8	702	..
$5c6.124^{\ddagger}$	6675	0.448	02 16 40.9	+32 50 47.1	10.4	702	..
$RCS0224^{\dagger\ddagger}$	9135	0.77	02 24 30.82	-00 02 27.8	13.2/6.6	606/814	..
GC0231	6000	0.607	02 31 42.7	+00 48 41.0	15.3	606	..
$A370^{\dagger\ddagger}$	6003	0.375	02 39 53.1	-01 34 54.8	5.6	675	..
$A383^{\dagger\ddagger}$	8249	0.189	02 48 03.3	-03 31 44.4	7.5	702	2
GC030518	5991	0.42	03 05 18.1	+17 28 24.9	2.1/2.4	606/814	3
$GC03053^{\ddagger}$	5991	0.43	3 05 31.6	+17 10 03.1	2.1/2.4	606/814	3
GC0303	5378	0.420	03 06 19.0	+17 18 49.6	12.6	702	..
Cl0317	7293	0.583	03 20 00.8	+15 31 50.1	2.6/2.5	555/814	..
GC0329	8131	0.45	03 29 02.8	+02 56 23.3	10.4	702	..
GC0337	7374	0.59	03 37 45.1	-25 22 35.8	11.0	702	..
GC0341	8131	0.44	03 41 59.1	-44 59 58.3	11.2	702	..
GC0412	5378	0.51	04 12 52.1	-65 50 48.5	12.6/14.7	555/814	..
$RXJ0439^{\ddagger}$	8719	0.245	04 39 00.5	+07 16 09.5	04.1	606	1
$MS0440^{\dagger\ddagger}$	5402	0.190	04 43 09.7	+02 10 19.5	22.2	702	3
$RXJ0451^{\ddagger}$	8719	0.430	04 51 54.6	+00 06 19.3	1.0	606	1

continued on next page

Table 4.3 – continued from previous page

Cluster	PID	z_{clus}	α (J2000.0)	δ (J2000.0)	Exp. time (ks)	Filter	Cluster Sample
$MS0451$†‡	5987	0.55	04 54 10.6	-03 00 50.7	10.4	702	3
GC0720	7374	0.268	07 20 17.8	+71 32 13.4	4.8	702	..
GC072056	8131	0.230	07 20 53.8	+71 08 59.3	5.2	702	..
A586	8301	0.170	07 32 20.3	+31 38 00.1	0.8	606	1
$PKS0745^{\ddagger}$	7337	0.103	07 47 31.3	-19 17 40.0	2.1/1.8	555/814	..
GC0818	8325	0.260	08 18 57.3	+56 54 24.5	7.2	702	..
GC0819	8325	0.226	08 19 18.3	+70 55 04.6	6.9	702	..
RXJ0821	8301	0.109	08 21 02.3	+07 51 47.3	0.6	606	1
A646	8301	0.127	08 22 09.6	+47 05 52.5	0.6	606	1
$4c+55^{\ddagger}$	8719	0.242	08 34 54.9	+55 34 21.3	1.0	606	1
GC0841+64	7374	0.342	08 41 07.6	+64 22 25.7	7.2	702	..
GC0841	8325	0.235	08 41 44.1	+70 46 53.2	6.9	702	..
$A697^{\ddagger}$	8301	0.282	08 42 57.6	+36 21 59.1	1.0	606	1
$GC0848^{\dagger}$	7374	0.570	08 48 48.0	+44 56 16.7	12.0	702	..
$GC0848N^{\ddagger}$	7374	0.543	08 48 49.3	+44 55 48.2	12.0	702	..
GC0849	8325	0.240	08 49 10.8	+37 31 08.1	7.8	702	..
Z2089	8301	0.235	09 00 36.8	+20 53 39.6	1.0	606	1
3c215	5988	0.411	09 06 31.8	+16 46 11.7	7.8/5.0	555/814	..
RXJ0911	8705	0.77	09 11 26.5	+05 50 14.5	12.5/12.5	606/814	..
IRAS0910	6443	0.442	09 13 45.5	+40 56 27.9	4.34	814	..
$A773^{\ddagger\dagger}$	8249	0.217	09 17 53.5	+51 44 1.0	7.2	702	2
A795	8301	0.136	09 24 05.3	+14 10 21.0	0.6	606	1
$3c220^{\ddagger}$	6778	0.620	09 32 40.1	+79 06 28.9	11.4/11.5	555/814	..
GC0939	5378	0.407	09 43 03.0	+46 56 33.3	4.0/6.3	555/814	..
GC0943	6581	0.70	09 43 42.7	+48 05 03.1	20.2	702	..
$A868^{\ddagger}$	8203	0.153	09 45 26.4	-08 39 06.6	4.4	606	..
Z2701	8301	0.215	09 52 49.1	+51 53 05.2	1.0	606	1
GC0952	6478	0.377	09 52 56.0	+43 55 28.8	7.0	555/814	..
GC0957	5979	0.390	10 01 20.9	+55 53 50.9	32.2/2.3	555/814	..
$A963^{\ddagger}$	8249	0.206	10 17 03.7	+39 02 49.2	7.8	702	2
A980	8719	0.158	10 22 28.4	+50 06 19.9	0.8	606	1

continued on next page

Table 4.3 – continued from previous page

Cluster	PID	z_{clus}	α	δ	Exp.	Filter	Cluster
			(J2000.0)	(J2000.0)	time (ks)		Sample
$Z3146^{\ddagger}$	8301	0.291	10 23 39.6	+04 11 10.8	1.0	606	1
A990	8301	0.142	10 23 39.9	+49 08 37.9	0.6	606	1
$Z3179^{\ddagger}$	8301	0.143	10 25 58.0	+12 41 07.5	0.6	606	1
A1033	8301	0.126	10 31 44.3	+35 02 29.0	0.6	606	1
A1068	8301	0.139	10 40 44.4	+39 57 10.9	0.6	606	1
$A1084^{\dagger}$	8301	0.133	10 44 32.9	-07 04 08.0	0.6	606	1
5c210	5988	0.478	10 52 36.1	+48 40 01.2	10.8/5.3	555/814	..
$A1201^{\ddagger}$	8719	0.151	11 12 54.5	+13 26 08.0	0.8	606	1
A1204	8301	0.171	11 13 20.5	+17 35 41.0	0.8	606	1
Z3916	8301	0.204	11 14 21.8	+58 23 19.8	1.0	606	1
A1246	8301	0.190	11 23 58.8	+21 28 46.2	0.8	606	1
$RXJ1133^{\dagger\ddagger}$	8719	0.394	11 33 13.2	+50 08 40.8	1.0	606	1
$MS1137^{\ddagger}$	6668/5987	0.782	11 40 22.3	+66 08 14.1	13.8/14.4	606/814	3
A1366	8719	0.116	11 44 36.9	+67 24 20.4	0.6	606	1
A1423	8719	0.213	11 57 17.3	+33 36 40.1	1.0	606	1
GC1205	8131	0.35	12 05 51.3	+44 29 08.9	7.8	702	..
Z5247	8719	0.229	12 34 17.6	09 45 58.6	1.0	606	1
GC1256	8131	0.232	12 56 02.3	+25 56 36.7	4.4	702	..
5c12.251	6675	0.312	13 05 51.7	+36 39 27.3	5.0	702	..
$A1682^{\dagger\ddagger}$	8719	0.221	13 06 45.8	+46 33 30.4	1.0	606	1
3c281	5988	0.600	13 07 54.0	+06 42 14.5	9.6/7.6	606/814	..
GC1309	8325	0.290	13 09 56.2	+32 22 13.0	7.8	702	..
$A1689^{\ddagger\dagger}$	6004	0.183	13 11 29.4	-01 20 28.7	44.2/6.0	555/814	..
GHO1322	6278	0.755	13 24 47.2	+30 59 00.1	15.8/15.8	606/814	..
GC1322	5234	0.571	13 24 48.9	30 11 39.3	8.0/16.0	606/814	..
GC1335	8131	0.382	13 34 57.6	+37 50 29.9	7.8	702	..
$A1763^{\ddagger}$	8249	0.223	13 35 20.2	+41 00 04.6	7.8	702	2
GC1347	8131	0.470	13 48 00.9	+07 52 23.7	10.4	702	..
$MS1358^{\ddagger}$	5989	0.33	13 59 50.5	+62 31 06.8	3.6	606/814	3
$A1835^{\ddagger\dagger}$	8249	0.253	14 01 02.1	+02 52 42.3	7.5	702	2
GC1409	5378	0.460	14 11 20.5	+52 12 09.6	12.6	702	..

continued on next page

Table 4.3 – continued from previous page

Cluster	PID	z_{clus}	α (J2000.0)	δ (J2000.0)	Exp. time (ks)	Filter	Cluster Sample
A1902	8719	0.160	14 21 40.4	+37 17 30.5	0.8	606	1
$A1914^{\ddagger}$	8301	0.170	14 25 56.7	+37 48 58.08	0.8	606	1
$GC1444^{\dagger}$	8325	0.298	14 44 06.8	+63 44 59.6	7.5	702	..
GC1446	5707	0.37	14 49 31.2	+26 08 36.8	4.4	702	..
A1978	8719	0.147	14 51 09.4	+14 36 43.7	0.8	606	1
$MS1455^{\ddagger}$	8301	0.258	14 57 15.1	+22 20 34.9	1.0	606	1,3
A2009	8301	0.153	15 00 19.5	+21 22 10.7	0.8	606	1
$MS1512^{\ddagger}$	6832/6003	0.372	15 14 22.4	+36 36 21.0	10.4/5.8/19.8	555/675/814	3
A2125	7279	0.247	15 41 02.0	+66 16 26.2	2.6/2.6	606/814	..
A2146	8301	0.234	15 56 13.9	+66 20 52.5	1.0	606	1
GC1601	5378	0.539	16 03 13.0	+42 45 50.7	16.8	702	..
RXJ1621.4	8719	0.465	16 21 24.8	+38 10 09.0	1.0	606	1
$MS1621^{\dagger\ddagger}$	6825	0.426	16 23 35.2	+26 34 28.2	4.6/4.6	555/814	3
$A2204^{\dagger}$	8301	0.151	16 32 46.9	+05 34 33.1	0.8	606	1
GC1633	7374	0.239	16 33 42.1	+57 14 13.9	4.8	702	..
$A2218^{\ddagger}$	5701/7343	0.176	16 35 49.3	+66 12 43.5	8.4/6.5	606/702	2
$A2219^{\ddagger\dagger}$	6488	0.225	16 40 19.8	+46 42 41.9	14.4	702	2
GC1648	8131	0.377	16 48 42.5	+60 19 09.7	7.8	702	..
GC1701	8325	0.220	17 01 47.7	+64 21 00.5	7.5	702	..
GC1702	8325	0.224	17 02 13.9	+64 19 54.2	7.5	702	..
A2254	8301	0.178	17 17 45.9	+19 40 49.1	0.8	606	1
Z8197	8301	0.114	17 18 12.1	+56 39 56.0	0.6	606	1
$A2259^{\ddagger}$	8719	0.164	17 20 9.7	+27 40 07.4	0.8	606	1
$A2261^{\ddagger}$	8301	0.224	17 22 27.2	+32 07 57.5	1.0	606	1
$A2294^{\dagger\ddagger}$	8301	0.178	17 24 12.6	+85 53 11.6	0.8	606	1
RXJ1750	8301	0.171	17 50 16.9	+35 04 58.7	0.8	606	1
$MS2053^{\ddagger}$	5991/6745	0.58	20 56 21.4	-04 37 50.9	3.3/2.4/3.2	606/702/814	3
AC103	5701	0.311	20 57 01.1	-64 39 47.2	6.5	702	..
3c435a	6675	0.471	21 29 05.5	+07 33 00.2	12.8	702	..
RXJ2129	8301	0.235	21 29 40.0	+00 05 20.7	1.0	606	1
$MS2137^{\ddagger\dagger}$	5991/5402	0.313	21 40 14.9	-23 39 39.5	2.4/2.6/22.2	606/814/702	3

continued on next page

Table 4.3 – continued from previous page

Cluster	PID	z_{clus}	α (J2000.0)	δ (J2000.0)	Exp. time (ks)	Filter	Cluster Sample
$A2390^{‡}$	5352	0.228	21 53 36.9	+17 41 43.4	8.4/10.5	555/814	..
GC2157	6581	0.70	21 57 50.6	+03 48 47.3	18.8	702	..
A2409	8719	0.147	22 00 52.6	+20 58 09.7	0.8	606	1
$Cl2244^{‡}$	5352	0.330	22 47 12.2	-02 05 38.6	8.4/12.6	555/814	..
$AC114^{†‡}$	7201/5935	0.312	22 58 48.3	-34 48 07.2	15.6/16.6	702/702	..
4c27.51	6675	0.319	23 25 00.4	+28 03 11.4	5.2	702	..
$A2667^{‡}$	8882	0.2264	23 51 39.4	-26 05 03.8	12.0/4.0/4.0	450/606/814	..

†Cluster has a radial arc candidate ‡Cluster has a tangential arc candidate with $L/W > 7$

Table 4.4: Arc List

Cluster	Arc Label	z_{arc}	z ref.	Mag	Filter	L/W	Δ N”	Δ E”	Type
A11	A1	..	..	22.24±0.11	606	3.5±0.2	-0.7	-1.7	R
AC118	A1	..	..	24.29±0.19	702	9.4±1.2	2.0	-3.9	R
	A2	..	..	24.55±0.27	702	12.1±1.4	-5.4	0.5	R
	A3	..	..	24.33±0.21	702	10.4±0.9	-17.5	22.5	R
CL0024	$A^{\dagger}$	1.675	1	21.30±0.02,20.32±0.02	450/814	4.4±0.2	-4.1	32.9	T
	$B^{\dagger}$	1.675	1	22.19±0.02,21.61±0.03	450/814	3.7±0.7	-17.7	29.4	T
	C	1.675	1	21.08±0.01,19.94±0.01	450/814	5.2±0.2	-29.0	19.8	T
	D	1.675	1	22.13±0.03,21.35±0.03	450/814	4.6±0.1	11.9	-17.8	T
	$E^{\dagger}$	1.675	1	23.24±0.03,20.98±0.01	450/814	2.6±0.1	-0.7	-3.9	R
	A1	..	..	22.25±0.03,22.18±0.05	450/814	11.39±2.4	22.5	-30.0	T
	A2	..	..	23.47±0.06,23.24±0.11	450/814	12.2±1.2	-47.3	-21.3	T
	A3	..	..	23.63±0.06,22.17±0.04	450/814	8.6±0.5	-52.1	6.8	T
	$A4^{\dagger}$	..	..	24.43±0.07,22.19±0.02	450/814	2.3±0.1	-0.9	6.4	R
	A5	..	..	24.28±0.08,22.38±0.03	450/814	7.5±0.9	-2.7	60.9	T
A68	$C0ab^{\dagger}$	1.60	2	20.94±0.04	702	9.6±0.7	2.3	7.7	T
	C0c	1.60	2	23.99±0.19	702	8.3±0.4	-15.9	-11.7	T
	C4	2.625	3	22.82±0.07	702	6.2±0.6	-18.6	12.1	T

continued on next page

Table 4.4 – continued from previous page

Cluster	Arc Label	z_{arc}	z ref.	Mag	Filter	L/W	Δ N”	Δ E”	Type
	C6/C20	..	..	21.77±0.05	702	14.1±1.4	27.4	-32.3	T
	C8	0.861	4	22.73±0.04	702	4.0±0.2	30.3	-46.6	T
	C9	..	..	23.78±0.14	702	7.2±0.4	37.4	-38.7	T
	$C12^{\dagger}$	1.265	4	21.09±0.02	702	4.8±0.1	56.6	-28.8	T
	C18	..	..	22.75±0.05	702	13.6±2.5	5.5	24.2	T
GC0054	A1	..	..	24.18±0.07;23.47±0.07	555/814	7.4±0.1	-3.2	14.1	T
A209	D1	..	..	21.60±0.02	702	8.0±0.3	15.1	-16.4	T
A267	E0	..	..	23.90±0.17	702	8.7±0.9	23.3	12.6	T
A291	A1	..	..	23.14±0.15	606	3.8±0.4	-1.2	0.2	R
5c6.124	$A1^{\dagger}$	..	..	23.27±0.05	702	8.3±0.4	1.40	1.5	T
RCS0224	C	4.879	12	24.22±0.24,22.11±0.06	606/814	15.6±3.7	-8.9	-12.4	T
	R1	1.055	7	24.25±0.10,23.09±0.06	606/814	5.3±0.9	-9.5	5.5	R
	$A1^{\dagger}$	..	..	24.26±0.10,24.94±0.4	606/814	5.3±1.8	-1.5	-0.8	R
	$A2^{\dagger}$	..	..	22.94±0.05,22.15±0.04	606/814	9.6±0.4	-6.1	7.9	T
	A3	..	..	24.50±0.2,22.56±0.06	606/814	8.6±1.2	-14.5	-6.3	T
A370	$A0^{\dagger}$	0.724	25	18.92±0.01	675	13.6±0.6	-47.3	3.7	T
	A1	..	..	22.91±0.13	675	32.4±12.2	18.0	-14.7	T
	A2	..	..	23.13±0.13	675	19.6±4.9	21.8	-4.9	T

continued on next page

Table 4.4 – continued from previous page

Cluster	Arc Label	z_{arc}	z ref.	Mag	Filter	L/W	Δ N”	Δ E”	Type
	B2	0.806	26	22.93±0.06	675	4.7±0.1	-17.0	-3.9	T
	B3	0.806	26	22.99±0.06	675	4.4±0.3	-17.9	-9.1	T
	$R1/R2^{\dagger}$	..	..	22.22±0.05	675	7.0±0.4	-31.2	0.4	R
A383	B0a/B1abc/B4abc	1.01	5,6	20.22±0.02	702	16.3±0.9	-10.4	-12.0	T
	$B0b/B1d^{\dagger}$	1.01	5	22.69±0.11	702	20.2±3.3	2.6	1.8	R
	$B2ab/B2c/B3a^{\dagger}$	..	..	22.10±0.05	702	17.4±1.5	-22.5	-4.3	T
	B5	..	..	23.43±0.24	702	16.4±1.9	-15.6	8.7	T
	B6	..	..	23.10±0.10	702	9.1±1.2	-6.4	13.9	T
	B7	..	..	24.36±0.18	702	8.6±0.5	4.3	-18.7	T
	B11	..	..	24.33±0.20	702	7.5±0.4	7.1	22.9	T
GC03053	A1	..	..	21.93±0.09,21.03±0.08	606/814	20.9±1.2	17.03	-6.39	T
GC0337	$A1^{\dagger}$	..	..	23.65±0.08	702	9.3±0.7	-7.1	6.7	T
MS0440	$A1^{\dagger}$	0.5317	7	21.31±0.01	702	2.2±0.1	-7.3	18.9	T
	$A3^{\dagger}$	..	..	22.51±0.01	702	10.2±0.4	10.1	-20.4	T
	$A16^{\dagger}$	..	..	20.67±0.01	702	2.9±0.1	4.8	4.7	R
	$A17^{\dagger}$	..	..	20.26±0.01	702	3.2±0.1	5.9	0.7	R
RXJ0451	A1	2.007	7	20.24±0.03	606	19.7±3.7	-3.8	38.0	T
	A2	..	..	22.82±0.13	606	10.3±1.7	21.6	-18.6	T

continued on next page

Table 4.4 – continued from previous page

Cluster	Arc Label	z_{arc}	z ref.	Mag	Filter	L/W	Δ N"	Δ E"	Type
MS0451	A1	2.91	13	22.33±0.04	702	7.6±0.3	-4.2	31.5	T
	$A3^{\dagger}$	..	..	24.48±0.20	702	9.2±1.4	-6.5	11.3	T
	A4	..	..	22.48±0.03	702	7.2±0.2	11.9	-18.0	T
	$A5^{\dagger}$	..	..	25.21±0.32	702	11.4±2.8	-1.7	1.7	R
	A6	..	..	23.66±0.08	702	4.6±0.4	44.2	81.9	R
PKS0745	A	0.433	14	20.73±0.02;18.96±0.01	555/814	4.3±0.1	5.8	-18.3	T
4c+55	A1	..	..	21.04±0.07	606	8.9±2.1	-13.0	-7.1	T
A697	A1	..	..	22.79±0.23	606	8.3±1.9	-20.6	-9.0	T
GC0848N	A/B/C	3.356	15	22.71±0.04	702	8.8±0.7	2.0	-5.8	T
GC0848	A1	..	..	25.20±0.20	702	4.7±0.6	-0.3	-0.9	R
A773	$F0^{\dagger}$	0.650	4	22.14±0.05	702	15.5±0.9	-19.8	-16.3	T
	$F3^{\dagger}$	0.398	4	21.21±0.02	702	9.0±0.2	-17.7	-44.6	T
	$F4^{\dagger}$	..	..	23.82±0.13	702	10.6±0.8	-30.2	-49.6	T
	F9	..	..	21.58±0.03	702	9.8±0.3	-17.7	49.9	T
	F11	1.114	7	22.86±0.06	702	9.5±0.5	13.0	48.1	T
	F13	0.398	4	21.52±0.03	702	6.6±0.4	-8.1	59.5	T
	F16	..	..	23.76±0.09	702	4.6±0.3	-4.6	-8.4	R
	F18	0.487	4	23.39±0.11	702	10.0±0.8	-10.4	53.2	T

continued on next page

Table 4.4 – continued from previous page

Cluster	Arc Label	z_{arc}	z ref.	Mag	Filter	L/W	Δ N”	Δ E”	Type
3c220	A1	1.49	16	22.30±0.04;21.36±0.03	555/814	10.1±0.1	8.6	0.4	T
A868	A1	..	..	22.28±0.05	606	16.8±2.1	10.3	17.1	T
	A2	..	..	24.58±0.23	606	8.5±0.8	9.9	26.6	T
A963	H0	0.771	8	22.25±0.06	702	15.3±1.7	12.2	-0.3	T
	H1/H2/H3	1.958*	7	21.73±0.06	702	30.2±4.0	-17.9	-1.5	T
	H5	..	..	23.26±0.09	702	11.1±1.1	21.7	-4.8	T
	A1	..	..	25.03±0.30	702	8.0±1.1	15.1	14.7	T
Z3146	A1	..	..	23.55±0.30	606	11.0±3.1	-10.6	25.4	T
Z3179	A1	..	..	24.72±1.20	606	> 20.0	7.0	2.0	T
A1084	A1	..	..	23.81±0.58	606	20.3±6.2	0.5	-7.6	R
A1201	A1	0.451	9	20.35±0.03	606	7.8±0.7	1.8	-2.2	T
RXJ1133	A1	1.544	5	20.54±0.03	606	12.4±2.0	-0.7	10.7	T
	A2	1.544	5	21.56±0.05	606	7.0±0.7	3.3	-1.2	R
MS1137	A1	..	..	24.28±0.10,23.58±0.10	606/814	8.2±0.9	1.6	15.6	T
	A2	..	..	24.48±0.14,24.41±0.28	606/814	> 12.4	17.9	4.8	T
	A3	..	..	24.37±0.12,26.83±1.79	606/814	> 7.7	-13.1	6.5	T
A1682	A1	..	..	25.17±1.15	606	8.3±3.5	3.3	-1.4	R
	A2	..	..	22.28±0.11	606	25.3±5.7	3.8	-47.9	T

continued on next page

Table 4.4 – continued from previous page

Cluster	Arc Label	z_{arc}	z ref.	Mag	Filter	L/W	Δ N”	Δ E”	Type
A1689	$A1^{\dagger}$	..	..	23.40±0.02,21.98±0.04	555/814	3.2±0.1	5.9	-14.3	R
	$16.2^{\dagger}$	..	..	23.52±0.03,22.12±0.05	555/814	3.6±0.1	-0.5	-9.8	R
	$25.1^{\dagger}$	..	..	24.18±0.05,22.51±0.07	555/814	4.4±0.2	-7.0	-14.8	R
	$5.1/5.2^{\dagger}$	..	..	22.49±0.02,21.08±0.03	555/814	5.5±0.1	-18.7	-5.2	R
	$A2^{\dagger}$	..	..	23.81±0.03,22.47±0.06	555/814	3.1±0.1	-21.0	0.8	R
	$A6^{\dagger}$	..	..	23.04±0.03,22.47±0.06	555/814	6.9±0.1	9.6	9.8	R
	$19.1^{\dagger}$	..	..	23.04±0.01,22.27±0.05	555/814	7.5±1.5	4.3	32.4	T
	12.1	1.83	..	24.10±0.06,24.20±0.40	555/814	8.6±2.8	37.0	11.8	T
	A3	..	..	24.10±0.05,24.02±0.32	555/814	10.0±3.8	45.9	-11.3	T
	A4	..	..	23.09±0.02,22.84±0.13	555/814	15.3±3.5	44.8	-12.3	T
	13.1/13.2/13.3	..	..	23.53±0.08,22.55±0.21	555/814	30.6±3.5	61.0	53.5	T
	A5	..	..	24.25±0.09,22.72±0.13	555/814	7.6±1.9	-17.4	33.3	T
	8.1/8.2/19.3/19.4	..	..	21.67±0.02,20.46±0.05	555/814	30.1±1.9	-31.5	36.7	T
	1.1/2.1	3.05	..	22.35±0.02,21.51±0.06	555/814	13.8±1.9	31.7	-45.1	T
	$21.2^{\dagger\ddagger}$	..	..	-,23.85±0.34	555/814	> 12.5	-16.6	18.9	R
	$29.2^{\ddagger}$	..	..	25.97±0.39,-	555/814	13.9±1.0	53.5	8.1	T
	$A6^{a}$	..	..	24.64±0.08,-	555/814	12.1±0.7	41.0	31.9	T
A1763	J1	..	..	24.87±0.28	702	8.7±1.5	-5.9	14.1	T

continued on next page

Table 4.4 – continued from previous page

Cluster	Arc Label	z_{arc}	z ref.	Mag	Filter	L/W	Δ N"	Δ E"	Type
MS1358	$B/C^{\ddagger}$	4.92	17	22.19±0.11	606/814	14.9±1.6	-18.6	-11.7	T
A1835	$K0^{\dagger}$	..	..	24.10±0.13	702	6.1±0.3	7.2	-1.1	R
	K2	..	..	23.45±0.11	702	7.7±0.7	-0.8	20.9	T
	$K3^{\dagger}$	..	..	21.71±0.07	702	12.0±1.2	-20.8	23.3	T
A1914	A1	..	..	23.35±0.20	606	> 14.3	-25.4	-11.8	T
GC1444	A1	1.151	7	23.88±0.11	702	4.4±0.5	1.2	0.8	R
MS1455	A1	..	..	21.66±0.08	606	15.6±6.6	8.9	17.9	T
MS1512	$cB58^{\dagger}$	2.72	18	20.62±0.01;20.40±0.02;19.93±0.01	555/675/814	4.1±0.2	4.6	-2.3	T
MS1621	$A1^{\dagger}$	..	..	25.19±0.52;25.42±0.23	555/814	> 4.1	-1.5	-0.1	R
	$A2^{\dagger}$	..	..	21.21±0.03;22.10±0.04	555/814	8.9±0.1	3.4	3.5	T
A2204	A1	..	..	22.36±0.10	606	5.9±0.4	7.9	2.7	R
	A2	..	..	22.56±0.09	606	6.0±0.4	3.4	-0.3	R
A2218	M0bcd	0.702	23	21.01±0.01,20.16±0.01	606/702	11.0±0.7	-16.6	12.7	T
	$M4^{*}$	1.034	23	20.25±0.02	606/702	15.3±1.0	-53.2	35.9	T
	M1ab	2.515	24	21.33±0.02,20.82±0.02	606/702	6.5±0.7	22.4	0.9	T
	M3ab	..	..	23.03±0.08,22.94±0.10	606/702	18.3±0.3	17.0	-17.6	T
	730*	..	..	22.02±0.05	702	17.2±0.2	-59.2	45.6	T
	323	..	..	21.38±0.02,20.56±0.01	606/702	7.7±1.6	-14.3	24.2	T

continued on next page

Table 4.4 – continued from previous page

Cluster	Arc Label	z_{arc}	z ref.	Mag	Filter	L/W	Δ N"	Δ E"	Type
	382	..	..	23.75±0.16,25.47±1.00	606/702	16.2±2.0	35.1	2.7	T
	A1	..	..	23.43±0.07,23.27±0.08	606/702	7.2±0.9	-38.6	9.1	T
	$H2/H3^{*}$	..	..	23.19±0.12	702	22.9±3.0	-32.3	31.3	T
	H1/273	..	..	21.73±0.01,21.89±0.03	606/702	8.9±1.5	-20.0	40.2	T
A2219	P0	1.070	3	21.58±0.02	702	10.0±0.6	-13.9	10.6	T
	P2ab	2.730	3	22.38±0.05	702	26.9±3.0	17.3	-16.9	T
	P2c	2.730	3	22.60±0.03	702	6.0±0.2	-3.8	-26.7	T
	P13	..	..	23.94±0.11	702	9.0±0.7	4.6	-30.8	T
	$A1^{\dagger}$	..	..	23.89±0.08	702	5.3±0.5	-19.2	31.1	R
A2259	A1	1.477	7	21.70±0.08	606	17.8±4.8	-0.7	10.7	T
A2261	$A1^{\dagger}$	..	..	22.82±0.20	606	25.5±8.1	-6.6	-26.3	T
	$A2^{\dagger}$	..	..	21.76±0.04	606	7.7±0.9	8.4	23.5	T
A2294	A1	..	..	24.69±0.81	606	> 13.1	2.3	6.7	R
	A2	..	..	24.09±0.70	606	> 29.0	-19.9	-24.9	T
MS2053	AB	3.146	29	21.67±0.03;21.27±0.05;20.90±0.05	606/702/814	11.6±0.7	14.6	-3.8	T
MS2137	A01/A02	1.501	10	21.76±0.06;21.91±0.04;21.54±0.12	606/702/814	13.6±5.7	15.4	1.5	T
	AR	1.502	10	23.68±0.16;23.58±0.07;23.20±0.24	606/702/814	9.2±2.7	5.4	-0.2	R
A2390	A/C	1.033/0.913	22	21.51±0.03,19.9±0.02	555/814	10.7±0.5	17.7	-33.7	T

continued on next page

Table 4.4 – continued from previous page

Cluster	Arc Label	z_{arc}	z ref.	Mag	Filter	L/W	Δ N"	Δ E"	Type
	H3a	4.04	22	24.15±0.14,22.44±0.06	555/814	7.9±0.4	19.3	-45.1	T
	H3b	4.04	22	24.46±0.12,22.88±0.06	555/814	4.1±0.1	9.4	-49.7	T
	H5a	4.05	27	24.28±0.11,23.53±0.11	555/814	5.0±0.7	3.6	-20.4	T
	H5b	4.05	27	24.21±0.11,22.82±0.06	555/814	5.9±0.9	-9.4	-24.6	T
	A1	..	..	24.78±0.22,23.27±0.11	555/814	10.4±0.9	-6.3	5.8	T
	A2†	..	..	-,20.76±0.04	555/814	19.1±2.1	-13.5	6.1	T
	A3	..	..	22.59±0.10,22.99±0.11	555/814	8.1±0.5	-33.2	9.2	T
CL2244	*A1*†	2.237	11	20.62±0.02,20.00±0.02	555/814	10.8±0.1	1.3	-8.3	T
	A4	..	..	23.74±0.13,24.72±0.59	555/814	10.4±1.9	-1.9	33.2	T
AC114	A4/A5	..	..	22.59±0.04	702	6.9±0.4	-2.9	-0.3	R
	S1†	1.867	21	21.97±0.02	702	2.5±0.1	12.7	2.0	T
	S2†	1.867	21	21.91±0.02	702	3.1±0.1	12.7	2.0	T
	C1	2.854	19	24.17±0.10	702	5.6±0.2	29.0	5.6	T
	T1	..	..	24.68±0.36	702	29.0±4.7	-24.7	2.5	T
	T2	..	..	24.08±0.13	702	14.2±1.5	-33.1	15.5	T
	T3	..	..	22.48±0.05	702	7.7±0.6	-40.0	16.1	T
A2667	A1	1.034	7	19.67±0.01,19.33±0.01,18.26±0.01	450/606/814	14.6±2.4	13.4	6.1	T
	A2	..	..	23.07±0.06,23.59±0.16,23.50±0.37	450/606/814	18.1±8.9	7.2	14.7	T

†Photometry and L/W may be affected by poor galaxy subtraction or chip boundary ‡Unable to detect feature or get reliable photometry in one of the observed bands ⋆Redshift is only for feature H1 *Due to different imaging orientations, this arc only appear in the F702W image [a]There is a flatfielding problem with this portion of the chip for this image. While this arc is clearly detected in the F814W band, no attempt was made to correct the flatfielding problem and so no arc magnitude was recoverable. The L/W for this arc was determined solely from the F555W band. (1) Broadhurst et al. 2000; (2) Smith et al. 2002; (3) Smith et al. 2004; (4) Richard et al. in prep; (5) Sand et al. 2004; (6) Smith et al. 2001; (7) This work; (8) Ellis et al. 1991; (9) Edge et al. 2003; (10) Sand et al. 2002; (11) Mellier et al. 1991; (12) Gladders, Yee, & Ellingson 2002; (13) Borys et al. 2004; (14) Allen et al. 1996; (15) Holden et al. 2001; (16) PID 6778 abstract; (17) Franx et al. 1997; (18) Yee et al. 1996; (19) Campusano et al. 2001; (20) Smail et al. 1995; (21) Lemoine-Busserolle et al. 2003; (22) Frye & Broadhurst 1998; (23) Pello

et al. 1992; (24) Ebbels et al. 1998; (25) Soucail et al. 1988; (26) Bezecourt et al. 1999; (27) Pello et al. 1999; (29) Tran et al. 2004

Chapter 5

Constraints on the DM Halo in MS2137 Using the BCG Velocity Dispersion Profile and a 2D Lensing Analysis

David J. Sand, Graham P. Smith, Tommaso Treu, Richard S. Ellis, & Jean-Paul Kneib

California Institute of Technology, Astronomy, mailcode 105–24, Pasadena, CA 91125

Abstract

We utilize existing imaging and spectroscopic data for the galaxy cluster MS2137 to study the relative distributions of dark and baryonic material in the cluster's central regions. Following Sand et al., we combine an analysis of the stellar velocity dispersion data for the brightest cluster galaxy in conjunction with the arc redshifts and lens models to constrain the dark and baryonic mass profiles jointly. The vital new ingredient in this work is that the mass models include 2D pseudo-elliptical generalized NFW profiles for constraining the inner DM slope and the lens modeling takes into account both ellipticity and substructure introduced by cluster galaxies and the full multiple image information provided by the HST imaging. In addition to this, we relax the assumption of Sand et al. that the dark matter scale radius is 400 kpc, and instead place a prior on this parameter based

on CDM simulations. We find a relatively low value of the ellipticity of the dark matter potential of MS2137, ~ 0.10 (~ 0.2 in the surface density), and that the inner dark matter density profile is consistent with a distribution, $\rho_{DM} \propto r^{-\beta}$, with logarithmic inner slope $\langle\beta\rangle = 0.25^{+0.35}_{-0.12}$ (68% CL). Comparing this result with the 1D lensing + dynamics analysis presented by Sand and collaborators ($\langle\beta\rangle = 0.57^{+0.11}_{-0.08}$), we find the results to agree at the $1-\sigma$ level. Moreover, contrary to recent theoretical speculation, the offset between the peaks of the probability distribution for the 2D and 1D modeling analysis are of the approximate magnitude and in the direction indicated in the systematic error analysis performed by Sand and collaborators. We conclude that a significant discrepancy remains between the numerical predictions of the CDM paradigm and observations of galaxy clusters. In an Appendix, we present the lensing formalism for implementing a pseudo-elliptical generalized NFW profile into our lensing code.

5.1 Introduction

One of the basic predictions of the CDM paradigm as revealed through dark matter only numerical simulations is the 'cuspy' nature of dark matter halos ranging in mass from dwarf galaxy to galaxy clusters (e.g. Navarro et al. 1997; Moore et al. 1998). From these simulations, dark matter halos are expected to have density profiles of the form $\rho \propto r^{-\beta}$ where β lies between 1.0 and 1.5. While there is debate as to the exact form of the dark matter profile (e.g. Navarro et al. 2004; Power et al. 2003), how universal it is (e.g. Diemand et al. 2004), and what effect baryons may have upon it (e.g. Gnedin et al. 2004; Sellwood & McGaugh 2005), this consequence of the CDM paradigm nonetheless makes for an important observational test.

While the bulk of the observational work on dark matter density profiles has been done on dwarf galaxy scales (e.g. Simon et al. 2005, & references therein), there is a considerable amount of interest has been taken in the dark matter profile of galaxy clusters (e.g. Tyson et al. 1998; Sand et al. 2002, 2004; Gavazzi et al. 2003; Smith et al. 2001; Broadhurst et al. 2005a; Buote & Lewis 2004; Lewis et al.

2002; Kelson et al. 2002; Arabadjis et al. 2004). This is partially because there is more than one tool at the galaxy cluster scale for studying the DM density profile. Strong and weak gravitational lensing, X-ray measures of the surface brightness and temperature profile of the intracluster medium (assuming hydrostatic equilibrium) and dynamical measures have each been used to constrain density profiles in clusters. Each technique has its own strengths and weaknesses, and this has led us to conclude that multiple density profile measurement techniques must be mastered and understood so that the systematics of each can be controlled and consistent measurements made. In recent years good progress has been made in combining and comparing these constraints in order to constrain the structure of DM halos and the inherent systematics associated with each mass measurement technique (e.g. Sand et al. 2004; Gavazzi et al. 2003; Gavazzi 2005; Łokas & Mamon 2003). Howver, important issues remain in reconciling different measurement techniques with each other, particularly since real galaxy clusters can not be easily characterized with simple models (e.g. Gavazzi 2005; Oguri et al. 2005).

The focus of this chapter is on refining the strategy of Sand et al. (2004; see also Chapter3; hereafter S04), which sought to combine constraints from the velocity dispersion profile of a central brightest cluster galaxy (BCG) with a strong lensing analysis in six galaxy clusters. Three of the clusters in the S04 sample had both radial and tangential gravitational arcs, while the other three contained only tangential arcs. S04 found that by combining the dynamical constraints on the BCG with a simple strong lensing model they could disentangle luminous from dark matter and constrain the inner DM logarithmic slope, β, finding a mean value $\langle\beta\rangle = 0.52^{+0.05}_{-0.05}$, although individual halos could be compatible with an NFW profile.

It was pointed out by S04 that many systematic effects could affect the results found on the inner DM logarithmic slope, β. These include cluster substructure and ellipticity, orbital assumptions and template mismatch in the velocity dispersion analysis, and fixing the generalized NFW scale radius, r_{sc}, to a single value. S04 concluded that at most any one of these effects would introduce a systematic of $\Delta\beta \sim 0.2$. Other authors have pointed out that the assumption of spherical symmetry for their lensing mass model may lead to significantly higher uncertainties than that predicted by S04 (Bartelmann & Meneghetti, 2004). In particular, it has been argued that this spherical symmetry assumption systematically biases their constraints of the DM inner slope towards shallower values.

The goal of this paper is to revisit the analysis of the cluster MS2137 as presented by S04 with 2D strong gravitational lens models using a modified version of the LENSTOOL software package (Kneib 1993; see Appendix). We have implemented a pseudo-elliptical generalized-NFW mass parameterization into the code representing a generalization of the profiles seen in CDM simulations

$$\rho_d(r) = \frac{\rho_c \delta_c}{(r/r_{sc})^{\beta}(1 + (r/r_{sc}))^{3-\beta}} \tag{5.1}$$

where the asymptotic inner slope, β, is predicted to be between 1.0 and 1.5. With this improved approach we wish to address the concerns presented by Bartelmann & Meneghetti (2004); Dalal & Keeton (2003) by parameterizing the ellipticity of the DM halo and subhalos in our mass model and including all of the multiple imaging constraints available for MS2137.

A plan of the chapter follows. In § 5.2 we briefly describe our implementation of the generalized NFW profile into LENSTOOL followed by an explanation of the methodology used to model the cluster and constrain its dark matter density profile. In § 5.3 we describe how we cut down on the number of free parameters in our lens model by extracting positional, surface brightness, and geometric information from luminous galaxies in our HST imaging of MS2137. These include the ellipticity and position angle of perturbing galaxies and the BCG, along with other structural properties. In § 5.4 we present our strong lensing interpretation for MS2137 and the results of our combined lensing and dynamical analysis. In § 5.5 we discuss further systematic effects. Finally, in § 5.6 we summarize and discuss prospects for future work. Throughout this chapter, we adopt r as the radial coordinate in 3-D space and R as the radial coordinate in 2-D projected space. When necessary, we assume H_0=65 km s^{-1}Mpc^{-1}, Ω_m=0.3, and Ω_Λ=0.7.

5.2 Methodology

The goal of this chapter is to use the full 2D information provided by the deep HST imaging in the strong lensing cluster MS2137 along with the BCG velocity dispersion profile in order to disentangle luminous from dark matter and constrain the inner DM density slope of the cluster. The two-dimensional data available includes the full multiple image constraints from the tangential and radial gravitational arc systems and the projected ellipticity of the BCG and any perturbing galaxies. We also include for the possible ellipticity in the cluster dark matter halo. To achieve this goal, we have modified the LENSTOOL software package in order to include a pseudo-elliptical generalized NFW parameterization for our mass modeling of the cluster dark matter halo. In this section, we briefly introduce our new implementation of LENSTOOL and then describe our method for constraining the DM halo by combining the 2D lensing of LENSTOOL with the BCG velocity dispersion analysis.

5.2.1 A Generalized NFW Implementation in LENSTOOL

Our implementation of the pseudo-elliptical parameterization is identical to that of Golse & Kneib (2002), with the exception that we have generalized their approach beyond that of just an NFW profile to arbitrary inner logarithmic slopes. By introducing ellipticity into the potential rather than the surface mass density we make the lensing calculations more tractable given that the deflection angle is just the gradient of the scaled lensing potential. Using the following coordinate substitution of x by x_ϵ,

$$\begin{cases} x_{1\epsilon} &= \sqrt{a_1}\,x_1 \\ x_{2\epsilon} &= \sqrt{a_2}\,x_2 \\ x_\epsilon &= \sqrt{x_{1\epsilon}^2 + x_{2\epsilon}^2} \;=\; \sqrt{a_1 x_1^2 + a_2 x_2^2} \\ \varphi_\epsilon &= \arctan\left(x_2/x_1\right) \end{cases} \tag{5.2}$$

where a_1 and a_2 are two parameters defining the ellipticity we can calculate the elliptical deflection angle:

$$\vec{\alpha}_\epsilon(\vec{x}) = \left(\begin{array}{c} \dfrac{\partial \varphi_\epsilon}{\partial x_1} = \alpha(x_\epsilon)\sqrt{a_1}\cos\phi_\epsilon \\ \dfrac{\partial \varphi_\epsilon}{\partial x_2} = \alpha(x_\epsilon)\sqrt{a_2}\sin\phi_\epsilon \end{array} \right) \tag{5.3}$$

The above expression holds for any definition of a_1 and a_2 which we choose to be:

$$\begin{aligned} a_1 &= 1 - \epsilon \\ a_2 &= 1 + \epsilon \end{aligned} \tag{5.4}$$

While this choice of a_1 and a_2 do not correspond directly to the ellipticity of the potential (see Meneghetti et al. 2003b, who use a different parameterization), it does lead to simple expressions for standard lensing quantities, such as the surface mass density and shear. We present these relations in the Appendix.

Our treatment of the ellipticity has its limitations. Once the surface mass distribution of the potential is computed, it appears boxier than elliptical models. At high radii along the minor axis the surface mass density can even go negative, which is clearly unphysical. We present a full quantitative investigation of the range of ϵ for which the generalized NFW mass model is an adequate description of an underlying elliptical mass distribution in the Appendix. To summarize, after performing two tests of the adequacy of using ellipticity in the potential we conclude that this treatment is perfectly satisfactory (deviations from true ellipticity in the surface mass distribution $< 10\%$ and a positive surface mass density is retained out to $\sim 10\ r_{sc}$) for $\epsilon \lesssim 0.25$ or $\epsilon_\Sigma \lesssim 0.4$ in the surface mass distribution.

Unlike the NFW profile, the surface mass density and deflection angle of the generalized NFW profile cannot be calculated analytically. This greatly slows any lensing computation, especially when we need to calculate χ^2 values over large parameter hypercubes. To limit the computing time necessary, we created a look-up table for all of the necessary integrals from which we interpolate when performing our lensing calculations.

5.2.2 The Mass Model and Lens Modeling Method

We use the newly updated LENSTOOL ray-tracing code (Kneib 1993) to construct models of MS2137's cluster mass distribution. Here we briefly explain the lens modeling process in general terms.

In general, a lens model will have both cluster and galaxy scale mass components. The cluster scale mass component represents the DM associated with the cluster as a whole. It is this component, and its associated inner density profile, which we wish to probe in this work, in particular using the pseudo-elliptical generalized NFW mass parameterization described in the previous subsection. The cluster DM halo is modeled as

$$\rho_d(r) = \frac{\rho_c(z)\delta_c}{(r/r_{sc})^{\beta}\left[1 + (r/r_{sc})\right]^{3-\beta}} \tag{5.5}$$

which is a generalization of the numerically simulated CDM halos, with ρ_c being the critical density and δ_c a scaling factor. In our parameterization, the DM halo also has a position angle (θ) and ellipticity (ϵ) associated with it.

Galaxy scale components are necessary to account for perturbations to the cluster potential that seem plausible based on the HST imaging and are demanded by the lens model. These components are described by pseudo-isothermal elliptical mass distributions (PIEMD) in this work. Each PIEMD mass component is parametrized by its position ($x_{\rm c}$, $y_{\rm c}$), ellipticity (ϵ), position angle (θ), core radius ($r_{\rm core}$), cut-off radius ($r_{\rm cut}$) and central velocity dispersion ($\sigma_{\rm o}$). The projected mass density, Σ is given by:

$$\Sigma(x,y)=\frac{{\sigma_{\rm o}}^2}{2G}\,\frac{r_{\rm cut}}{r_{\rm cut}\,-\,r_{\rm core}}\left(\frac{1}{({r_{\rm core}}^2\,+\rho^2)^{1/2}}-\frac{1}{({r_{\rm cut}}^2\,+\rho^2)^{1/2}}\right) \tag{5.6}$$

where $\rho^2=[(x-\ x_{\rm c})/(1+\epsilon)]^2+[(y-\ y_{\rm c})/(1-\epsilon)]^2$ and the ellipticity of the lens is defined as $\epsilon=(a-b)/(a+b)$ (this quantity should not be confused with the quite different ellipticity definition used for the pseudo-elliptical generalized NFW profile). In order to relate Equation 5.6 to the observed luminosity of the galaxy, we take $\Sigma = (M/L)I$, where M/L is the mass to light ratio and I is the intensity, and find the following relation

$$M/L = \pi\ {\sigma_{\rm o}}^2 r_{\rm cut}\ /(GL) \tag{5.7}$$

The M/L of the central BCG will be used as a free parameter in our mass modeling analysis.

For typical galaxy scale components, we fix the galaxy position through examination of the HST imaging, and use the IRAF task ELLIPSE to find and fix the galaxy ellipticity and position angle. Both the core and cutoff radius are measured from the 1-dimensional surface brightness profile of the perturbing galaxy. The one perturbing galaxy used in the analysis of MS2137 can be seen in Fig. 5.2.

A special case is the BCG, which we assume to be coincident with the center of the cluster DM halo in our analysis, whose mass parameterization is assumed to comprise only the stellar mass, given that we wish to distinguish between stellar and dark matter in our final cluster analysis in the inner core. Also, we intend to use the stellar kinematics of the BCG as a further constraint on the mass profile in the central regions of the cluster. To do this, we would like to utilize the Jaffe stellar density parameterization for the BCG presented in Sand et al. (2002, 2004) since it has analytic solutions to the spherical Jeans equation while the PIEMD model used for the lensing does not. Via this method, we can appropriately use the PIEMD model for the lensing portion of the analysis and then the Jaffe parameterization for the BCG dynamics portion of the analysis, since their surface mass distribution at that point will be essentially identical.

A χ^2-estimator is used to quantify the level of agreement between the strong lensing interpretation taken from the HST imaging data and the predictions of a given trial lens model. The value is calculated in the image plane and is based on the image positions only:

$$\chi^2_{pos}=\sum_{i=1}^{N}\frac{(x_{model}-x_{HST})^2+(y_{model}-y_{HST})^2}{\sigma^2_{pos}} \tag{5.8}$$

Where σ_{pos} is the positional error associated with a multiply imaged knot, which we take to be $0\farcs2$ throughout this work. At the beginning of the modeling process there is some iterative work done in order to pin down the acceptable values of perturbing galaxies and to clarify the lensing interpretation.

Once the lensing interpretation is finalized and the perturbing galaxy parameters are fixed, we constrain the remaining free parameters, including the inner dark matter slope by calculating χ^2_{pos} over a hypercube grid which encompasses the full range of acceptable models. This allows for easy marginalization of nuisance parameters and the calculation of confidence regions.

5.2.3 Incorporating the Dynamical Constraints

As was done in S04, we further constrain the dark halo inner slope by using the observed velocity dispersion profile of the BCG. The interested reader is referred to Chapter 3. We calculate this portion of the χ^2 by comparing the expected velocity dispersion profile of the BCG given a mass model with the observed velocity dispersion profile, taking into account the effects of seeing and the long slit shape used for the observations. We ignore the ellipticity in the BCG and dark matter halo here as its effect on the velocity dispersion profile will be negligible.

We lead the reader step by step through the analysis in the following sections. First, in § 5.3 we describe how we measure the parameters of the perturbing galaxy and BCG from the HST imaging data in order to cut down on the number of free parameters in our model. Then, in § 5.4.1, we present the multiple image interpretation of MS2137. We systematically compare our results with those obtained in

Sand et al. 2004 in § 5.4.2 by adopting all of their assumptions, relaxing only the assumption of spherical symmetry in the mass model. We then go on and adopt a CDM motivated prior for the range in scale radius, r_{sc}, and repeat our analysis in § 5.4.3.

5.3 Observational Results

Observational results for the cluster MS2137 have been presented in particular Chapters 2 & 3 where the HST data reduction, BCG surface brightness fitting, redshift measurements of the giant arcs and the spectroscopic measurement of the velocity dispersion profile of the BCG are discussed. In this section we focus on two aspects of our new analysis. First, we review measuring the relevant PIEMD parameters for the perturbing galaxy and the BCG. We also describe how we convert between the PIEMD model of the BCG for the strong lensing analysis to a Jaffe model in order to simplify our dynamical modeling.

5.3.1 Cluster galaxy geometry and fitting

In order to minimize the number of free parameters in our mass model, we utilized the HST imaging to measure the luminous components which we included in our modeling. As we will see in § 5.4.1, there is only one perturbing galaxy and the BCG for which we must extract as much information as possible.

In order to fix the position angle and ellipticity of both the perturber and BCG components we use output from the IRAF task ELLIPSE at roughly the effective radius and fix the measured parameters in our lensing analysis. We also fix the perturbing galaxy's position, core radius ($r_{\rm core}$) and cutoff radius ($r_{\rm cut}$) to that which matches its light distribution. See Table 5.1. This leaves only the PIEMD parameter velocity dispersion ($\sigma_{\rm o}$) which must be adjusted to match the multiple imaging constraints.

The situation for the BCG is slightly more complicated. As in S04, we would like to be able to use the Jaffe density profile fit to represent the BCG component of the mass model for the velocity dispersion portion of the analysis since this function provides an analytic solution to the spherical Jeans equation. However, the only parametrized model available in LENSTOOL is the PIEMD model. To bridge this gap we use the IRAF task ELLIPSE to measure the position angle and ellipticity of the BCG. We then take the Jaffe surface brightness fit presented by S02 and fit a corresponding PIEMD model. In order to match the PIEMD model to the Jaffe profile found by S04 (and taken from the 2D $R^{1/4}$ surface brightness fit) a by-eye comparison was made between the 1D profiles. The PIEMD model is used to represent the BCG in the lensing analysis while the corresponding Jaffe profile is used in the dynamical analysis. Figure 5.1 shows a comparison between the PIEMD and Jaffe profiles and Table 5.1 lists their corresponding parameters.

Table 5.1: Fixed Parameters in MS2137-23 Lens Model

Parameters	x_c (arcsec)	y_c (arcsec)	b/a	θ (deg)	r_{core} (kpc)	σ_0 (kms^{-1})	r_{cut} (kpc)
Cluster-scale DM halo	0.0	0.0	-	5.0	-	-	-
BCG_{Jaffe}	0.0	0.0	0.83	17.75	5×10^{-6}	-	22.23
Galaxy Perturber	16.2	-5.46	0.66	159.9	0.05	173.0	4.8

The position angle, θ is measured from North towards East. The DM halo is parameterized with the pseudo-gNFW profile. All other mass components are parameterized by a PIEMD model.

5.4 Results

In this section we present our results on the DM inner slope. First, we present the multiple image interpretation of MS2137 and discuss the final set of free parameters that we adopt in our mass model. With this information in hand we compare our results directly to those of S04 by adopting a generalized NFW scale radius of 400 kpc to directly determine the effect of including ellipticity into our analysis. Following this, we adopt a more suitable prior range for the scale radius, r_{sc},

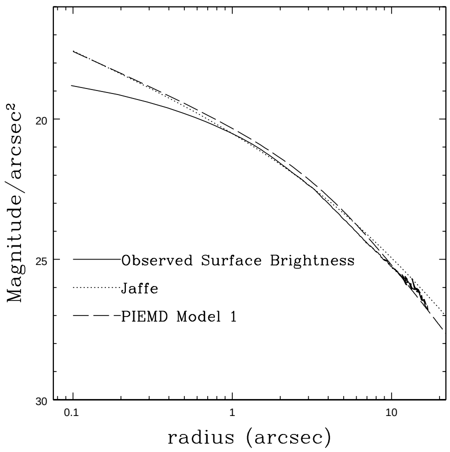

Figure 5.1: Surface Brightness Fits and PIEMD models. The observed surface brightness profile of the BCG is shown with the unconvolved Jaffe profile fit. The surface brightness model of the PIEMD model is meant to represent this Jaffe luminous distribution in the strong lensing portions of the analysis.

between 50 and 200 kpc, which fits the data best.

5.4.1 MS2137 Multiple Image Interpretation and Final Free Parameter Set

The strong lensing properties of MS2137 have been studied extensively by many workers (e.g. Mellier et al. 1993; Miralda-Escude 1995; Hammer et al. 1997; Gavazzi et al. 2003; Gavazzi 2005). The most detailed strong lensing model has been presented by G03, who used 26 multiply-imaged knots from two different background sources to constrain the lensing properties of MS2137. Our strong lensing model is more conservative than that of G03, in the sense that it is based only on those multiple images in which we are confident based on spectroscopy, surface brightness expectations from gravitational lensing theory and interim lens modeling results. It is not likely that this slight difference in interpretation greatly effects the mass model constraints in MS2137.

We interpret the tangential and radial arcs in MS2137 to come from two separate background galaxies at $z = 1.501$ and $z = 1.502$, respectively (see S02 for spectroscopy). Our multiple image interpretation is detailed in Figure 5.2 and Table 5.2. There are two separate features (features 1 and 3) on the tangential arc source galaxy which we have confidently identified to be multiply imaged four and three times respectively. We have not been able to confidently locate the fourth image of feature 3 and so do not include it as a constraint. Two images of the radial arc source galaxy were identified. We could not confidently locate the mirror image of feature 2a nearer the center of the BCG, most likely due to residuals in the BCG subtracting process. For this reason, no constraint was used.

Much was learned about the mass model of MS2137 during the process of understanding the multiple image interpretation. With some experimentation, it was clear that the perturbing galaxy (see Fig. 5.2) did not have a strong effect on the lensing χ^2 (and thus on our ultimate conclusions on the inner dark matter density slope). After using the HST imaging, the galaxy perturber only had one more PIEMD free parameter to be characterized, $\sigma_{\rm o}$. When this parameter was allowed to vary, the best-fitting χ^2 value always occurred near $\sigma_{\rm o}$=173 km/s. We kept this value of $\sigma_{\rm o}$ in the perturbing galaxy fixed throughout the remainder of the analysis, leaving the perturber completely characterized.

One of the primary goals this study seeks to answer is the effect introducing ellipticity can have on the inner slope of the dark matter density profile. Therefore, in our initial modeling and iterations to determine the lensing interpretation of MS2137, we experimented with different cluster dark matter ellipticities and position angles. While some variation in the ellipticity is permitted by our lensing interpretation, we detected a robust offset between the position angle of the BCG and that of the dark matter halo of ∼13 degrees, in agreement with previous strong lensing studies of MS2137-23 (Gavazzi et al., 2003). Changing the dark matter position angle slightly had no effect on the resulting best-fitting inner dark matter halo slope and for this reason, we fixed the dark matter position angle to 5.0 degrees throughout. We keep the ellipticity of the dark matter halo as a free parameter, however, in order to constrain its allowed range.

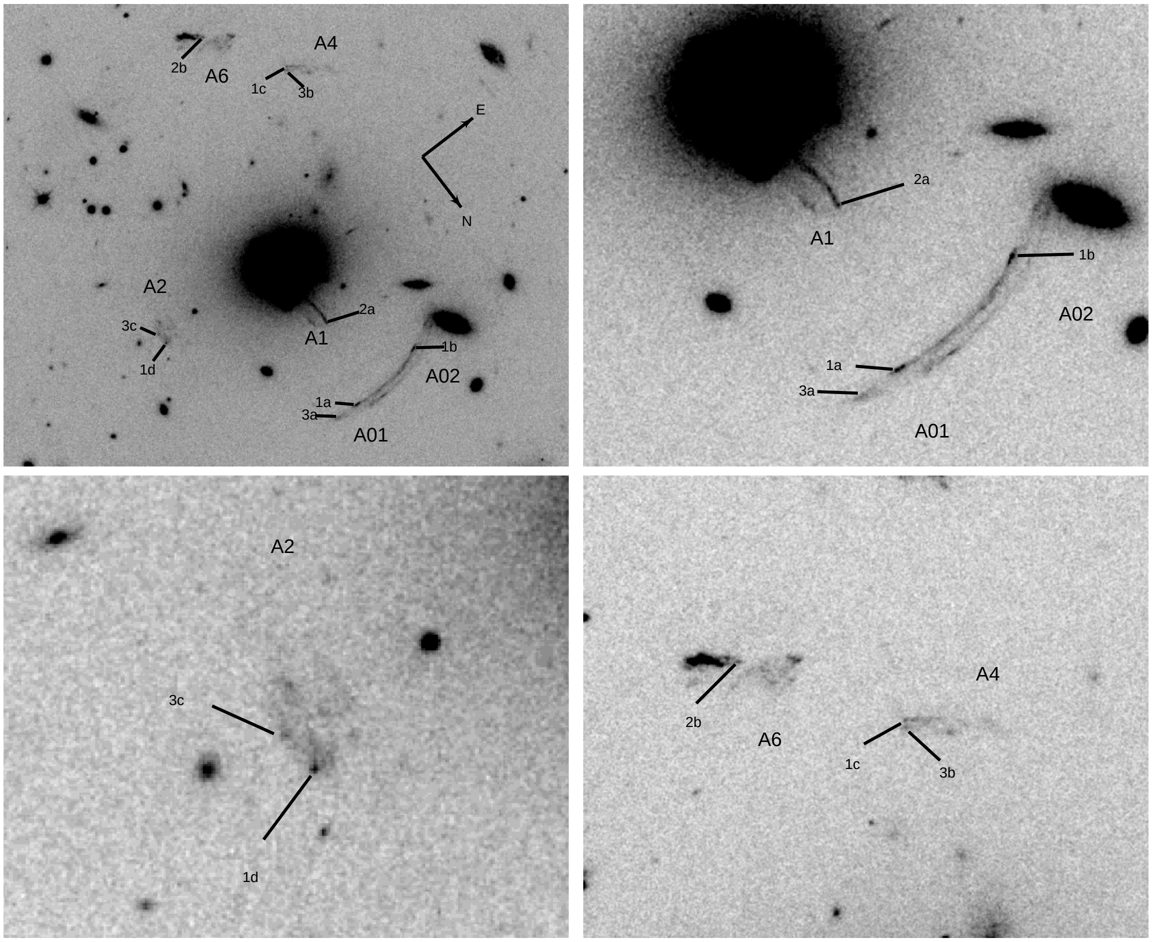

Figure 5.2: Multiple image interpretation of the cluster MS2137. The exact positions used are shown in Table 5.2. Three sets of multiple images are identified, one with the radial arc system (2a & 2b) and two with the tangential arc system (1abcd & 3abc). The perturbing galaxy is the elliptical S0 next to the lensed feature 1b.

This leaves four or five free parameters in the final mass model (depending on whether we decide to keep the scale radius fixed (§ 5.4.2) or allow it to vary (§ 5.4.3)): the inner dark matter slope, β, the dark matter halo ellipticity, ϵ, δ_c, the dark matter scale, r_{sc}, the dark matter scale radius and the M/L of the BCG. As discussed in § 5.2.2, by computing the χ^2 over a hypercube of values encompassing the acceptable range of the above free parameters we can marginalize nuisance parameters and obtain constraints on the quantities of interest in this work.

Table 5.2: Multiple Image Interpretation

Cluster	Multiple Image ID	x_c (arcsec)	y_c (arcsec)
MS2137	1a	6.92	-13.40
	1b	12.40	-7.94
	1c	0.07	19.31
	1d	-11.57	-7.49
	2a	3.96	-5.51
	2b	-8.01	22.10
	3a	5.16	-14.68
	3b	0.11	18.91
	3c	-12.30	-6.74

Multiple Image Interpretation. Uncertainties on all positions are $0\farcs2$ for the lensing analysis. All image positions are with respect to the BCG center.

5.4.2 Comparison with Sand et al. (2004)

In this section we would like to directly compare the 1D lensing+dynamics analysis of S04 with the 2D multiple image strong lensing+dynamics analysis presented here. To do this, we fix the dark matter scale radius, r_{sc}, to 400 kpc, as was done by S04. In this way, we directly mimic the analysis of S04 with the exception of the multiple image interpretation presented in § 5.4.1 and the ellipticity and PA of both the BCG and cluster DM halo. This allows us to see directly how these enhancements to our lensing model affect our conclusions on the DM inner slope.

The results of our analysis are presented in Fig. 5.3 with a direct comparison to the analogous results of S04. As can be seen, when comparing the lensing-only results, the current results and those of S04 are largely consistent. The range in BCG M/L ratio are identical. However, there is no tail of acceptable lens models to low values of the DM inner slope, β, as was seen in S04. It turns out that models with shallow inner dark matter slopes can match the critical line position of the tangential and radial arcs but cannot at the same time match the *angular* structure of the lensed images, that is, the full multiple image constraints.

Turning to the constraints on the DM halo derived from the combined lensing and dynamics, we see that the final derived inner dark matter slope using the two methods is different. The current two-dimensional analysis favors much steeper slopes, with a best-fitting value of β ~1.2 as opposed to the β ~0.6 value found by S04. The range of allowed ellipticity in the potential of the dark matter halo are $\epsilon \sim 0.08 - 0.12$ which corresponds to a range of ellipticity in the surface mass distribution between ~0.15 and 0.22.

At face value, it seems as if the analysis of S04 was too simplistic and did not capture the true inner slope of the dark matter density profile as claimed by Bartelmann & Meneghetti (2004); Dalal & Keeton (2003). However, it should be noted that the total best-fitting χ^2 for this two-dimensional r_{sc}=400 kpc scenario is not so satisfactory, χ^2 =25.30 for 16 degrees of freedom (twenty constraints from the lensing interpretation with the velocity dispersion profile and four free parameters). A worse χ^2 would be had only ~5% of the time if this model were correct. Is it possible that fixing the scale radius to r_{sc}=400 kpc results in us not finding the best-fitting mass model? In order to check this idea further, we now explore a range of scale radii, taking expectations from CDM simulations and previous strong lensing analyses (e.g. Gavazzi et al. 2003) as a prior.

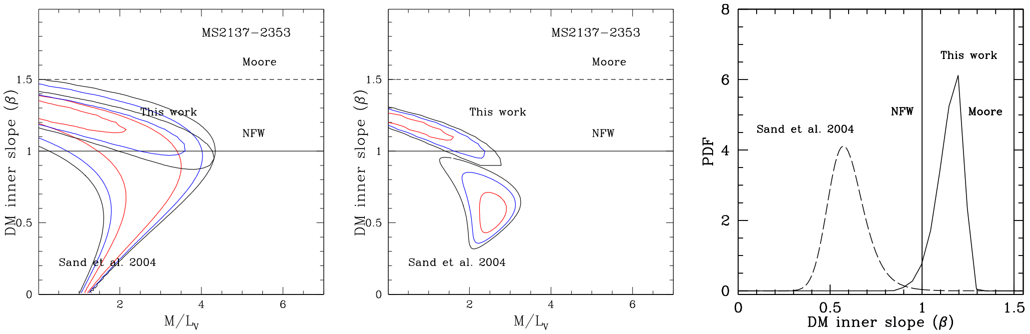

Figure 5.3: Fixed scale radius = 400 kpc scenario. Left–Direct comparison between the lensing only likelihood contours (68%,95%, and 99%) found in Sand et al. 2004 and this work. Note that the allowed range in M/L ratio is identical to that in S04, but that the addition of ellipticity into the lens model, along with the more detailed multiple image interpretation leads to tighter contours.

5.4.3 Wide Scale Radius Prior

An array of CDM simulations have provided information not only on the inner dark matter density profile, but on the expected value of the scale radius, r_{sc}, and its intrinsic scatter at the galaxy cluster scale (e.g. Bullock et al. 2001; Tasitsiomi et al. 2004; Diemand et al. 2004). For example, Bullock et al. (2001) found that dark matter halos the size of small galaxy clusters have scale radii between 240 and 550 kpc (68% CL). Tasitsiomi et al. (2004), using higher resolution simulations with fewer dark matter halos found r_{sc} of 450±300 kpc. In addition, a previous strong lensing analysis of MS2137-23 by Gavazzi et al. (2003) has provided some hints as to the approximate value of the scale radius in this system. Gavazzi et al. found a best fitting scale radius of ∼130 kpc (and hints that the scale radius may be as low as ∼70 kpc from their weak lensing data) for their analysis of MS2137, and although they used a slightly different parameterization of the BCG and included weak lensing data into their analysis, we took this information along with the results from CDM simulations into account and decided on a uniform scale radius prior between 50 and 200 kpc.

With this prior on the scale radius, we ran a similar analysis to that performed in the r_{sc}=400 kpc case, with the scale radius as an additional parameter to marginalize over. The results are presented in Figure 5.4. Once we let the scale radius vary within this range we get quite different results then for the fixed r_{sc}=400 kpc case. In fact, the overall constraints on β obtained are in agreement with those of S04. The trend is toward slightly smaller M/L ratios in the BCG, but still in the range of M/L between 1.5 and 2, which is expected from the evolution of the fundamental plane (right panel;Figure 5.4) . Adopting the peak of the 1D probability distribution as the best estimate of the inner slope, we get β=$0.25^{+0.35}_{-0.12}$ (68% CL). The upper limit on β at the 95% confidence limit is 0.91. We conclude that a significant discrepancy remains between the dark matter halo observed in MS2137 and those seen in numerical simulations exists. When compared with the best fit value obtained by S04 ($\langle\beta\rangle = 0.57^{+0.11}_{-0.08}$), we find the results to be in reasonable agreement, although the allowed range in β in the current analysis is signficantly wider reflecting the uncertainty in the scale radius. Moreover, the offset between the peaks of the probability distribution for the 2D and 1D modeling analyses are of the approximate magnitude ($\Delta\beta$ ∼0.2) and in the direction indicated by S04, suggesting that the original systematic error analysis they performed was roughly correct.

Given we have modified the method adopted by S04 in two ways - a two-dimensional lensing analysis and a less restricted scale radius - a key question is the following: How good a fit does the our mass model provide to the data? Importantly, the best-fitting model is significantly better than that for the r_{sc}=400 kpc model; χ^2 =22.30 for 15 degrees of freedom (one less degree of freedom since we have one extra free parameter). Statistically, models which correctly represented the underlying cluster density profile would get a worse χ^2 10% of the time, indicating a reasonable fit to the data. We are also able to constrain the ellipticity in the dark matter halo potential quite strongly (right panel, Fig 5.4). As in the r_{sc}=400 kpc case, we found a ϵ value centered around 0.1, translating into an ellipticity in the surface density profile of ∼0.2.

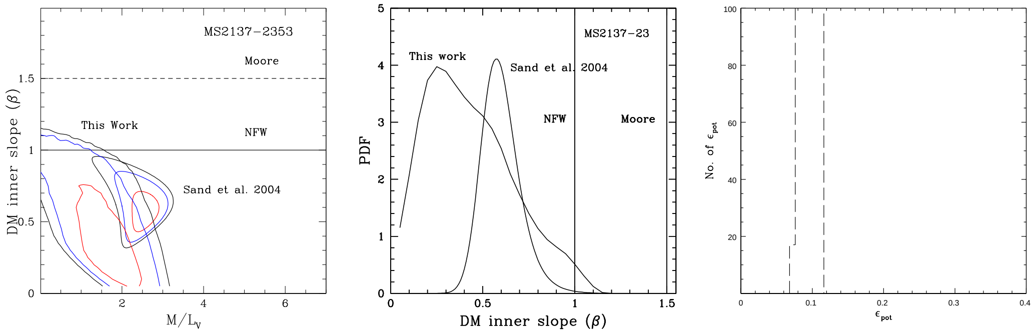

Figure 5.4: Uniform prior on scale radius, 50-200 kpc. Constraints on β when a larger prior on scale radius is taken. Right–A histogram illustrating the range of ellipticity (in the potential) which correspond to mass profiles within 3-σ of the best fitting mass profile. The ellipticity in the potential is tightly clustered around ϵ=0.1, which corresponds to a surface mass density ellipticity of ~0.2.

From this analysis, what can we conclude about the earlier criticism presented by Bartelmann & Meneghetti (2004); Dalal & Keeton (2003), which declared that the neglect of two-dimensional effects in the lens model of S04 caused a systematic bias towards shallower dark matter density profiles? There are a couple of factors which reconciled our analysis with the original work of S04. First, we have allowed a range of scale radii as opposed to the fixed scale radius of 400 kpc used in S04. If we stick with the assumption of S04 and use a fixed scale radius, we recover dark matter density slopes which are steep and compatible with CDM simulations and not in agreement with S04. However, once we allow the scale radius to vary, shallower inner density slopes are found with a lower overall reduced χ^2 value indicating that the fits are superior. Just as importantly, the cluster MS2137 is not very elliptical, having a surface mass density ellipticity of ~0.2. This result is not an accident since S04's sample of clusters were chosen to be roughly circular exactly to avoid the complications of ellipticity. There is theoretical evidence that the correct dark matter density profile can be inferred using axially symmetric models in roughly circular clusters like MS2137 (Meneghetti et al. in preparation), as was seen in the observational work presented here.

5.5 Remaining Systematics

In this work we have addressed the major systematic uncertainty in the joint strong lensing and BCG dynamics analysis of S04. We have implemented a 2D gravitational lensing code which allows us to take into account ellipticity and cluster substructure. However, other systematic uncertainties still remain, including those having to do with template mismatch and orbital assumptions in the dynamical analysis, as discussed thoroughly in S04.

Several simplifications in the lens model still remain. For example, we restrict the dark matter halo and BCG to be exactly coincident in order to properly run our joint analysis. While this assumption appears to be quite good in MS2137 (some exploratory lens models were run in which the BCG and dark matter halo were allowed to have a small offset; all good models seemed to be offset by no more than <0.5 arcseconds). Real CDM halos are triaxial in nature, while our lens modeling did not properly take this into account. Though this does not likely effect our constraints on the the inner slope, it could have a relatively large effect on our constraints on the scale radius (see e.g. Oguri et al. 2005; Gavazzi 2005). It would also be interesting to see if there was a systematic uncertainty associated with the multiple lensing interpretation. The multiple lensing interpretation presented in this work is quite different from that presented by Gavazzi et al. (2003) for the same system. In the future, it should be straightforward to run the same analysis discussed in this chapter with the Gavazzi strong lensing constraints and compare them with the results presented here.

5.6 Summary & Future Work

In this final chapter, we have implemented an upgraded version of the gravitational lensing code LENSTOOL, which uses a pseudo-elliptical generalized NFW profile to account for ellipticity and substructure in the mass model of the galaxy cluster MS2137. Together with velocity dispersion profile measurements of the BCG, this has led to strong constraints on the inner dark matter density slope. Our final parameter estimate on the inner logarithmic slope is $\langle\beta\rangle = 0.25^{+0.35}_{-0.12}$ (68% CL), in disagreement with expectations of the CDM paradigm. Our work also showed that the general conclusions of S04 were correct, that the DM inner slope was shallow. This is most likely because the cluster is not strongly elliptical (with the ellipticity in the surface density being ~ 0.2), which was one of the original criteria for selection by S04.

There are several future avenues to explore with this cluster. The degeneracy between scale radius and inner dark matter density slope may be broken, since it is a result of projection effects, if an additional mass probe was had a large radius, such as weak lensing. Given that there is published weak lensing data for MS2137, we will incorporate this additional constraint on the mass profile in the near future. Also, the cluster MS2137 has deep Chandra data ($\sim$ 100 ks) with which a comparison hydrostatic equilibrium mass analysis can be performed. A comparison between the two mass profile results could lend insight into the state of the intracluster gas. Alternatively, using the deep Chandra data to constrain the hot gas contribution to the total cluster mass budget and disentangling that from the mass profile in the current analysis would isolate the dark matter halo even further, leading us one step closer to the true dark matter density profile.

5.7 Appendix: Lensing Formalism & the Pseudo-Elliptical gNFW Implementation

Here we discuss the implementation of the pseudo-elliptical generalized NFW profile into the LENSTOOL software package. The interested reader is referred to Kneib (1993); Smith et al. (2005) for further details about the LENSTOOL software.

The following is a brief overview of basic gravitational lensing formalism (see e.g. Schneider et al. 1992; Narayan & Bartelmann 1996). We will often use dimensionless radial coordinates, $\vec{x} = \vec{R}/r_{sc} = \vec{\theta}/\theta_{sc}$ (where $\theta_{sc} = r_{sc}/D_l$). Given the thin lens approximation and a three-dimensional Newtonian gravitational potential, $\Phi(R, z)$, then

$$\varphi(\vec{\theta}) = \frac{2D_{ls}}{c^2 D_l D_s} \int_{-\infty}^{+\infty} \Phi(D_l \vec{\theta}, z) dz \tag{5.9}$$

is the scaled, projected potential. From this quantity, the deflection angle $\vec{\alpha}$, convergence κ, and shear γ can be computed:

$$\vec{\alpha}(\vec{\theta}) = \vec{\nabla}\varphi(\vec{\theta}) \tag{5.10}$$

$$\kappa(\vec{\theta}) = \frac{1}{2}(\frac{\partial^2 \varphi}{\partial \theta_1^2} + \frac{\partial^2 \varphi}{\partial \theta_2^2}) \tag{5.11}$$

$$\gamma^2(\vec{\theta}) = \frac{1}{4}(\frac{\partial^2 \varphi}{\partial \theta_1^2} - \frac{\partial^2 \varphi}{\partial \theta_2^2})^2 + (\frac{\partial^2 \varphi}{\partial \theta_1 \partial \theta_2})^2 \tag{5.12}$$

We now take the case of an axially symmetric lens and connect that with our pseudo-elliptical implementation. The density profile for a generalized NFW profile looks like,

$$\rho_{DM}(r) = \frac{\rho_c \delta_c}{(r/r_{sc})^{\beta}(1 + (r/r_{sc}))^{3-\beta}}, \tag{5.13}$$

with an inner slope β (NFW and M98 correspond to $\beta = 1, 1.5$ respectively; ρ_c is the critical density). The surface mass density then becomes

$$\Sigma_{DM}(R) = 2\rho_c r_{sc} \delta_c x^{1-\beta} \int_0^{\pi/2} d\theta \sin\theta (\sin\theta + x)^{\beta-3}, \tag{5.14}$$

and the mean surface density inside x is

$$\overline{\Sigma}_{DM}(x) = \frac{1}{\pi x^2} \int_0^x 2\pi x \Sigma_{DM}(x) dx \tag{5.15}$$

For arbitrary values of β, the above integrals must be computed numerically. There are also straightforward expressions for the deflection angle α, convergence κ, and shear γ (Miralda-Escude, 1991)

$$\alpha(x) = \theta \, \frac{\overline{\Sigma}(x)}{\Sigma_{\text{crit}}} \tag{5.16}$$

$$\kappa(x) = \frac{\Sigma(x)}{\Sigma_{\text{crit}}} \tag{5.17}$$

$$\gamma(x) = \frac{\overline{\Sigma}(x) - \Sigma(x)}{\Sigma_{\text{crit}}} \tag{5.18}$$

With these relations set, we will now introduce an ellipticity, ϵ, into the lens potential, $\varphi(\theta)$. Consider the following elliptical coordinate system:

$$\begin{cases} x_{1\epsilon} & = & \sqrt{a_1}\, x_1 \\ x_{2\epsilon} & = & \sqrt{a_2}\, x_2 \\ x_\epsilon & = & \sqrt{x_{1\epsilon}^2 + x_{2\epsilon}^2} \; = \; \sqrt{a_1 x_1^2 + a_2 x_2^2} \\ \varphi_\epsilon & = & \arctan\left(x_2/x_1\right) \end{cases} \tag{5.19}$$

where a_1 and a_2 are two parameters defining the ellipticity. We can calculate the elliptical deflection angle, given that $\varphi_\epsilon(x) = \varphi(x_\epsilon)$:

$$\vec{\alpha}_\epsilon(\vec{x}) = \begin{pmatrix} \dfrac{\partial \varphi_\epsilon}{\partial x_1} = \alpha(x_\epsilon)\sqrt{a_1}\cos\phi_\epsilon \\ \dfrac{\partial \varphi_\epsilon}{\partial x_2} = \alpha(x_\epsilon)\sqrt{a_2}\sin\phi_\epsilon \end{pmatrix} \tag{5.20}$$

This expression holds for any value of a_1 and a_2 and for our purposes we use:

$$\begin{aligned} a_1 &= 1 - \epsilon \\ a_2 &= 1 + \epsilon \end{aligned} \tag{5.21}$$

This definition of a_1 and a_2 lead to simple expressions for the deflection angle and κ, unlike other choices in the literature (Meneghetti et al., 2003b), and is related to the standard ellipticity in the potential (1-b/a) by

$$\epsilon_\varphi = 1 - \sqrt{\frac{1-\epsilon}{1+\epsilon}}. \tag{5.22}$$

If we combine several of the above relations we have:

$$\kappa_\epsilon(\vec{x}) = \frac{1}{2\theta_s^2}\left(\frac{\partial^2\varphi_\epsilon}{\partial x_1^2} + \frac{\partial^2\varphi_\epsilon}{\partial x_2^2}\right) = \kappa(\vec{x}_\epsilon) + \epsilon\cos 2\varphi_\epsilon\,\gamma(\vec{x}_\epsilon) \tag{5.23}$$

Similarly, the shear $\gamma_\epsilon(\vec{x})$ can be written as:

$$\begin{aligned}\gamma_\epsilon^2(\vec{x}) = \gamma^2(\vec{x}_\epsilon) \quad &+ \quad 2\epsilon\cos 2\phi_\epsilon\gamma(\vec{x}_\epsilon)\kappa(\vec{x}_\epsilon) \\ &+ \quad \epsilon^2(\kappa^2(\vec{x}_\epsilon) - \cos^2 2\phi_\epsilon\gamma^2(\vec{x}_\epsilon)).\end{aligned} \tag{5.24}$$

Finally, the projected mass density $\Sigma_\epsilon(\vec{x})$ is simply determined from equations (5.23) and (5.18):

$$\Sigma_\epsilon(\vec{x}) = \Sigma(\vec{x}_\epsilon) + \epsilon\cos 2\phi_\epsilon(\overline{\Sigma}(\vec{x}_\epsilon) - \Sigma(\vec{x}_\epsilon)). \tag{5.25}$$

To get a feel for the relation between ϵ and the ellipticity in the surface mass density, ϵ_Σ, we plot several values in Fig. 5.6.

5.7.1 Limitations of Pseudo-Elliptical Treatment

In this section we quantitatively investigate the range of ϵ for which the generalized NFW pseudo-elliptical mass model (which is elliptical in the potential) is an adequate description of an elliptical mass distribution. In Figure 5.5 the extent to which our implementation does not produce surface density profiles with true elliptical surface density isocontours is illustrated. As the parameter ϵ increases the surface density isocontours become more boxy and peanut shaped. However, at relatively low ϵ, the isocontours are very nearly elliptical. To what degree can we consider our treatment of ellipticity an accurate method for representing elliptical surface density distributions?

One way is by directly measuring the degree of boxiness, where we measure the distance, δr between a surface density contour and a real ellipse with the same major and minor axis radii (as was done in Golse & Kneib 2002; see Fig. 5.7). We plot $\delta r/r$ as a function of ϵ for several values of the inner slope, β, and a variety

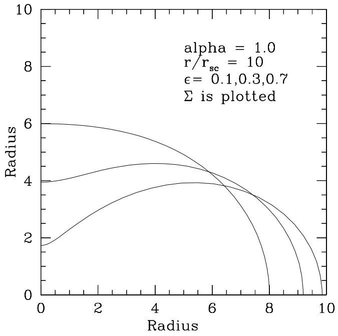

Figure 5.5: Illustration of projected density isocontours for our pseudo-elliptical generalized NFW parameterization with r/r_{sc}=10.0 and β=1.0. Note that as ϵ gets larger, the projected density contours become more dumb-bell shaped.

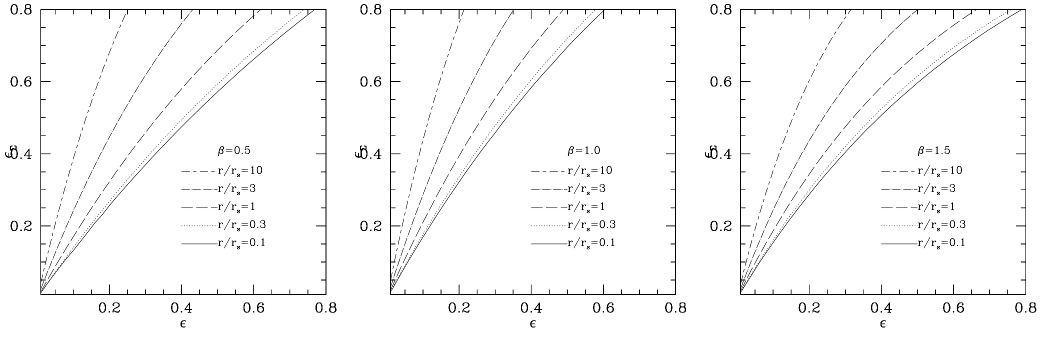

Figure 5.6: The ellipticity of the projected density, Σ, as a function of the ellipticity in the potential for different values of β.

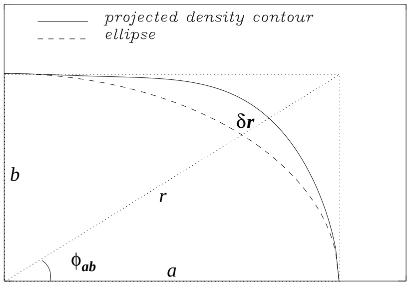

Figure 5.7: Illustration of the method used to compare a projected density contour using our pseudo-elliptical methodology and a real ellipse. $\delta r/r$ characterizes the deviation. See Figure 5.8. This figure is reproduced from Golse & Kneib (2002).

of r/r_{sc} in Fig. 5.8. If we desire our pseudo-elliptical implementation to be within 10% of a true elliptical surface density distribution for the range of $r/r_{sc} < 10$, then values of $\epsilon \lesssim 0.25$ are appropriate.

One very unphysical consequence of introducing ellipticity into the potential is that the surface mass density can become negative, especially near the minor axis where $cos(2\phi_\epsilon) = -1$. In Figure 5.9 we plot the distance along the minor axis at which Σ_ϵ becomes negative for several inner slopes. If we wish to restrict ourselves to values of ϵ where the surface density does not go negative at less than r/r_{sc}, then again we find that we must deal with values of ϵ less than approximately 0.25.

Based on the above two tests, we conclude that one can safely use values of $\epsilon \lesssim 0.25$ when trying to represent elliptical surface mass distributions in a lens model. Based on Fig 5.6, this means that we can accurately model galaxy clusters with ellipticity in the surface density with $\epsilon_\Sigma \lesssim 0.45$ (taking, roughly, the r/r_{sc}=3 values) which is well within the acceptable values for the cluster MS2137.

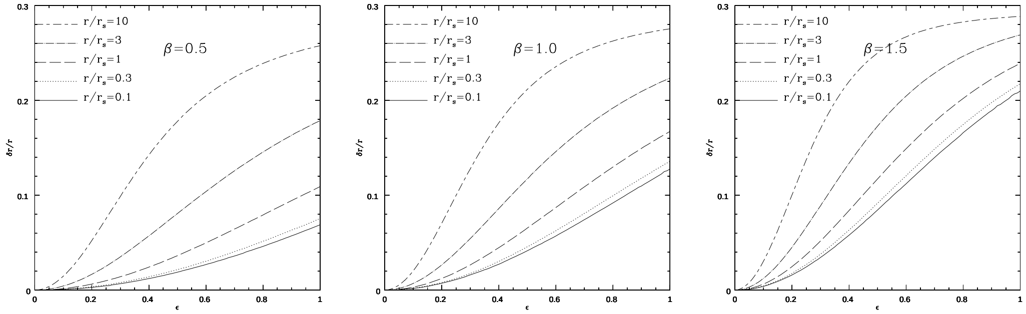

Figure 5.8: δr/r as a function of ϵ for a variety of pseudo-elliptical generalized NFW models with different inner slopes, β. This simply characterizes the deviation of the projected density from an ellipsoidal model for various r/r_{sc}. Write sentence about range in ϵ we think is acceptable.

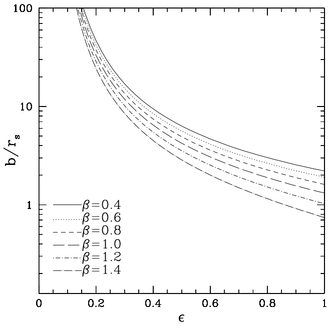

Figure 5.9: Distance from ellipse center along the minor axis at which Σ_ϵ becomes negative. Several example values for different inner dark matter density slopes, β, are plotted.

Chapter 6

Future Work

The quest to measure precisely the dark matter density profile in galaxy clusters has advanced rapidly during the course of my graduate school career. Prior to 2002, most observational approaches utilized X-ray observations of the intracluster medium, or the kinematics of cluster galaxies. Neither method separated the important baryonic contribution on small scales, as has been possible by simultaneously using the effects of gravitational lensing. The early only lensing work that specifically targeted the NFW profile was that of Tyson et al. (1998). However, in the realm of both X-ray observations and cluster galaxy kinematics great strides have recently been made. In particular, the deep spectroscopic study of the BCG in Abell 2199 (Kelson et al., 2002) has demonstrated that the velocity dispersion profile of the BCG rises in response to the dominant dark cluster halo and that an NFW halo cannot explain the results. Buote's group at the University of California Irvine has taken special care to select galaxy clusters that appear to have regular isophotes without cooling flows so that simple hydrostatic equilibrium analyses are more valid. These results strongly indicate that within the assumption of hydrostatic equilibrium the clusters they studied have steep inner cusps in accordance with CDM simulations, although with the caveat that they may not fully take into account the contribution of the BCG into their analysis (Lewis et al., 2003; Buote & Lewis, 2004).

But perhaps the most striking recent advance has been the analysis of the, deep, multi-color ACS imaging of Abell 1689 (Broadhurst et al., 2005a). These observations have yielded a significant increase in the number of strong lensing constraints with over 100 multiple images uncovered! Not only does this striking data allow for improved traditional analyses, but they also have encouraged bolder modeling. Diego et al. (2004) have succesfully implemented a parameter free model for the strong lensing data in A1689 recovering the surface density profile found by (Broadhurst et al., 2005a). Moreover, Oguri et al. (2005) have attempted to fit triaxial models to the data. These pioneering analyses clearly indicate a promising future role for strong lensing observations.

In addition, progress has been made by combining data sets. One example of this has been presented in this thesis: using strong lensing constraints simultaneously with those from the velocity dispersion profile of the BCG. As discussed throughout this thesis, using the velocity dispersion profile of the BCG allowed us to disentangle luminous from dark matter in the very core of the cluster. Beyond this sort of analysis, combining strong and weak gravitational lensing has been particularly powerful in securing mass constraints from ∼10 kpc to ∼ Mpc scales, which has led to interesting new constraints. Three analyses are particularly signficant: the clusters Cl0024 (Kneib et al., 2003), Abell 1689 (Broadhurst et al., 2005a) and MS2137 (Gavazzi et al., 2003). Common to all three clusters is a high inferred concentration parameter, c, the ratio of virial radius to NFW scale radius. Both Gavazzi (2005) and Oguri et al. (2005) have suggested that these results are due to the neglect of triaxiality in the modeling process, which can bias the mass and parameters determined for a system (see Fig 6.1). The combination of a strong+weak lensing analysis allows the mass to be probed from ∼100 kpc to ∼Mpc scales, partially eliminating certain degeneracies which are inherent to strong-lensing only analyses (e.g. the $\beta - r_{sc}$ degeneracy seen in Chapter 5) due to projection effects.

Prior to considering the role of future investigations it is pertinent to ask: What is the question we are trying to answer? Is the goal simply to test the predictions of CDM on galaxy cluster scales? Or should the goal be empirical: to measure and

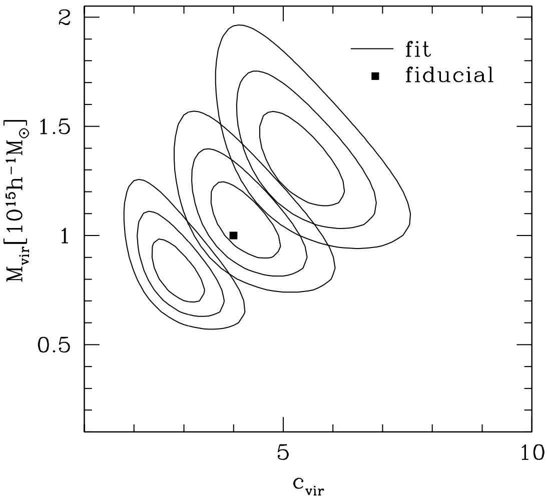

Figure 6.1: Constraints on the mass and halo concentration (the ratio of the virial radius to the NFW scale radius) when fitting a spherical NFW model to an inherently triaxial system. Constraint contours represent fits made on a triaxial halo while projecting along the principal axes. The square box shows the input values of the triaxial halo. This plot suggests that the triaxiality of real halos may need to be taken into account if the true parameters of the halo are to be inferred. This figure is reproduced from Oguri et al. (2005).

decompose the density profile in galaxy clusters, from 10 kpc to 1 Mpc in terms of its constituents. This thesis has demonstrated that the tools to do this are at our disposal and I will outline in this final section the general path I think can be taken to achieve them.

6.1 What Theorists Can Do

Here I suggest ways in which numerical workers could better facilitate comparisons between simulated dark matter halos (and more sophisticated simulations that include baryonic physics) and observations.

First, numerical simulators should make some effort to project their data into two dimensions for better comparison with observational results. Real galaxy clusters are three-dimensional objects with roughly triaxial structure, which is borne out in simulations (Jing & Suto, 2002). This naturally leads to characterizations of halos in three dimensional units, such as mass densities, scale radii or axial ratios. For instance, the original NFW density profile is just that, a spherically averaged three dimensional mass density profile. However, most observations can only infer surface mass density profiles and the projection from three dimensions to two during the modeling process can lead to ambiguous results and degeneracies (such as the afforementioned $\beta - r_{sc}$ degeneracy or mismeasurement of common parameters in triaxial halos, Figure 6.1). By projecting their results along multiple sight lines and illustrating what range of two-dimensional parameters that observers can expect to see, simulators could easily resolve these ambiguities. This of course is not to imply that three-dimensional results are not interesting and that observers should not be looking for signatures of triaxiality, just that simulators could address some of the apparent conflicts with CDM by making their results easily comparable to observations.

An understanding of which observations should be made and how to model them can progress by simulating observations of simulated cluster dark matter halos. This idea is beginning to be recognized in the community which measures the dark matter density profile in dwarf galaxies. For instance, Hayashi et al. (2004a) have taken triaxial, hydrodynamic simulations of disks embedded in CDM halos and performed mock long slit observations. They find that 25% of the time they measure rotation curves that would be interpreted as arising from a flat-cored dark matter halo even though the original profiles are NFW-like. Also, Rhee et al. (2004) have "observed" realistic simulations of dwarf galaxies and have found that slight morphological and dynamical perturbations caused by the presence of a small bulge or bar can cause typical long-slit observations to infer a flat-cored dark matter halo. Even though these studies have shown that current rotation curve observations which imply that dark matter halos have flat cores do not necessarily rule out cuspy models, they have not suggested any particular method for overcoming these obstacles to actually measuring the inner dark matter slope in dwarf galaxies.

One study at the galaxy cluster scale has sought to understand systematics involved in measuring cluster masses with weak gravitational lensing measurements by performing mock observations on simulated clusters (Clowe et al., 2004). The authors concluded that massive substructure and cluster asphericities do not prevent one from inferring reliable cluster masses and concentrations from simple, spherically averaged weak shear measurements, within the observational uncertainties. One could imagine other experiments involving mock observations of simulated clusters which seek to elucidate the best method for measuring the dark matter density profile in clusters. Simply by simulating clusters and ray-tracing through background sources to produce gravitational arcs and then performing standard strong lensing analyses on these "observations" important questions can be addressed, e.g. How many strong lensing arcs are needed before one can accurately estimate the cluster density profile? How complex does the lens model have to be to recover the actual underlying simulated cluster profile? Can we disentangle luminous from dark matter by combining different measurement techniques? Such work could point the way to what clusters should be observed and with what techniques in order to best determine their dark matter density profile. In fact, a paper in preparation is doing something very similar by taking simulations of galaxy clusters and "observing" gravitational arcs and mock velocity dispersion profiles of the BCGs (mimicking the observations presented in this thesis) and determining which modeling techniques accurately recover the inner dark matter density slope in these systems (Meneghetti et al. in preparation). Indeed it seems that much progress could be made if observers and theorists cooperated more.

6.2 What Observers Can Do

The ultimate goal of the observer should not just be measuring the inner density slope of cluster dark matter profiles. It should also be a complete characterization of the three massive components of clusters (dark matter, hot intracluster gas, and stellar matter) from kiloparsec scales out to the virial radius. The galaxy cluster scale is ideal for measuring the radial distribution of the prominent cluster mass components, since there are several observational techniques which both complement each other and can serve to disentangle luminous from dark matter in clusters: gravitational lensing, galaxy dynamics, and the X-ray emitting intracluster hot gas in hydrostatic equilibrium. Each of these observational probes permits a cross-disciplinary approach which combines and compares techniques.

Each observational technique has its strengths and weaknesses. Gravitational lensing is a direct probe of the mass without regard to its state or type. When weak and strong lensing are combined, the mass profile can be probed from ~ 10 kpc scales out to ~ 1 Mpc. However, this advantage has a weakness, because lensing alone cannot distinguish between luminous and dark matter. Without another mass probe, it is difficult to disentangle the two with lensing alone. X-ray analyses of the intracluster medium are also excellent at probing the cluster density profile from kpc to Mpc scales, especially with the Chandra and XMM satellites in orbit. However, these observations are always plagued by the necessary assumption of hydrostatic equilibrium and its inability to account for the massive BCG in the center of the cluster. Without having to assume hydrostatic equilibrium, it is possible to

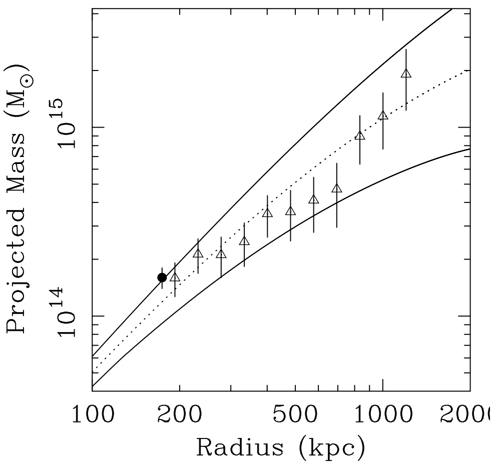

Figure 6.2: A comparison between the weak-lensing and X-ray mass estimates (assuming hydrostatic equilibrium) in Abell 2390. The results are in remarkable agreement given the apparently unrelaxed state of the cluster as seen in the X-ray and optical. Any discrepancy between the two measurements could indicate that the cluster is not truly in hydrostatic equilibrium and has other significant forms of pressure support.

probe the gas density profile (which makes up ∼20% of the total cluster mass) of a cluster. Used in combination with other techniques the gas density profile information from X-ray data can be used to disentangle that massive component from the rest of the mass model. Relative kinematics of constituent cluster galaxies can be used to probe the cluster potential by solving the spherical Jeans equation and thus measuring the total mass enclosed within concentric annuli. This dynamical approach can also account for and disentangle the mass associated with the cluster galaxies themselves, once again separating luminous from dark matter. The weakness inherent in using galaxy dynamics as a probe of the cluster potential is the need to make unwarranted assumptions about the orbital properties of the cluster galaxies, particularly noting the the degeneracy between the mass profile shape and orbital anisotropy in the results of any modeling.

An observational approach which combined and compared the above three techniques would be a powerful tool. Jointly analyzing lensing+X-ray+galaxy dynamics for a given cluster could, in principle, simultaneously account for each of the constituent mass components and probe the total density profile from ∼kpc to ∼Mpc scales. Of course, if any of the underlying assumptions inherent to each method are not actually correct then this would come out by comparing the methods. By comparing the mass profiles derived from the X-ray and lensing methodologies, it will be possible to probe directly deviations from hydrostatic equilibrium, and by extension, deviations from pure thermal pressure support of the cluster gas. A non-thermal pressure term could come from magnetic pressure, turbulence or bulk motions and is expected during cluster mergers or other low-level interactions (e.g. Markevitch et al. 2001). A direct comparison between X-ray and weak+strong lensing mass estimates has only been performed once, in Abell 2390 (Allen et al. 2001; Figure 6.2). A similar analysis performed on a sample of clusters would lend insight into the state of the hot intracluster gas and the density profile of clusters. Similarly, by comparing lensing and galaxy dynamics mass profiles one would be sensitive to departures from orbital isotropy in the galaxy orbits, breaking the traditional mass profile-orbital anisotropy degeneracy (see Figure 6.3). It is expected that at the center of the cluster the galaxy orbits are close to isotropic (e.g. Huss et al. 1999) but at larger radii, and among different galaxy populations (spirals vs. ellipticals) galaxy orbits should become anisotropic (e.g. Ghigna et al. 1998).

The combination of these three types of data sets on a well chosen sample of galaxy clusters would empirically establish the relationship between the major galaxy cluster mass components across three decades in radius and could elucidate the dynamical state of typical systems. The basis for such a data set is already in hand as a result of the search for gravitationally lensed arcs in the HST/WFPC2 archive presented in Chapter 4. In fact, out of that sample of clusters with strong gravitational lensing, I have identified ∼10 clusters with sufficient Chandra archival data for complementary study. While a difficult observational goal, such an analysis would serve as a template from which modern numerical simulations could be compared and perhaps hint at the nature of dark matter itself.

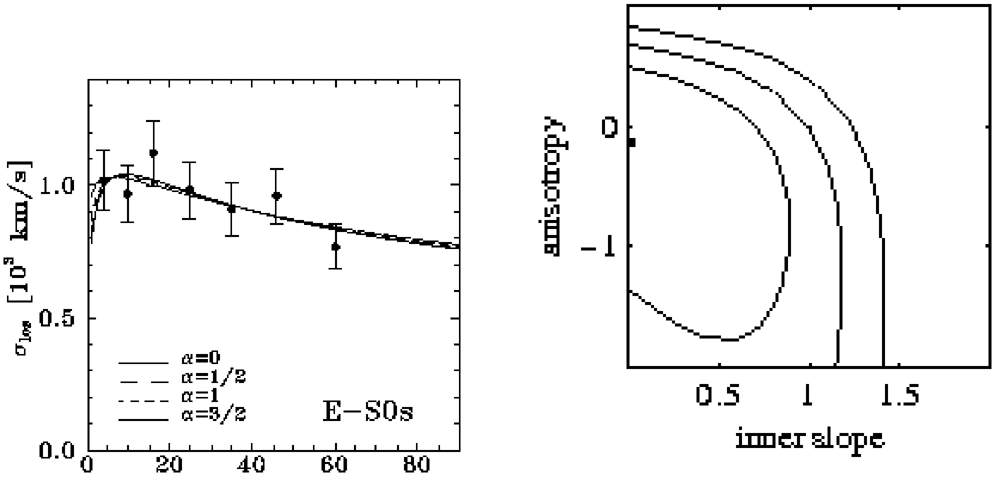

Figure 6.3: An illustration of the mass profile-orbital anisotropy degeneracy. **Left:** An example of the type of cluster galaxy velocity dispersion data obtainable, in this case for the Coma cluster. The various curves show fits to a generalization of the NFW profile with inner slope $\rho_{DM} \propto r^{-\beta}$. Note that virtually any slope can be fit to the velocity dispersion data on its own, due to the mass-orbital anisotropy degeneracy. **Right:** The actual constraints obtained on the inner DM slope and orbital anisotropy in the Coma cluster (Lokas & Mamon 2003). Although shallow DM slopes are preferred, no strong constraints can be obtained.

Bibliography

Allen, S. W., Ettori, S., & Fabian, A. C. 2001, MNRAS, 324, 877

Allen, S. W., Schmidt, R. W., & Fabian, A. C. 2002, MNRAS, 335, 256

Arabadjis, J. S., Bautz, M. W., & Arabadjis, G. 2004, ApJ, 617, 303

Arabadjis, J. S., Bautz, M. W., & Garmire, G. P. 2002, ApJ, 572, 66

Bahcall, N. A., Dong, F., Bode, P., Kim, R., Annis, J., McKay, T. A., Hansen, S., Schroeder, J., Gunn, J., Ostriker, J. P., Postman, M., Nichol, R. C., Miller, C., Goto, T., Brinkmann, J., Knapp, G. R., Lamb, D. O., Schneider, D. P., Vogeley, M. S., & York, D. G. 2003, ApJ, 585, 182

Barnes, E. I., Sellwood, J. A., & Kosowsky, A. 2004, AJ, 128, 2724

Bartelmann, M. 1996, A&A, 313, 697

Bartelmann, M., Huss, A., Colberg, J. M., Jenkins, A., & Pearce, F. R. 1998, A&A, 330, 1

Bartelmann, M., & Meneghetti, M. 2004, A&A, 418, 413

Bartelmann, M., & Weiss, A. 1994, A&A, 287, 1

Bertin, E., & Arnouts, S. 1996, A&AS, 117, 393

Binney, J. 1980, MNRAS, 190, 873

Binney, J., & Merrifield, M. 1998, Galactic astronomy (Galactic astronomy / James Binney and Michael Merrifield. Princeton, NJ : Princeton University Press, 1998. (Princeton series in astrophysics) QB857 .B522 1998 ($35.00))

Binney, J., & Tremaine, S. 1987, Galactic dynamics (Princeton, NJ, Princeton University Press, 1987, 747 p.)

Biviano, A., & Katgert, P. 2003, A&SS, 285, 25

Blandford, R. D., & Narayan, R. 1992, ARAA, 30, 311

Blumenthal, G. R., Faber, S. M., Flores, R., & Primack, J. R. 1986, ApJ, 301, 27

Blumenthal, G. R., Faber, S. M., Primack, J. R., & Rees, M. J. 1984, Nature, 311, 517

Borgani, S., Murante, G., Springel, V., Diaferio, A., Dolag, K., Moscardini, L., Tormen, G., Tornatore, L., & Tozzi, P. 2004, MNRAS, 348, 1078

Borriello, A., & Salucci, P. 2001, MNRAS, 323, 285

Borriello, A., Salucci, P., & Danese, L. 2003, MNRAS, 341, 1109

Bosma, A. 1978, Ph.D. Thesis

Broadhurst, T., Benítez, N., Coe, D., Sharon, K., Zekser, K., White, R., Ford, H., Bouwens, R., Blakeslee, J., Clampin, M., Cross, N., Franx, M., Frye, B., Hartig, G., Illingworth, G., Infante, L., Menanteau, F., Meurer, G., Postman, M., Ardila, D. R., Bartko, F., Brown, R. A., Burrows, C. J., Cheng, E. S., Feldman, P. D., Golimowski, D. A., Goto, T., Gronwall, C., Herranz, D., Holden, B., Homeier, N., Krist, J. E., Lesser, M. P., Martel, A. R., Miley, G. K., Rosati, P., Sirianni, M., Sparks, W. B., Steindling, S., Tran, H. D., Tsvetanov, Z. I., & Zheng, W. 2005a, ApJ, 621, 53

Broadhurst, T., Huang, X., Frye, B., & Ellis, R. 2000, ApJ, 534, L15

Broadhurst, T., Takada, M., Umetsu, K., Kong, X., Arimoto, N., Chiba, M., & Futamase, T. 2005b, ApJ, 619, L143

Bullock, J. S., Kolatt, T. S., Sigad, Y., Somerville, R. S., Kravtsov, A. V., Klypin, A. A., Primack, J. R., & Dekel, A. 2001, MNRAS, 321, 559

Buote, D. A. 2000, ApJ, 539, 172

Buote, D. A., & Lewis, A. D. 2004, ApJ, 604, 116

Cardelli, J. A., Clayton, G. C., & Mathis, J. S. 1989, ApJ, 345, 245

Carter, D., Bridges, T. J., & Hau, G. K. T. 1999, MNRAS, 307, 131

Ciotti, L. 1999, ApJ, 520, 574

Clowe, D., De Lucia, G., & King, L. 2004, MNRAS, 350, 1038

Crawford, C. S., Allen, S. W., Ebeling, H., Edge, A. C., & Fabian, A. C. 1999, MNRAS, 306, 857

Croft, R. A. C., Weinberg, D. H., Bolte, M., Burles, S., Hernquist, L., Katz, N., Kirkman, D., & Tytler, D. 2002, ApJ, 581, 20

Dahle, H., Hannestad, S., & Sommer-Larsen, J. 2003, ApJ, 588, L73

Dalal, N., Hennawi, J. F., & Bode, P. 2005, ApJ, 622, 99

Dalal, N., Holder, G., & Hennawi, J. F. 2004, ApJ, 609, 50

Dalal, N., & Keeton, C. R. 2003, ArXiv Astrophysics e-prints

Davis, M., Efstathiou, G., Frenk, C. S., & White, S. D. M. 1985, ApJ, 292, 371

de Blok, W. J. G. 2005, ArXiv Astrophysics e-prints

de Blok, W. J. G., & Bosma, A. 2002, A&A, 385, 816

de Blok, W. J. G., Bosma, A., & McGaugh, S. 2003, MNRAS, 340, 657

de Blok, W. J. G., & McGaugh, S. S. 1997, MNRAS, 290, 533

de Blok, W. J. G., McGaugh, S. S., Bosma, A., & Rubin, V. C. 2001, ApJ, 552, L23

Dekel, A., Arad, I., Devor, J., & Birnboim, Y. 2003, ApJ, 588, 680

Diego, J. M., Sandvik, H. B., Protopapas, P., Tegmark, M., Benitez, N., & Broadhurst, T. 2004, ArXiv Astrophysics e-prints

Diemand, J., Moore, B., & Stadel, J. 2004, MNRAS, 353, 624

Dressler, A. 1979, ApJ, 231, 659

Dubinski, J. 1998, ApJ, 502, 141

Dubinski, J., & Carlberg, R. G. 1991, ApJ, 378, 496

Dutton, A. A., Courteau, S., de Jong, R., & Carignan, C. 2005, ApJ, 619, 218

Ebeling, H., Edge, A. C., Bohringer, H., Allen, S. W., Crawford, C. S., Fabian, A. C., Voges, W., & Huchra, J. P. 1998, MNRAS, 301, 881

Ebeling, H., Voges, W., Bohringer, H., Edge, A. C., Huchra, J. P., & Briel, U. G. 1996, MNRAS, 281, 799

Edge, A. C., Smith, G. P., Sand, D. J., Treu, T., Ebeling, H., Allen, S. W., & van Dokkum, P. G. 2003, ApJ, 599, L69

El-Zant, A., Shlosman, I., & Hoffman, Y. 2001, ApJ, 560, 636

El-Zant, A. A., Hoffman, Y., Primack, J., Combes, F., & Shlosman, I. 2004, ApJ, 607, L75

Ellis, R., Allington-Smith, J., & Smail, I. 1991, MNRAS, 249, 184

Ellis, R., Santos, M. R., Kneib, J., & Kuijken, K. 2001, ApJ, 560, L119

Ettori, S., & Fabian, A. C. 1999, MNRAS, 305, 834

Ettori, S., Fabian, A. C., Allen, S. W., & Johnstone, R. M. 2002, MNRAS, 331, 635

Faber, S. M., & Gallagher, J. S. 1979, ARAA, 17, 135

Fabricant, D., Lecar, M., & Gorenstein, P. 1980, ApJ, 241, 552

Ferguson, H. C., Dickinson, M., Giavalisco, M., Kretchmer, C., Ravindranath, S., Idzi, R., Taylor, E., Conselice, C. J., Fall, S. M., Gardner, J. P., Livio, M., Madau, P., Moustakas, L. A., Papovich, C. M., Somerville, R. S., Spinrad, H., & Stern, D. 2004, ApJ, 600, L107

Fisher, D., Illingworth, G., & Franx, M. 1995, ApJ, 438, 539

Flores, R. A., Maller, A. H., & Primack, J. R. 2000, ApJ, 535, 555

Flores, R. A., & Primack, J. R. 1994, ApJ, 427, L1

Fort, B., Le Fevre, O., Hammer, F., & Cailloux, M. 1992, ApJ, 399, L125

Franx, M. 1993, PASP, 105, 1058

Franx, M., Illingworth, G. D., Kelson, D. D., van Dokkum, P. G., & Tran, K. 1997, ApJ, 486, L75+

Freeman, K. C. 1970, ApJ, 160, 811

Frenk, C. S., White, S. D. M., Davis, M., & Efstathiou, G. 1988, ApJ, 327, 507

Fruchter, A. S., & Hook, R. N. 2002, PASP, 114, 144

Fukushige, T., Kawai, A., & Makino, J. 2004, ApJ, 606, 625

Fukushige, T., & Makino, J. 1997, ApJ, 477, L9+

—. 2003, ApJ, 588, 674

Gaitskell, R. J. 2004, Annual Review of Nuclear and Particle Science, 54, 315

Gavazzi, R. 2005, ArXiv Astrophysics e-prints

Gavazzi, R., Fort, B., Mellier, Y., Pelló, R., & Dantel-Fort, M. 2003, A&A, 403, 11

Gebhardt, K., Richstone, D., Tremaine, S., Lauer, T. R., Bender, R., Bower, G., Dressler, A., Faber, S. M., Filippenko, A. V., Green, R., Grillmair, C., Ho, L. C., Kormendy, J., Magorrian, J., & Pinkney, J. 2003, ApJ, 583, 92

Gehrels, N. 1986, ApJ, 303, 336

Gerhard, O., Kronawitter, A., Saglia, R. P., & Bender, R. 2001, AJ, 121, 1936

Ghigna, S., Moore, B., Governato, F., Lake, G., Quinn, T., & Stadel, J. 1998, MNRAS, 300, 146

—. 2000, ApJ, 544, 616

Gioia, I. M., Shaya, E. J., Le Fevre, O., Falco, E. E., Luppino, G. A., & Hammer, F. 1998, ApJ, 497, 573

Gladders, M. D., Hoekstra, H., Yee, H. K. C., Hall, P. B., & Barrientos, L. F. 2003, ApJ, 593, 48

Gnedin, O. Y., Kravtsov, A. V., Klypin, A. A., & Nagai, D. 2004, ApJ, 616, 16

Golse, G., & Kneib, J.-P. 2002, A&A, 390, 821

Gonzalez, A. H., Zabludoff, A. I., & Zaritsky, D. 2005, ApJ, 618, 195

Hammer, F., Gioia, I. M., Shaya, E. J., Teyssandier, P., Le Fevre, O., & Luppino, G. A. 1997, ApJ, 491, 477

Hayashi, E., Navarro, J. F., Jenkins, A., Frenk, C. S., Power, C., White, S. D. M., Springel, V., Stadel, J., Quinn, T., & Wadsley, J. 2004a, ArXiv Astrophysics e-prints

Hayashi, E., Navarro, J. F., Power, C., Jenkins, A., Frenk, C. S., White, S. D. M., Springel, V., Stadel, J., & Quinn, T. R. 2004b, MNRAS, 355, 794

Hernquist, L. 1990, ApJ, 356, 359

Hogan, C. J., & Dalcanton, J. J. 2000, Phys. Rev. D, 62, 063511

Huss, A., Jain, B., & Steinmetz, M. 1999, MNRAS, 308, 1011

Jaffe, W. 1983, MNRAS, 202, 995

Jimenez, R., Verde, L., & Oh, S. P. 2003, MNRAS, 339, 243

Jing, Y. P. 2001, ApJ, 550, L125

Jing, Y. P., & Suto, Y. 2000, ApJ, 529, L69

—. 2002, ApJ, 574, 538

Jones, C., Mandel, E., Schwarz, J., Forman, W., Murray, S. S., & Harnden, F. R. 1979, ApJ, 234, L21

Jorgensen, I., Franx, M., & Kjaergaard, P. 1995, MNRAS, 276, 1341

Keeton, C. R. 2001, ApJ, 562, 160

Keeton, C. R., & Madau, P. 2001, ApJ, 549, L25

Kelson, D. D., Illingworth, G. D., van Dokkum, P. G., & Franx, M. 2000, ApJ, 531, 159

Kelson, D. D., Zabludoff, A. I., Williams, K. A., Trager, S. C., Mulchaey, J. S., & Bolte, M. 2002, ApJ, 576, 720

Kent, S. M., & Gunn, J. E. 1982, AJ, 87, 945

Klypin, A., Kravtsov, A. V., Bullock, J. S., & Primack, J. R. 2001, ApJ, 554, 903

Kneib, J., Ellis, R. S., Santos, M. R., & Richard, J. 2004, ApJ, 607, 697

Kneib, J., Hudelot, P., Ellis, R. S., Treu, T., Smith, G. P., Marshall, P., Czoske, O., Smail, I., & Natarajan, P. 2003, ApJ, 598, 804

Kneib, J.-P. 1993, Ph.D. Thesis

Kneib, J.-P., Ellis, R. S., Smail, I., Couch, W. J., & Sharples, R. M. 1996, ApJ, 471, 643

Koopmans, L. V. E., & Treu, T. 2002, ApJ, 568, L5

—. 2003, ApJ, 583, 606

Kravtsov, A. V., Nagai, D., & Vikhlinin, A. A. 2005, ApJ, 625, 588

Kronawitter, A., Saglia, R. P., Gerhard, O., & Bender, R. 2000, A&AS, 144, 53

Laine, S., van der Marel, R. P., Lauer, T. R., Postman, M., O'Dea, C. P., & Owen, F. N. 2003, AJ, 125, 478

Landolt, A. U. 1992, AJ, 104, 340

Le Fevre, O., Hammer, F., Angonin, M. C., Gioia, I. M., & Luppino, G. A. 1994, ApJ, 422, L5

Lewis, A. D., Buote, D. A., & Stocke, J. T. 2003, ApJ, 586, 135

Lewis, A. D., Stocke, J. T., & Buote, D. A. 2002, ApJ, 573, L13

Loeb, A., & Peebles, P. J. E. 2003, ApJ, 589, 29

Łokas, E. L., & Mamon, G. A. 2003, MNRAS, 343, 401

Luppino, G. A., Gioia, I. M., Hammer, F., Le Fèvre, O., & Annis, J. A. 1999, A&AS, 136, 117

Mahdavi, A., & Geller, M. J. 2004, ApJ, 607, 202

Mao, S., Mo, H. J., & White, S. D. M. 1998, MNRAS, 297, L71

Markevitch, M., Gonzalez, A. H., Clowe, D., Vikhlinin, A., Forman, W., Jones, C., Murray, S., & Tucker, W. 2004, ApJ, 606, 819

Markevitch, M., Vikhlinin, A., & Mazzotta, P. 2001, ApJ, 562, L153

Mellier, Y., Fort, B., & Kneib, J.-P. 1993, ApJ, 407, 33

Meneghetti, M., Bartelmann, M., & Moscardini, L. 2003a, MNRAS, 346, 67

—. 2003b, MNRAS, 340, 105

Meneghetti, M., Jain, B., Bartelmann, M., & Dolag, K. 2004, ArXiv Astrophysics e-prints

Meneghetti, M., Yoshida, N., Bartelmann, M., Moscardini, L., Springel, V., Tormen, G., & White, S. D. M. 2001, MNRAS, 325, 435

Merritt, D. 1985a, MNRAS, 214, 25P

—. 1985b, AJ, 90, 1027

—. 1987, ApJ, 313, 121

Merritt, D., & Aguilar, L. A. 1985, MNRAS, 217, 787

Miralda-Escudé, J. 2002, ApJ, 564, 60

Miralda-Escude, J. 1991, ApJ, 370, 1

—. 1993, ApJ, 403, 497

—. 1995, ApJ, 438, 514

Molikawa, K., & Hattori, M. 2001, ApJ, 559, 544

Moore, B. 1994, Nature, 370, 629

Moore, B., Ghigna, S., Governato, F., Lake, G., Quinn, T., Stadel, J., & Tozzi, P. 1999a, ApJ, 524, L19

Moore, B., Governato, F., Quinn, T., Stadel, J., & Lake, G. 1998, ApJ, 499, L5+

Moore, B., Quinn, T., Governato, F., Stadel, J., & Lake, G. 1999b, MNRAS, 310, 1147

Nagai, D., & Kravtsov, A. V. 2005, ApJ, 618, 557

Narayan, R., & Bartelmann, M. 1996, Lectures on Gravitational Lensing

Natarajan, P., & Kneib, J.-P. 1996, MNRAS, 283, 1031

Navarro, J. F., Frenk, C. S., & White, S. D. M. 1996, ApJ, 462, 563

—. 1997, ApJ, 490, 493

Navarro, J. F., Hayashi, E., Power, C., Jenkins, A. R., Frenk, C. S., White, S. D. M., Springel, V., Stadel, J., & Quinn, T. R. 2004, MNRAS, 349, 1039

Nipoti, C., Stiavelli, M., Ciotti, L., Treu, T., & Rosati, P. 2003, MNRAS, 344, 748

Nusser, A., & Sheth, R. K. 1999, MNRAS, 303, 685

Oguri, M., Takada, M., Umetsu, K., & Broadhurst, T. 2005, ArXiv Astrophysics e-prints

Oguri, M., Taruya, A., & Suto, Y. 2001, ApJ, 559, 572

Oke, J. B., Cohen, J. G., Carr, M., Cromer, J., Dingizian, A., Harris, F. H., Labrecque, S., Lucinio, R., Schaal, W., Epps, H., & Miller, J. 1995, PASP, 107, 375

Peebles, P. J. E. 1982, ApJ, 263, L1

—. 2000, Phys. Rev. D, 62, 023502

Percival, W. J., Baugh, C. M., Bland-Hawthorn, J., Bridges, T., Cannon, R., Cole, S., Colless, M., Collins, C., Couch, W., Dalton, G., De Propris, R., Driver, S. P., Efstathiou, G., Ellis, R. S., Frenk, C. S., Glazebrook, K., Jackson, C., Lahav, O., Lewis, I., Lumsden, S., Maddox, S., Moody, S., Norberg, P., Peacock, J. A., Peterson, B. A., Sutherland, W., & Taylor, K. 2001, MNRAS, 327, 1297

Pettini, M., Steidel, C. C., Adelberger, K. L., Dickinson, M., & Giavalisco, M. 2000, ApJ, 528, 96

Power, C., Navarro, J. F., Jenkins, A., Frenk, C. S., White, S. D. M., Springel, V., Stadel, J., & Quinn, T. 2003, MNRAS, 338, 14

Pratt, G. W., & Arnaud, M. 2002, A&A, 394, 375

Press, W. H., Flannery, B. P., Teukolsky, S. A., & Vetterling, W. T. 1988, Numerical recipes in C: the art of scientific computing (New York, NY, USA: Cambridge University Press)

Reed, D., Gardner, J., Quinn, T., Stadel, J., Fardal, M., Lake, G., & Governato, F. 2003, MNRAS, 346, 565

Rhee, G., Valenzuela, O., Klypin, A., Holtzman, J., & Moorthy, B. 2004, ApJ, 617, 1059

Ricotti, M. 2003, MNRAS, 344, 1237

Rix, H.-W., de Zeeuw, P. T., Cretton, N., van der Marel, R. P., & Carollo, C. M. 1997, ApJ, 488, 702

Roberts, M. S. 1975, in Dynamics of stellar systems; Proceedings of the Symposium, Besancon, France, September 9-13, 1974. (A76-12676 02-90) Dordrecht, D. Reidel Publishing Co., 1975, p. 331-339; Discussion, p. 339, 340., 331–339

Rogstad, D. H., & Shostak, G. S. 1972, ApJ, 176, 315

Rubin, V. C., Burstein, D., Ford, W. K., & Thonnard, N. 1985, ApJ, 289, 81

Rubin, V. C., & Ford, W. K. J. 1970, ApJ, 159, 379

Rubin, V. C., Thonnard, N., & Ford, W. K. 1980, ApJ, 238, 471

Salucci, P., & Burkert, A. 2000, ApJ, 537, L9

Sand, D. J., Treu, T., & Ellis, R. S. 2002, ApJ, 574, L129

Sand, D. J., Treu, T., Ellis, R. S., & Smith, G. P. 2005, ApJ, 627, 32

Sand, D. J., Treu, T., Smith, G. P., & Ellis, R. S. 2004, ApJ, 604, 88

Santos, M. R., Ellis, R. S., Kneib, J.-P., Richard, J., & Kuijken, K. 2004, ApJ, 606, 683

Schlegel, D. J., Finkbeiner, D. P., & Davis, M. 1998, ApJ, 500, 525

Schmidt, R. W., Allen, S. W., & Fabian, A. C. 2001, MNRAS, 327, 1057

Schneider, P., Ehlers, J., & Falco, E. E. 1992, Gravitational Lenses (Gravitational Lenses, XIV, 560 pp. 112 figs.. Springer-Verlag Berlin Heidelberg New York. Also Astronomy and Astrophysics Library)

Seitz, S., Saglia, R. P., Bender, R., Hopp, U., Belloni, P., & Ziegler, B. 1998, MNRAS, 298, 945

Sellwood, J. A., & McGaugh, S. S. 2005, ArXiv Astrophysics e-prints

Sheinis, A. I., Bolte, M., Epps, H. W., Kibrick, R. I., Miller, J. S., Radovan, M. V., Bigelow, B. C., & Sutin, B. M. 2002, PASP, 114, 851

Simon, J. D., Bolatto, A. D., Leroy, A., & Blitz, L. 2003, ApJ, 596, 957

Simon, J. D., Bolatto, A. D., Leroy, A., Blitz, L., & Gates, E. L. 2005, ApJ, 621, 757

Smail, I., Dressler, A., Kneib, J.-P., Ellis, R. S., Couch, W. J., Sharples, R. M., & Oemler, A. J. 1996, ApJ, 469, 508

Smith, G. P., Kneib, J., Ebeling, H., Czoske, O., & Smail, I. 2001, ApJ, 552, 493

Smith, G. P., Kneib, J.-P., Smail, I., Mazzotta, P., Ebeling, H., & Czoske, O. 2005, MNRAS, 359, 417

Smith, G. P., Smail, I., Kneib, J.-P., Davis, C. J., Takamiya, M., Ebeling, H., & Czoske, O. 2002, MNRAS, 333, L16

Smith, S. 1936, ApJ, 83, 23

Spergel, D. N., & Steinhardt, P. J. 2000, Physical Review Letters, 84, 3760

Spergel, D. N., Verde, L., Peiris, H. V., Komatsu, E., Nolta, M. R., Bennett, C. L., Halpern, M., Hinshaw, G., Jarosik, N., Kogut, A., Limon, M., Meyer, S. S., Page, L., Tucker, G. S., Weiland, J. L., Wollack, E., & Wright, E. L. 2003, ApJS, 148, 175

Stiavelli, M., & Sparke, L. S. 1991, ApJ, 382, 466

Swaters, R. A., Madore, B. F., van den Bosch, F. C., & Balcells, M. 2003, ApJ, 583, 732

Swinbank, A. M., Smith, J., Bower, R. G., Bunker, A., Smail, I., Ellis, R. S., Smith, G. P., Kneib, J.-P., Sullivan, M., & Allington-Smith, J. 2003, ApJ, 598, 162

Tasitsiomi, A., Kravtsov, A. V., Gottlöber, S., & Klypin, A. A. 2004, ApJ, 607, 125

Torri, E., Meneghetti, M., Bartelmann, M., Moscardini, L., Rasia, E., & Tormen, G. 2004, MNRAS, 349, 476

Treu, T., & Koopmans, L. V. E. 2002, ApJ, 575, 87

—. 2003, MNRAS, 343, L29

—. 2004, ApJ, 611, 739

Treu, T., Stiavelli, M., Bertin, G., Casertano, S., & Møller, P. 2001, MNRAS, 326, 237

Treu, T., Stiavelli, M., Casertano, S., Møller, P., & Bertin, G. 1999, MNRAS, 308, 1037

Tyson, J. A., Kochanski, G. P., & dell'Antonio, I. P. 1998, ApJ, 498, L107+

van Albada, T. S. 1982, MNRAS, 201, 939

van Albada, T. S., Bahcall, J. N., Begeman, K., & Sancisi, R. 1985, ApJ, 295, 305

van den Bosch, F. C., & Swaters, R. A. 2001, MNRAS, 325, 1017

van der Marel, R. P. 1994, MNRAS, 270, 271

van der Marel, R. P., & Franx, M. 1993, ApJ, 407, 525

van der Marel, R. P., Magorrian, J., Carlberg, R. G., Yee, H. K. C., & Ellingson, E. 2000, AJ, 119, 2038 van Dokkum, P. G. 2001, PASP, 113, 1420

van Dokkum, P. G., & Ellis, R. S. 2003, ApJ, 592, L53

van Dokkum, P. G., & Franx, M. 1996, MNRAS, 281, 985

Wambsganss, J., Bode, P., & Ostriker, J. P. 2004, ApJ, 606, L93

Warren, M. S., Quinn, P. J., Salmon, J. K., & Zurek, W. H. 1992, ApJ, 399, 405

Williams, L. L. R., Navarro, J. F., & Bartelmann, M. 1999, ApJ, 527, 535

Wyithe, J. S. B., Turner, E. L., & Spergel, D. N. 2001, ApJ, 555, 504

Zaritsky, D., & Gonzalez, A. H. 2003, ApJ, 584, 691

Zwicky, F. 1937, ApJ, 86, 217